An atomically flat gold film thermometer on mica for calorimetric applications

Tesi di laurea magistrale

Candidato: Thea Papa

Università di Pisa

Luglio 2018

Indice

Introduction

This thesis reports the research work on the development of a sensitive atomically flat gold film thermometer which exploits *mica* as a substrate. Besides being an insulator, this mineral boasts a low thermal conductivity that allows an improved thermal decoupling of the sensor from its substrate, if compared to the largely utilized silicon (Si thermal conductivity is about 300 times higher). It is also mechanically soft and elastic, useful for applications in flexible electronics. Moreover, a mica substrate allows the gold re-crystallization, thus permitting the investigation of the processes which can affect the structure of the sensor itself, or of a sample, with atomic resolution, by the use of the Scanning Tunneling Microscope (STM).
This entire investigation has been realized at the facilities of Laboratorio NEST of Scuola Normale Superiore. The sample preparation has been performed in clean and controlled conditions (clean room), and the measurements have been taken in an Ultra-High Vacuum environment (UHV chamber of a RHK Technology Scanning Tunneling Microscope).
This study is inserted in the framework of calorimetric techniques, which are useful means to investigate the properties of matter by measuring the heat exchange during a system evolution. Indeed, an energy flux accompanies any evolution of a system, giving invaluable information on the processes underlying the evolution itself. A large number of commercial calorimeters can be found, specialized in studying solid or liquid samples, phase transitions and chemical reactions generally.

However, typical commercial calorimeters require a sample mass in the mg range and have a quite limited sensitivity in energy ($\sim$ mJ). Very sensitive thermometric techniques have been successfully developed to measure milli-Kelvin temperature differences in nano-scale devices, mainly in thermoelectric ones. Such thermometers, however, can operate only at low temperatures (below a few Kelvin) or at least their sensitivity drops to tenths of Kelvin at room temperature.
In this context we present the improvement of a recently reported thermometric technique, which has been utilized to monitor the hydrogen storage in titanium-functionalized mono-layer graphene [1]. The actual focus of our upgrade is the substrate of the sensor: *mica* has been chosen to replace silicon in order to gain in terms of sensitivity but mostly to exploit its atomically flat surface. Indeed it allows the gold re-crystallization, thus permitting to take advantage of the STM potentiality to investigate the surface of the sample after an experiment of hydrogen adsorption, for example, or any other process which could affect the structure of the sensor/sample. For testing the new sensor, an experiment of atomic hydrogen adsorption on the gold film itself has been performed. The old sensor has been subjected to the same experiment, as well, in order to compare the performances of the two. This testing has highlighted the potentiality of our sensor: indeed it allowed to study a change in the gold surface reconstruction that only an atomically flat surface could reveal.
A summary description of the thesis chapters is briefly listed below:

- In Chapter 1 we present the state of the art of the current research. The motivation of this research and its starting point (first prototype of the gold film thermometer), with focus on mica as new substrate for the sensor, are discussed.

- In Chapter 2 we describe the experimental setup and the measuring principles utilized for the measurements.

- In Chapter 3 we present the sample fabrication and calibration, with the related issues. These procedures are fundamental in order to get the best possible gold reconstructed surface to exploit in the STM analysis of the sensor surface, but also to extract the calibration parameters necessary to derive a quantitative analysis from our experiments.

- In Chapter 4 we discuss the testing of the thermometer and we compare its performance with that of the first prototype of the sensor.
- In Chapter 5 the final conclusions are drawn and an outlook of future improvements is discussed.

State Of The Art 1

The measurement of energy/heat exchange between a system and its environment is an important issue in many chemical and physical problems. Therefore, calorimetry has been widely utilized to investigate the properties of matter, especially in the presence of processes affecting the sample structure or inducing changes in the sample's thermodynamic conditions (chemical reactions, phase transitions, etc.). In the following a brief survey of calorimetry and an original improvement to study very small samples will be presented.

1.1 Calorimetry

Calorimetry is the science of measuring changes in state variables of a body, for the purpose of deriving the heat transfer associated with changes of its state, due to chemical reactions, physical changes, or phase transitions under specified constraints. The word calorimetry is derived from the Latin word *calor*, meaning heat and the Greek word *μέτρον* (metron), meaning measure. The Scottish physician and scientist Joseph Black is said to be the founder of the science of calorimetry, and he was the first to recognize the distinction between heat and temperature [2]. Indeed, *temperature* is the measure of the average kinetic energy of the molecules in a substance, while *heat* is the total energy that these moving molecules have.
Any calorimeter (an object which allows to measure the heat transfer) is basically made of a thermal bath and a measuring chamber which accommodates the

sample. While the sample's temperature varies during the process under investigation, the thermal bath acts as a heat sink (or source) with a fixed temperature, and allows to measure $\Delta T = T_{sample} - T_{bath}$ as a function of time.
The arrangement of calorimeters in a classification system should be based on a simple and sensible order structure, suitable for practical application. Several classification criteria have been suggested but with modest results. A particular difficulty in the classification of calorimeters arises from the fact that many calorimeters can be operated in various modes, so that a certain instrument must often be classified in different ways, depending on the mode of operation. Often, the same applies to the measuring principle, which can be changed in certain calorimeters. Three primary groups of criteria are taken as a basis of classification: the principles of measurement, the mode of operation, and the construction principle. On the basis of the measuring principle, calorimeters can be classified in three groups (see Ref. [3]):

- heat compensating calorimeters
- heat accumulating calorimeters
- heat exchanging calorimeters

In *heat compensating calorimeters*, the effect of the heat to be measured is compensated, either passively by the phase transition of a suitable calorimeter substance (e.g. ice), or with the aid of an active control system, which compensates the temperature change in the sample (or the sample container) through electrical heating/cooling or other suitable heat sources/sinks. The compensation energy is determined from the mass of the transformed calorimeter substance or from the electrical heating/cooling energy.
Advantages of the compensation method are that the measurement is carried out under quasi-isothermal conditions and thus heat leaks remain unchanged to a first approximation. Examples of heat compensating calorimeters are: ice calorimeters, adiabatic scanning calorimeters and power compensating Differential Scanning Calorimeters (DSC) (see Ref. [3] for details).
In *heat accumulating calorimeters*, the effect (for example an increase in temperature) of the heat to be measured is not minimized by any compensation, but leads to a temperature change in the sample and the calorimeter substance with which

the sample is thermally connected. This temperature change is the quantity to be measured and is proportional to the amount of heat exchanged between the sample and the calorimeter substance. Examples of heat accumulating calorimeters are drop calorimeters, adiabatic bomb calorimeters and flow calorimeters (see Ref. [3] for details).
In *heat exchanging calorimeters*, a defined exchange of heat takes place between the sample (sample container/crucible/support) and the surroundings. The amount of flowing heat is determined on the basis of the temperature difference along a "thermal resistance" between sample and surroundings. By recording the dependence of the heat flow rate on time, it is possible to carry out kinetic investigations. An example of heat-exchanging calorimeter is the heatflux DSC (see Ref. [3] for details).

For what concerns the construction principles, heat accumulation and heat compensation calorimeters are usually built up with single vessels, whereas the twin arrangement, first introduced by Joule in 1845, is often used with heat-exchanging calorimeters. In the latter case, the vessels are arranged as perfect twins with the detection units being in opposition to give a differential signal. Thus, extraneous disturbances are canceled, giving long-term stability and high precision for determination of slow processes. It is also possible to allow a reaction to proceed in one vessel, while running a control (or blank) measurement in the second vessel [3].

In the last decades, the research community has developed a growing number of devices at the micro- or nano-scale. Increasingly, sensors, catalyzers, and energy storage systems are designed as nano-devices which represent the building blocks for commercial "macroscopic" objects. However commercial calorimeters involve the use of macroscopic amount of material (of the order of milligrams or millimoles of substances) and have a limited sensivity in energy ($\sim$mJ). Recently, very sensitive thermometric techniques have been successfully developed to measure milli-Kelvin temperature differences in nano-scale devices, mainly in thermoelectric ones [4]. Such thermometers, however, can operate only at low temperatures (below a few Kelvin) or at least their sensitivity drops to tenths of Kelvin at room temperature.

In this context, an original thermometric technique has been presented in Ref. [1], and has been utilized to monitor the hydrogen storage in titanium-functionalized mono-layer graphene. The enthalpy variation ΔH due to an adsorption process (in this case hydrogen adsorption) consists in the change in internal energy of the system (ΔU) plus the work needed to change the system's volume (L):

$$\Delta H = \Delta U + L = C_p \cdot \Delta T + V \cdot \Delta P \tag{1.1}$$

where C_p is the heat capacity at constant pressure, ΔT is the temperature change consequent to the heat exchange and ΔP is the pressure variation. For processes under constant pressure, ΔH is equivalent to the total heat exchanged by the system in the exothermic (or endothermic) reaction:

$$\Delta H = \delta Q \tag{1.2}$$

where δQ can be written as [5]:

$$\delta Q = C_p \cdot \Delta T \tag{1.3}$$

The system heat capacity at constant pressure C_p can be written as $C_p = c \cdot m$, where c is the specific heat capacity and m is the mass of the system/sample. Assuming time-independent sample mass and specific heat capacity, in case of exothermic heat release H_r, equation (1.3) can be written in the following differential form:

$$\frac{\delta H_r}{\delta t} = C_p \cdot \frac{\delta \Delta T}{\delta t} \tag{1.4}$$

Therefore, knowing the heat capacity of the system it is possible to extract the heat release from the recording of the temperature variation. In the (real) case of thermal losses, by introducing the heat transfer coefficient λ, it is possible to describe the losses through the sample of interest and its substrate:

$$\frac{\delta H_r}{\delta t} = C_p \cdot \frac{\delta \Delta T}{\delta t} + \lambda \cdot \Delta T \tag{1.5}$$

In order to analyse the calorimetric data that will be recorded, our system can be described as in [1], by a simple thermal model in which the thermometer is heated

by the adsorption of a thermal power $P(t)$ (so its temperature increases) while at the same time it releases energy by heat losses towards the substrate. The losses are described by the heat transfer coefficient λ and it is possible to assume that the mica substrate acts as a thermal bath at fixed temperature T_0, because of its very high heat capacity with respect to that of the sensor. Moreover, assuming that the heat capacity of the sensor remains constant during the time interval of the measurement we can write (from equation (1.5)):

$$C_{sensor} \cdot \frac{dT_{sensor}(t)}{dt} = P(t) - \lambda \cdot \Delta T(t) \tag{1.6}$$

with $\Delta T(t) = T_{sensor}(t) - T_0$ [6, 7], where $T_0 = T(t = 0)$. C_{sensor} is the heat capacity at constant pressure but from now on we will omit the subscript p.
If we supply a constant power P and consider $dT_{sensor}(t) = d(T_{sensor}(t) - T_0) = d\Delta T(t)$ equation (1.6) can be rewritten as:

$$C_{sensor} \cdot \frac{d\Delta T(t)}{dt} = P - \lambda \cdot \Delta T(t) \tag{1.7}$$

By imposing the initial condition $\Delta T(t = 0) = 0$, this first-order constant-coefficient linear differential equation in $\Delta T(t)$ can be solved, giving the solution:

$$\Delta T(t) = T(t) - T_0 = \frac{P}{\lambda} \cdot \left[1 - exp\left(-\frac{t}{\tau}\right)\right] \tag{1.8}$$

where $\tau = C_{sensor}/\lambda$. In order to extract the unknown heat release which will heat the sensor during the exothermic adsorption of hydrogen, equation (1.6) can be adapted as:

$$\frac{\delta H_r}{\delta t} = C_{sensor} \cdot \frac{\delta \Delta T(t)}{\delta t} + \lambda \cdot \Delta T(t) \tag{1.9}$$

where H_r is the total heat released [8].
In Ref. [1] the exothermic reaction that binds hydrogen to graphene has been detected and analysed, in order to extract the total heat released H_r, as explained in the following section.

1.2 Nano-scale calorimetry

An original development of the calorimetric technique, which extends the application of calorimetry to microscopic devices, is reported in [1]. The presented experimental setup allows to detect the enthalpy released during the adsorption process of $\sim 10^{-10}$ mol of D_2 on titanium-functionalized monolayer graphene (Ti-MLG), by using a sensor having physical dimensions of $\sim$5×5 mm^2. This thermometer can, in principle, operate in the temperature range from 50 to 900 K. Operating in the temperature range 300-600 K, a Noise Equivalent Temperature Difference of 10 mK has been achieved. The calorimetric technique described in [1] has the advantage of scalability of sample dimensions and permits the direct measurement of the adsorption energy, without relying on a destructive measurement such as the Thermal Desorption Spectroscopy (TDS) (described in the following chapter). The work of Ref. [1] is briefly summarized in the following.
The sensor in question is a gold film thermometer which acts as temperature probe and holder for the Ti-MLG. The electrical resistance of the Au film increases with temperature, following the linear relation [9]: $R(T) = R_0[1 + \alpha(T - T_0)]$, where R_0 is the resistance at the reference temperature T_0 (room temperature) and α is the resistance temperature coefficient. The temperature increase of the sensor causes a resistance increase of the gold layer, that can be measured with a Wheatstone Bridge cascaded to a high quality PreAmplifier.
The thermometer has been subjected to a careful calibration through several heating cycles, in order to obtain the coefficient α of the sensor, from the recorded Resistance vs. Temperature curves (via linear fit), and the electrical resistivity.
After this initial characterization, MLG has been transferred on the gold film and the sensor has been calibrated again. Finally, graphene has been functionalized with titanium via evaporation in situ, inside the UHV chamber which hosted all the performed measurements. 6.5 ML of titanium have been deposited, in order to ensure a 100% coverage of the graphene layer (because Ti tends to cluster). After the deposition, the thermometer calibration has been repeated, thus producing the final calibration parameters.
About 20 minutes after the Ti deposition, the sample has been exposed to molecular deuterium (D_2) for 5 minutes at a pressure of 1.0×10^{-7} mbar, while recording the sensor resistance. After subtracting the thermalization background,

the sensor temperature variation due to D_2 adsorption can be obtained, as shown in Figure 1.1, adapted from Ref. [1].
Finally, a TDS measurement has been performed, and from the detected desorption temperature ($T_p \simeq 469$ K), extracted from the TDS spectrum vs. temperature, the desorption energy barrier E_d has been estimated. E_d corresponds to the average binding energy for the adsorption of deuterium molecules on titanium, which turns out to be $E_b \simeq 1.3$ eV/molecule. The amount of desorbed (and therefore stored) D_2 has been estimated from the TDS spectra (vs. time) as well: $n \sim 1.7 \times 10^{-10}$ mol or $N \sim 1 \times 10^{14}$ D_2 molecules. The heat released during the adsorption process has been estimated: $H_r = n \cdot E_b \simeq 22 \pm 1\,\mu$J. This value is in good agreement with that obtained from the analysis of the calorimetric data: $H_r \simeq 23 \pm 5\,\mu$J [1].

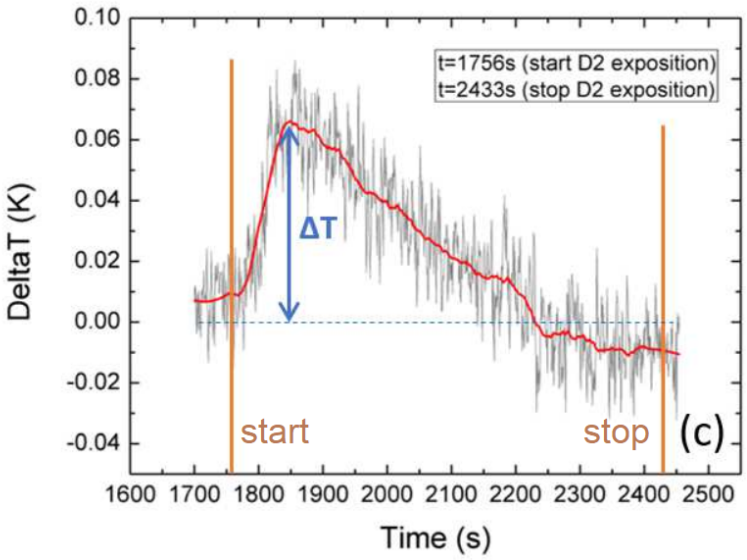

Figura 1.1: Figure adapted from [1]. Sensor temperature variation during D_2 exposure to the Ti layer (Red line: smoothing). $\Delta T = 0.065$ K is clearly detected.

In conclusion, the developed sensor turned out to have a sensitivity of ~ 0.03 mΩ for the resistance variation, which corresponds to a sensitivity of ~ 10 mK

for the temperature variation and $\sim 5\,\mu$J for the energy release. Besides that, because of its non-destructive, real-time and scalable characteristics, this original technique introduces a useful and reliable new way to measure the amount of adsorbed gas in a solid-state system. Moreover, such a sensor can be used to investigate, besides graphene, novel 2D materials, but is also suitable for use in several other applications where small resistance or temperature variations need to be detected.
The weak spot of this gold film thermometer is its substrate: indeed the Au film (20 nm-thick) has been deposited on an amorphous SiO_2 layer (280 nm-thick), which covers the top surface of a silicon wafer of $\sim 300\,\mu$m. The STM analysis of the sample (before the graphene transfer and the titanium deposition) reveals an atomically rough gold surface (see Ref. [1]), which prevents the user from taking advantage of the STM capability. For this reason, in this thesis a new substrate is studied: a *muscovite mica substrate* would improve the sensor sensitivity (because its thermal conductivity is about 300 times lower than silicon one) and would allow to fully exploit the STM capability.

1.3 Muscovite Mica

Mica, the well-known layered silicate mineral, was once regarded as a natural resource of tremendous importance. In 1945, researchers for the (then) National Bureau of Standards declared it "one of the most important strategic minerals in time of war, and indispensable in some modern applications in time of peace" [10]. While it has largely been replaced by other materials in its former applications in industry, such as dielectric in capacitors, and as insulator in home electrical appliances (as hot plates, toasters, and irons), it continues to be used in ceramic composites, electrical components, and as an electrical insulator. Moreover, mica products are very stable at high temperatures (over 450°C).
Mica is also used as substrate for evaporated thin films. The following features make it suitable for flexible device applications:

- 2D structure: mica exhibits strong intra-layer but weak inter-layer interactions. Due to the weak van der Waals interaction between layers, it is possible to peel off overlayer from mica creating an unconstrained or free-

standing like overlayer thin film;

- Transparent: a thin mica sheet ($\sim 100\,\mu$m) exhibits extraordinary transmittance in the ultraviolet–visible-infrared range of the electromagnetic spectrum. Therefore mica can serve as very attractive template for a wide range of optoelectronic applications;

- Elastic: its high Young's modulus ($\sim$ 200 GPa in suspended mica nanosheets reported in [11]) validates mica applicability as dielectric substrate in highly demanding mechanical applications. This feature is extremely useful in flexitronics-paper electronics, wearable electronics, conformal electronics and so on;

- Flexible: mica possesses a very high yield strain, and the thickness of a single cleaved mica sheet can be controlled down to few microns by splitting manually or using a scotch tape;

- Chemically inert: the absence of dangling bonds at the surface makes atoms incapable of forming chemical bonds;

- Non-toxic: beneficial in biomedical and wearable applications;

- CTE matched with Si: coefficient of thermal expansion (CTE) of mica matches that of Si;

- Atomically flat surface: this is the key reason for using mica in TEM and AFM. Moreover, epilayers on mica are ideal systems for investigating molecular surface phenomena like adhesion, friction, and colloidal interactions.

Mica is additionally inexpensive and abundant, light-weight and biocompatible: this can have significant impact on bioinspired applications [12] as artificial skin and muscles, prosthetic limbs, soft and humanoid robots, smart clothing and electronic textiles. All these features qualify mica as an optimal substrate for flexible electronics [13].
The continuing interest in mica is primarily based on its characteristics as a highly

anisotropic crystal. Like other layered materials, its properties are governed by the contrast between the strong intraplanar bonding and the much weaker interplanar forces. The anisotropy governs the mechanical properties as well as the optical and electrical characteristics, and is reflected most obviously in the easy cleavage parallel to the basal plane.

The many minerals under the general classification "mica" consist of negatively charged silicate layers, bonded together by interlayer cations. Each layer consists of two tetrahedral (T) sheets sandwiching one octahedral (O) sheet, with apical oxygen atoms shared between the tetrahedral and octahedral sheets. The basal oxygens of the tetrahedral sheets form a hexagonal mesh on the outer surface of the layer, and the interlayer cations sit in the cavities at the centres of the six-membered rings.

Muscovite is a dioctahedral mica, i.e. of the three octahedra which form a repeat unit within the layer, two have octahedral cations (Al^{3+}) at their centres. The repulsion of the cations in adjacent octahedra leads to shifts and twists in the anion bonds, which break the biaxial symmetry of the layer. One fourth of the tetrahedral cations are Al^{3+} rather than Si^{4+}, which gives a net negative charge to the layer and also expands the tetrahedral sheets, forcing the tetrahedra to rotate in the (001) plane to accommodate the smaller dimensions of the octahedral sheet. Potassium cations reside between the layers and bind them together, leading to the chemical formula [15]:

$$KAl_2(AlSi_3)O_{10}(OH)_2.$$

The cations in this formula are written in the order: interlayer cation-octahedral cation-tetrahedral cations. In the most common form of muscovite, successive layers are shifted laterally in alternating directions separated by 120°, leading to a monoclinic crystal structure with two layers per unit cell.
The TOT sandwich units are separated from each other by the van der Waals-gap. These sandwich units have a very strong covalent bonding within them while the sandwich units are weakly held together by K^+ ions along the crystallographic c-axis. Cleavage of mica along this van der Waals gap layer produces two large, atomically flat surfaces, with each surface occupied by equal but randomly distri-

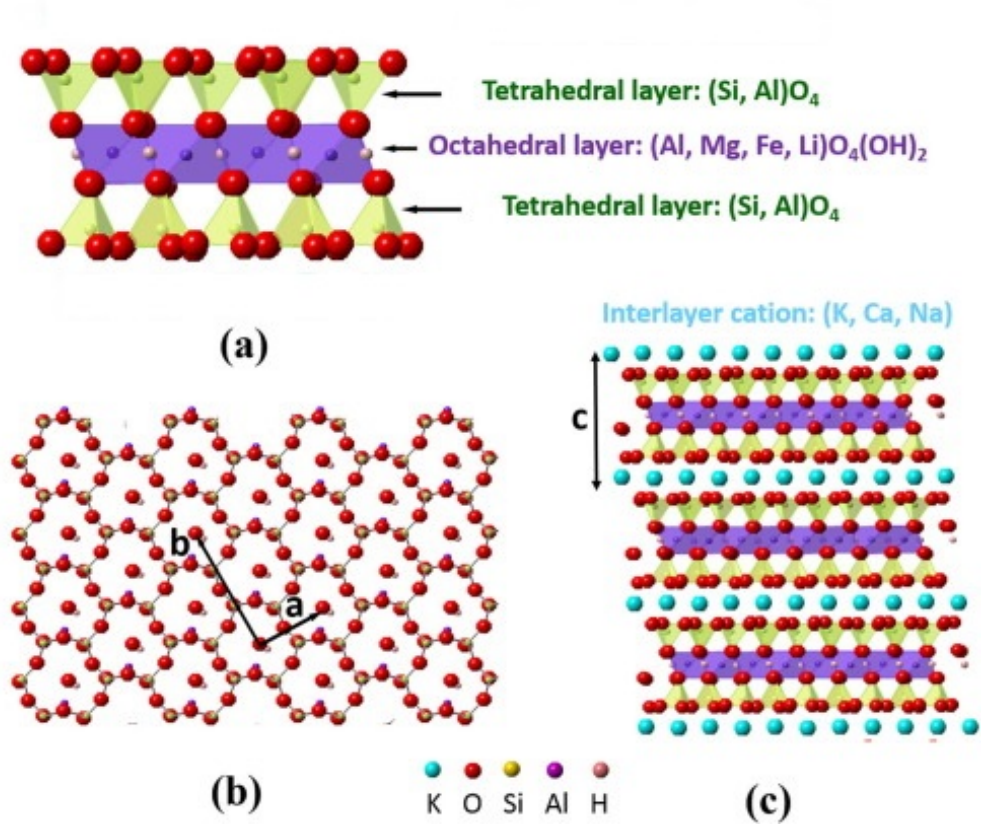

Figura 1.2: (a) The layered mica structural unit (∼1 nm) comprises of two tetrahedral (T) sheets on either sides of an octahedral (O) sheet and these (2:1) layer stacks are bound together by interlayer cations. (b) Basal plane [001] of the cleaved muscovite mica surface with a hexagonally arrayed pattern of oxygen atoms, with the in-plane lattice parameters marked (a= 5.17 Å, b=8.94 Å). (c) [100] projection of muscovite mica where the TOT sandwich units are separated from each other by the van der Waals-gap (c=20.01 Å). Figure adapted from [14].

buted K^+ cations to preserve charge neutrality.
The mica properties we are most interested in are essentially two:

- thermal conductivity, which shows an anisotropic behaviour as well: 4.05 W/m·K parallel to the cleavage planes, and 0.46 W/m·K perpendicular to the cleavage planes [16] (to be compared with silicon one, 156 W/m·K [17]);
- its capability to allow gold surface re-crystallization, in order to exploit the STM potentiality to investigate the sensor surface after an adsorption process, for example.

1.4 Au[111] herringbone reconstruction

Above their melting point, metals are liquids, and their atoms are randomly arranged and relatively free to move. However, when cooled below their melting point, metals rearrange to form ordered, crystalline structures. To form the strongest metallic bonds, metals are packed together as closely as possible.
Several packing arrangements are possible. Instead of atoms, we can imagine marbles that need to be packed in a box. The marbles would be placed on the bottom of the box in neat orderly rows and then a second layer begun. The second layer of marbles cannot be placed directly on top of the other marbles and so the rows of marbles in this layer move into the spaces between marbles in the first layer. The first layer of marbles can be designated as A and the second layer as B, giving the two layers a designation of AB. Packing marbles in the third layer requires a decision. Again rows of atoms will nest in the hollows between atoms in the second layer but two possibilities exist. If the rows of marbles are packed so they are directly over the first layer (A) then the arrangement could be described as ABA. Such a packing arrangement with alternating layers (ABAB) is called *hexagonal close packing* (hcp). If the rows of atoms are packed in the third layer so that they do not lie over atoms in either A or B layer, then the third layer is called C. This packing ABCABC is also known as *face-centered cubic* (fcc). Both arrangements give the closest possible packing of spheres, leaving only about a fourth of the available space empty.
The face centred cubic structure, shown in Fig. 1.3, has atoms located at each

of the corners and the centres of all the cubic faces. Each of the corner atoms is the corner of another cube so the corner atoms are shared among eight unit cells. Additionally, each of the six face centred atoms is shared with an adjacent atom. The fcc unit cell consists of a net total of four atoms; eight eighths from corners atoms and six halves of the face atoms.

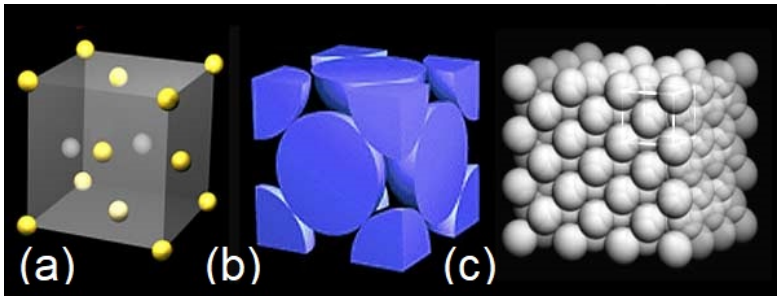

Figura 1.3: (a) Face centred cubic structure, (b) fcc unit cell and (c) a unit cell in a larger section of the lattice.

By contrast, the hexagonal close packed structure of alternating layers is shifted, so its atoms are aligned to the gaps of the preceding layer. The atoms from one layer nest themselves in the empty space between the atoms of the adjacent layer just like in the fcc structure. However, instead of being a cubic structure, the pattern is hexagonal.
The hcp structure has three layers of atoms. In each the top and bottom layer, there are six atoms that arrange themselves in the shape of a hexagon and a seventh atom that sits in the middle of the hexagon. The middle layer has three atoms nestle in the triangular "grooves" of the top and bottom plane. Note that there are six of these "grooves" surrounding each atom in the hexagonal plane, but only three of them can be filled by atoms. As shown in Fig. 1.4(b), there are six atoms in the hcp unit cell. Each of the 12 atoms in the corners of the top and bottom layers contribute 1/6 atom to the unit cell, the two atoms in the center of the hexagon of both the top and bottom layers each contribute 1/2 atom and each of the three atom in the middle layer contribute 1 atom. Fig. 1.4(c) attempts to show several hcp unit cells in a larger lattice.

The packing factor (the volume of atoms in a cell per the total volume of a cell) is 0.74 for both the fcc and hcp structure.

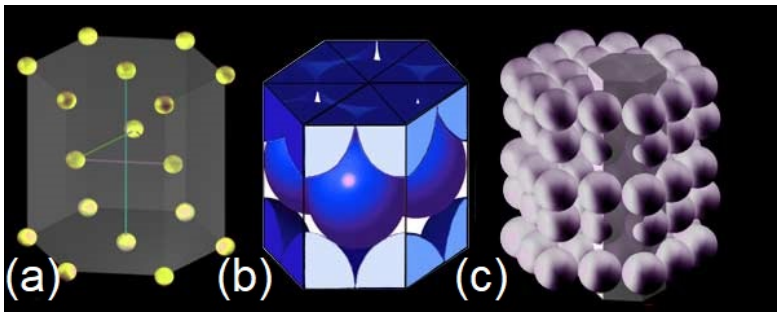

Figura 1.4: (a) Hexagonal close packed structure, (b) hcp unit cell and (c) a unit cell in a larger section of the lattice.

In summary, the face-centered-cubic and the hexagonal-close-packed structures represent two different ways of arranging hard spheres in a regular array to minimize the interstitial volume. The fcc structure corresponds to an ABC$\cdots$ packing of hexagonal layers of atoms, while the hcp structure corresponds to an ABA$\cdots$ packing. For the Au(111) surface, if a continuation of the bulk structure occurs, an ABC stacking is expected (Au is an fcc metal). However, the Au(111) surface reconstructs to the so-called herringbone reconstruction.
The intrinsic tendency for the Au surface layer to contract to higher surface density is opposed by the substrate potential, which tries to keep the top layer in registry (ABC stacking) with the underlying atomic layers. However, if the energy required to occupy the hcp sites (ABA stacking) is close to the energy required to occupy the fcc sites, the energy cost in losing registry is expected to be small and a contraction of the top layer can be favourable, as shown in Fig. 1.5.

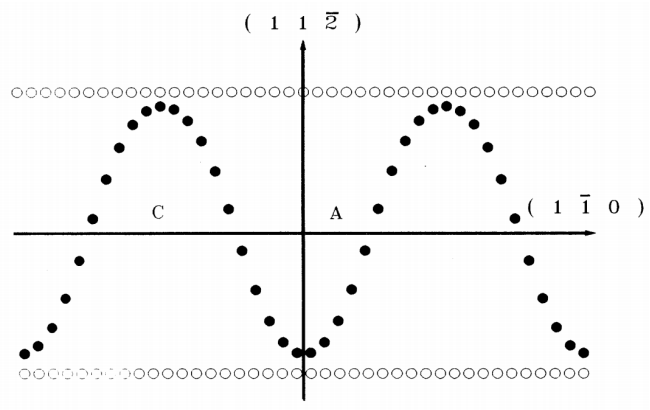

Figura 1.5: One row of surface atoms on the reconstructed Au(111) surface in the $[1\bar{1}0]$ direction. The scale in the $[11\bar{2}]$ direction has been exaggerated. Filled circles denote the position of the reconstructed top layer, open circles at the top denote the positions of fcc sites, and open circles at the bottom denote the position of the hcp sites. C and A mark the regions of ABC and ABA stacking, respectively. Image from [18].

The different widths of the two domains (fcc and hcp) reflect the difference in energy of the stacking sites. Indeed, as expected from the bulk lattice, the fcc domain is more favorable [19].
The topography of a clean and well-annealed Au(111) surface is characterized by large, atomically flat terraces, which often extend over many hundred ångstroms [20]. The terraces exhibit a periodic pattern of pairwise-arranged, parallel lines, running in $[11\bar{2}]$ direction (corrugation lines). The distance between neighbored pairs, in $[1\bar{1}0]$ direction, amounts to $\sim$63 Å; the individual lines within a pair are about 44 Å apart. The corrugation amplitude amounts to $\sim 0.20 \pm 0.05$ Å, while the depression of the narrow regions between the two lines of each pair is less pronounced, $\sim 0.12 \pm 0.05$ Å [20, 21].

High-resolution STM images of the surface, such as the one presented in Fig. 1.6 from Ref. [20], reveal an additional, more dense corrugation, superimposed over the long-wave corrugation of the reconstruction. From the hexagonal arrangement of the minima and the distance of $2.7 \div 2.9$ Å between neighboring minima, these have been attributed to the atomic structure of the surface [20, 22]. Atomic

resolution images of the surface have allowed the direct determination of the unit cell of the reconstructed layer, which is marked by a rectangle in Fig. 1.6. The lattice vectors are given by the connection between adjacent main minima (63 Å in the $[1\bar{1}0]$ direction), and by the connection between next-neighbor $[1\bar{1}0]$ rows of Au atoms (4.7 Å in the $[11\bar{2}]$ direction), thus forming a unit cell of 63×4.7 Å^2 [20, 21, 23].

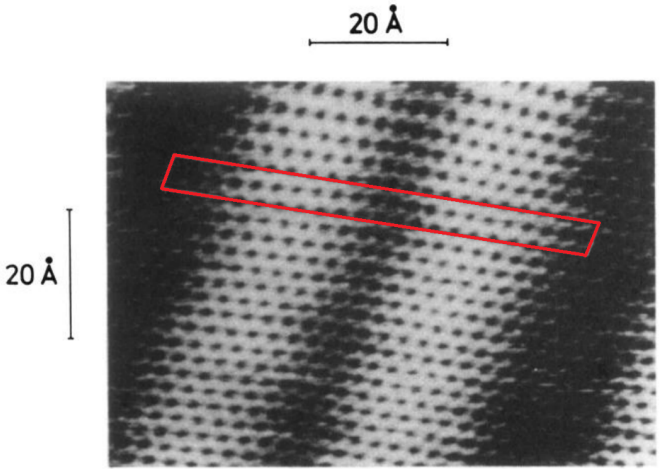

Figura 1.6: Atomic resolution STM image of the reconstructed Au(111). The unit cell is marked in figure. Image from Ref. [20].

Furthermore, STM images of the gold surface reveal three different rotational domains (two of them are shown in Fig. 1.7(a)). They often coexist on a single terrace, especially on larger ones. In most cases, the transition from one domain to another one occurs by a correlated bending of the corrugation lines by 120°. Usually, an additional long-range periodicity in the reconstructed layer is observed. Entire sets of corrugation lines change their orientation in a zig-zag pattern by ±120°, and thus form a periodic sequence of domain boundaries. A more detailed inspection of the rotational domain boundaries reveals that the corrugation line pairs are characteristically deformed in the vicinity of the bending points, i.e., near the domain boundaries. The distance between the lines is either increased

or decreased, but they never bend exactly parallel (red rectangle in Fig. 1.7(a)). In addition, the corrugation amplitude of the reconstruction is often increased in this area [20].

The presence of domain boundaries does not necessarily correspond to a well-ordered zig-zag arrangement of the corrugation lines (like patterns in Fig. 1.7(a)). The corrugation lines can collectively change their direction by 120° by forming a complicated pattern of entangled lines, as shown in Fig. 1.7(b). A novel feature in this image is presented by the U-shaped connections between neighbouring corrugation lines. These "U" can connect either both lines in a pair (red box in Fig. 1.7(b)) or lines of adjacent pairs (yellow box in Fig. 1.7(b)).

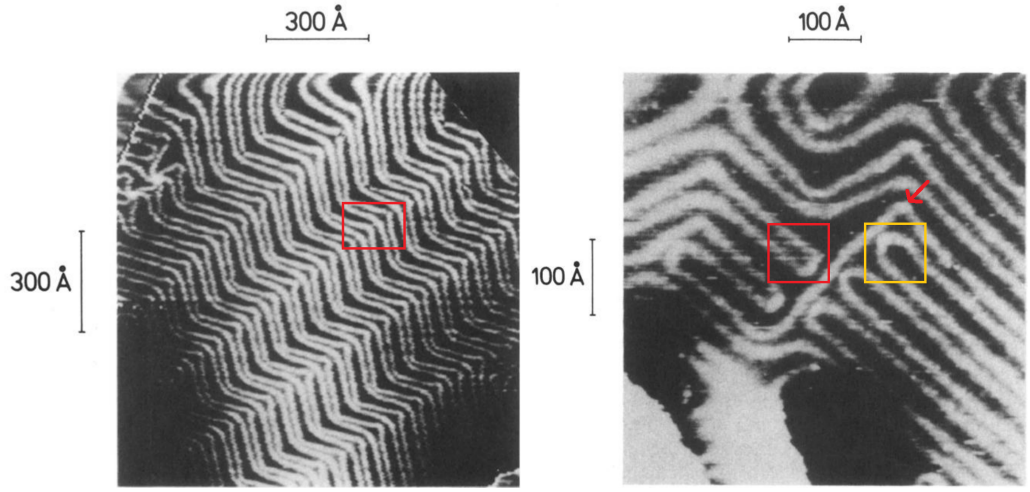

Figura 1.7: (a) STM image of periodic rotational domains in the reconstructed Au(111) surface. Note the non-parallel arrangement of the corrugation lines at the bending points, highlighted by the red box. (b) STM image of U-shaped connections of two adjacent corrugation lines, terminating a line pair. Connections occur either between lines of one pair (red box) or between lines of two neighboring pairs (yellow box). Images from Ref. [20].

A U connection of neighbouring lines corresponds to the termination of either

a fcc or a hcp region at this position. Since the minima between the corrugation lines are associated with fcc and hcp stacking regions, two types of U connections cannot exist in the direct neighbourhood, since areas surrounding the respective U termination correspond to different stacking regions. Therefore, adjacent U connections of different type must be separated by an additional transition region, equivalent to a single corrugation line in between, as shown in Fig. 1.7(b) (red arrow).
Because of the long-range strain in the topmost layer accompanying the reconstruction surface, defects such as steps are expected to play a major role for the formation and ordering of the reconstruction. However, it has been noticed that frequently the corrugation lines, and thus the reconstruction, proceed straight over the monoatomic steps, without any apparent lateral displacement or even a change in direction at the step edge (see Fig. 1.8). This requires sufficiently strong interactions between the topmost reconstructed layers on both sides of the step, which presumably are mediated by the second layer of the upper terrace.

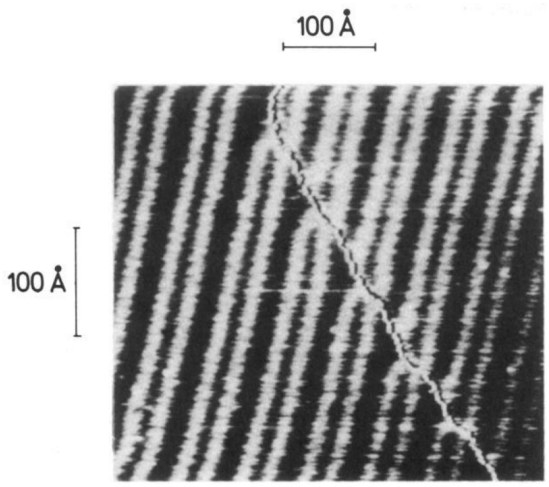

Figura 1.8: STM image of the pairwise-arranged corrugation lines on the reconstructed Au(111) surface. A monoatomic step passes diagonally through the image and is crossed by the reconstruction. Image from Ref. [20].

The transmission of strain, from one terrace to another one, can be rationalized in the framework of the stacking-fault-domain model of reconstruction [20]. If the corrugation lines pass over a step, atoms in the hcp regions of the reconstructed lower terrace have to connect to fcc atoms in the same layer, right at the step edge. This necessitates the formation of domain boundaries ("transition regions") in the hcp regions, along the steps: i.e. the hcp regions of the lower terrace must be terminated by a U connection right at the step edge. However, a slight distortion in that layer, on the other side of the step edge (or right at the step edge), caused by the presence of the topmost reconstructed layer in the upper terrace, could determine the arrangement of the transition regions along the step, allowing the reconstruction to cross the surface steps without any change.
All these features will be recognized in the STM images recorded with our samples.

1.5 Gold thin film on mica

There has been considerable interest in producing thin, highly cristalline metal films, for both scientific investigations and industrial applications [24–26]. Thin metal films offer several advantages over metal single crystals for scanning probe experiments. For example, thin films can be directly prepared in vacuum, thereby avoiding the possibility of contamination from polishing or transfer trough the atmosphere, and the cost is usually a small fraction of the corresponding single crystal [27]. Thin gold films are used in many industrial processes, including the manufacturing of circuits boards and sensors [28], due to the possibility to form patterns via photoresist and stamping methods [29, 30]. For these and other applications, the preparation of high quality gold thin films is essential.

The preparation of high quality thin films is dependent upon the precise control of temperature, pressure, growth rate, cleanliness and thickness. The essential requirements for the production of gold thin films are the employment of the best possible vacuum (1×10^{-5} mbar minimum), a clean chamber, a smooth dry substrate (e.g. mica) and an appropriate combination of substrate temperature and deposition rate.

For very thin films (less than 1 μm-thick), it is reasonable to expect the topography of the substrate to be reproduced in the gold film. Both fused silica glass and quartz have been employed as substrates for thin films [25, 26, 31]; however, these substrates are relatively rough, and usually require an adhesion promoter, such as chromium or titanium, to produce films with good mechanical properties [27]. Bulk mica is a "sheet" silicate that has a layered structure, as explained in section 1.3. Cleavage of mica parallel to these sheets yields an atomically flat surface, which, if cleaved in air, is quickly covered with water. In order to promote adhesion and two-dimensional growth, water must be removed either chemically, by the use of an adhesion promoter [25,32], or physically, by heating in vacuum.

The most important factor for the production of high quality thin films of gold on mica is the avoidance of contaminants from the growth chamber. Indeed, in addition to pump back streaming (a drawback of oil sealed vacuum pumps), a normal laboratory environment offers several potential contaminants such as dust, fingerprints, and airborne organic chemicals. In order to prevent contamination, all vacuum components must be handled with clean room gloves and the evaporation chamber must be cleaned regularly, or at least whenever the gold films are observed to contain impurities.

Generally thermal annealing of metal films causes the grain boundaries to diffuse so that grains can merge to produce larger grains [33]. Moreover, in Ref. [27] it is shown that flame annealing with a butane micro-torch can also remove moderate amounts of contaminants from the surface of gold films.
There are numerous reports describing gold deposition on mica [25, 34–37]. Unfortunately, these reports have proven to be difficult to assemble into a unified, self-consistent picture; consequently, preparing high quality gold films is a nontrivial obstacle for doing research involving these materials. However, one thing is certain: Au deposition on a freshly cleaved, heated, mica substrate produces very large grains of gold. Besides, the annealing procedure, performed either with a butan torch (as in Ref. [27]) or in the UHV chamber (as in Ref. [34]), allows to obtain films that appear completely crystalline and [111] terminated. Indeed, STM images show that the gold grains exhibit the well-known *herringbone reconstruction*.

Experimental Details 2

In this chapter, the experimental methods and apparatus used to perform our investigation are described.
All experiments are performed in an Ultra High Vacuum (UHV) environment (UHV chamber of a RHK Technology Scanning Tunneling Microscope), so, at the beginning, the UHV conditions are explained and justified. Besides a Scanning Tunneling Microscope (STM), the RHK Technology Scanning Tunneling Microscope system is equipped with deuterium and nitrogen gas inlets, a Residual Gas Analyser (RGA), titanium and lithium evaporators, Low Energy Electron Diffraction (LEED) and Auger Electron Spectroscopy (AES) systems, and a thermal hydrogen cracker. In particular only the instruments actually used will be described in depth.
In this chapter, the thermal evaporation procedure, exploited for the sensor fabrication, is described.
Finally, the presentation of the experimental apparatus will be concluded with a short explanation of the setup used for the sensor resistance measurements.

2.1 Ultra High Vacuum (UHV) system

In order to investigate a solid surface on an atomic scale, the interaction between the surface and the reaction species from the gas environment should be low to avoid contaminations, which can change the surface conditions. That is why all

measurements presented are performed in an ultra high vacuum environment. One of the crucial factors in determining how long a surface can be maintained clean is the number of gas molecules impacting on the surface per unit time per unit area of surface, that is the incident flux [38]:

$$F = \frac{1}{4} n \bar{v} \tag{2.1}$$

where n is the molecular gas density and $\bar{v}$ is the average molecular speed. The molecular gas density can be approximated with the ideal gas equation:

$$n = \frac{N}{V} = \frac{P}{k_B T} \tag{2.2}$$

where P is the pressure, k_B is the Boltzmann constant and T is the temperature. The mean molecular speed is obtained from the Maxwell Boltzmann distribution of gas velocities $f(v) = (m/2\pi k_B T)^{3/2} exp(-mv^2/2k_B T)$ by integration:

$$\bar{v} = \int_0^\infty v f(v) dv = \sqrt{\frac{8 k_B T}{m\pi}} \tag{2.3}$$

where m is the molecular mass.
Combining the equations (2.2) and (2.3), Eq. (2.1) can be rewritten as:

$$F = \frac{P}{\sqrt{2\pi m k_B T}} \tag{2.4}$$

From Eq. (2.4) we can calculate two useful parameters:

- $\lambda = 1/(\sqrt{2} n \sigma)$, the mean free path of a molecule in the gas phase above the surface,
- $\tau = n_0/F$, the time required to form one monolayer of adsorbate,

where σ is the collision cross section and n_0 is the number of atoms in a monolayer.
Therefore, the useful parameters for defining the vacuum are: the molecular density n, the mean free path λ and the monolayer formation time τ. They are listed

in Table 2.1 for different levels of vacuum.
Once the pressure in a vacuum system has reached high vacuum levels, most gas particles reside on the walls of the system; thus the pressure in the system is determined by the equilibrium between the adsorption and desorption of gas particles from the surfaces of the walls. At a gas pressure of 1.3×10^{-6} mbar, it only takes 2.2 seconds to create a monolayer of gas on the walls, while at 1.3×10^{-12} mbar it will take 25 days! This explains why surface analysis equipment usually operates in UHV environment.

Vacuum level	P (mbar)	n (cm^{-3})	λ (cm)	τ (s)
Rough	10^3	$2.5 \cdot 10^{19}$	$6.7 \cdot 10^{-6}$	$2.9 \cdot 10^{-9}$
($> 10^{-3}$) mbar	1.3	$3.3 \cdot 10^{16}$	$5.1 \cdot 10^{-3}$	$2.2 \cdot 10^{-6}$
High	$1.3 \cdot 10^{-3}$	$3.3 \cdot 10^{13}$	5.1	$2.2 \cdot 10^{-3}$
($10^{-3} \div 10^{-9}$) mbar	$1.3 \cdot 10^{-6}$	$3.3 \cdot 10^{10}$	$5.1 \cdot 10^{3}$	2.2
Ultra High	$1.3 \cdot 10^{-9}$	$3.3 \cdot 10^{7}$	$5.1 \cdot 10^{6}$	$2.2 \cdot 10^{3}$
($< 10^{-9}$) mbar	$1.3 \cdot 10^{-12}$	$3.3 \cdot 10^{4}$	$5.1 \cdot 10^{9}$	$2.2 \cdot 10^{6}$

Tabella 2.1: Useful vacuum parameters: pressure interval P, molecular density n, mean free path λ, and monolayer formation time τ for different levels of vacuum [39].

High vacuum levels require the use of special materials of construction, as 304 stainless steel, suitable for its characteristics of low gas permeability, non-magnetic, resistance to corrosion, and ability to take a high polish. Commonly used materials are copper, aluminium, and refractory metals (used for evaporators and sample holders) such as tungsten, while different types of ceramics are used for electrical insulation inside the vacuum chamber. Finally, pyrex is frequently employed for the construction of window flanges, because of its low gas permeability and good vacuum characteristics. Besides, fittings and gaskets used between components in a UHV system must prevent even trace leakage. Therefore, nearly all such fittings are ConFlat metal flanges, with knife-edges on both sides cutting into a soft gasket, typically copper.
To reach the UHV conditions the system needs to be *baked*, i.e. heated up to 150°C (this is the maximum rating for our RHK system). That is because water molecules and rest gas are generally adsorbed on the chamber walls. The vapour pressure trend of the water is exponential with temperature, so water slowly desorbs from the chamber, but the time needed to pump it away is very long at room temperature. Therefore the bakeout process accelerates the outgassing process.
The UHV condition, once reached, must be preserved. For this purpose, there is

a specific pumping system which allows to obtain and maintain the vacuum in the chamber.

2.1.1 Pumping system

To reach UHV condition, pressure must be reduced by $13-14$ orders of magnitude (from $P_{atm} = 1013$ mbar to $P_{UHV} = 10^{-10} \div 10^{-11}$ mbar). The pumps used to this end are usually three.
The most common pumps used to get rough vacuum ($10^{-2} - 10^{-3}$ mbar) are rotary pumps and *scroll pumps*. In our system, we use the latter because they are oil-free. In a scroll pump the gas enters the inlet port and is trapped in between two interleaving scrolls, one of which is fixed, while the other orbits eccentrically without rotating. The gas is compressed by the rotation of the eccentrically mounted motor and expelled into atmosphere through the exhaust discharge valve.
The second step is high vacuum (down to 10^{-8} mbar), achieved using a *turbomolecular pump*. The working principle of this pump is to transfer momentum in the direction out-of-the chamber to gas molecules, by repeated collision with the rapidly moving surfaces of a rotor. The surfaces of the rotor, usually disk-shaped, form, with the stationary surfaces of a stator, intervening spaces in which the gas is transported to the backing port. In other words, as the gas molecules enter through the inlet valve, they hit the angled blades of the rotor, which transfer momentum to the particles, in the direction of the holes in the stator. This carries them to the next stage, where they collide again with the rotor surface, and finally are exhausted through the foreline. The performance of a turbomolecular pump is strongly related to the rotation frequency of the rotor. In fact, as revolutions per minute (rpm) increase, the rotor blades deflect more. The operational frequency of our turbomolecular pump is 1200 rpm.
Finally, ultra-high vacuum (down to 10^{-11} mbar) is achieved using an *ion pump*, which operates via ionization and adsorption of residual gas molecules.
The pump configuration consists of two titanium plates, acting as cathode, mounted close to several short stainless steel tubes, acting as anode. A strong magnetic field, parallel to the tubes' axes, is used to contain and guide electrons (generated by applying high voltage to the electrodes) within the circular anode rings. As

the gas molecules move into the anode assembly, they are struck by electrons, and thus ionized; so they are pushed towards the cathode plates by the high voltage field out of the anode tube. In the physical impact (sputtering) cathode material (in our case Ti atoms) is ejected toward the anode tube and the positive gas ions can either react with the cathode, forming new solid compounds, or acquire electrons and be reflected toward the anode assembly. These reflected ions still have enough energy to implant themselves physically in the pump surface and stop contributing to the vacuum environment pressure.
Titanium Sublimation Pumps (TSP) are usually present in UHV systems. A TSP consists of a titanium filament through which a high current (typically about 40 A) passes in order to sublimate titanium. Hence the surrounding chamber walls become coated with a thin film of clean titanium, which reacts with the residual gas molecules in the chamber, forming stable and solid products and therefore reducing the gas pressure in the chamber. Such titanium film acts for a certain time beyond which it is no longer clean and active. So this procedure needs to be periodically repeated, in order to deposit new clean Ti layers.
The UHV system used for this thesis consists of three chambers: the *load lock*, the *preparation (or prep) chamber* and the *STM chamber*.
The load lock is a small chamber used for loading and removing samples and tips without bringing the entire system to atmospheric pressure. This chamber is pumped down to $\sim 10^{-8}$ mbar (in about 8 hours) by a turbomolecular pump backed by a scroll pump, and is separated from the preparation chamber by a manual gate valve.
Once a pressure of $\sim 10^{-8}$ mbar is reached, the sample can be moved through the open valve into the preparation chamber, which is pumped down to $\sim 10^{-10}$ mbar by an ion pump. The prep chamber is equipped with deuterium and nitrogen gas inlets, a Residual Gas Analyser, titanium and lithium evaporators, Low Energy Electron Diffraction (LEED) and Auger Electron Spectroscopy (AES) systems, and a thermal hydrogen cracker. The experiments of this thesis, i.e. the calibrations, the LEED analysis, the calorimetric and the TDS measurements have been performed in the preparation chamber. Whereas, the STM characterization has been done in the STM chamber, separated from the preparation chamber by another manual gate valve, and pumped down to a pressure of the order of 10^{-11} mbar by a second ion pump. Both the preparation and the STM chambers have

a titanium sublimation pump.

2.1.2 Pressure measurement: Ionization Gauge Theory of Operation

Instruments used to measure and display pressure are called *pressure gauges* or *vacuum gauges*. Ionization gauges are the most sensitive gauges for very low pressures (high vacuum). The functional parts of a typical ionization gauge are the filament (cathode), grid (anode) and ion collector, shown schematically in Fig. 2.1. These electrodes are maintained by the gauge controller at +30, +180, and 0 Volts, relative to ground, respectively.

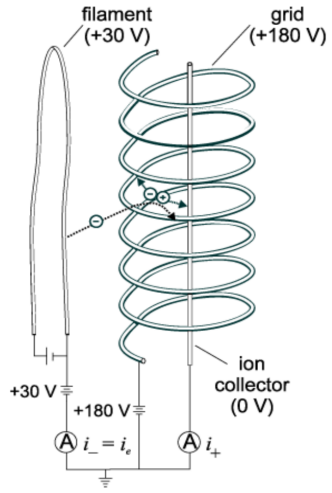

Figura 2.1: Ionization Gauge Schematic, from Ref. [40].

The filament is heated to such a temperature that electrons are emitted, and accelerated toward the grid by the potential difference between the grid and filament. Most of the electrons eventually collide with the grid, but many first traverse the region inside the grid one or more times. When an energetic electron collides with a gas molecule, an electron may be dislodged from the molecule, leaving it with a positive charge. Most ions are then accelerated to the collector. The rate at which electron collisions with molecules occur is proportional to the density of gas molecules, and hence the ion current is proportional to the gas density (or pressure, at constant temperature). The amount of ion current for given emission current and pressure depends on the ion gauge design. The ion gauge controller varies the heating current to the filament to maintain a constant electron emission, and measures the ion current to the collector. The pressure is then calculated from these data [40].

2.2 Residual Gas Analyzer (RGA)

Complete characterization of a vacuum environment requires the detection of all component gases present, as well as measurement of the total pressure. The instrument used for this purpose is called Residual Gas Analyzer or Partial Pressure Analyzer. A Residual Gas Analyzer is a mass spectrometer of small physical dimensions that can be connected directly to a vacuum system and whose function is to analyze the gases inside the vacuum chamber. The principle of operation is based on the ionization of a small fraction of the gas molecules: the resulting ions are separated, detected and measured according to their molecular masses. RGA's are widely used to quickly identify the different molecules present in a gas environment and, when properly calibrated, can be used to determine the concentrations or absolute partial pressures of the components of a gas mixture.

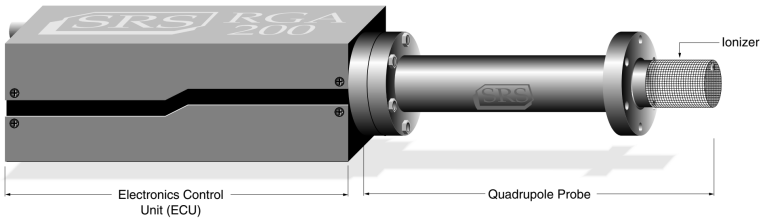

Figura 2.2: Scheme of the SRS Residual Gas Analyzer, composed of an Electronic Control Unit (ECU), connected to the PC, and a quadrupole probe.

We use an SRS RGA which consists of a quadrupole probe and an Electronics Control Unit (ECU) which mounts directly on the probe flange and contains all the electronics necessary to operate the instrument.
The total probe equipment consists of three parts: the ionizer (electron impact), the quadrupole mass filter and the ion detector. All of these parts reside in the vacuum space where the gas analysis measurements are performed. The detector measures the ion currents directly, by the use of a Faraday Cup, or it can measure an electron signal proportional to the ion current by using an optional electron multiplier detector. However, when the pressure is lower than 10^{-7} mbar, as in

our case, the Electron Multiplier upgrade is recommended. The Multi-Channel Continuous Dynode Electron Multiplier (CDEM) consists of a conical system made out of a special resistive glass. When the cone is biased negatively relative to the back end, positive ions are very efficiently attracted and strike the cone at high velocity, producing electrons by secondary electron emission. This process continues, and depending on the bias voltage applied, up to 10^7 electrons come out at the back end and are picked up by a grounded plate.
It is worth noting that the quadrupole mass filter must operate in a vacuum environment, at a pressure lower than 10^{-4} mbar, in order to avoid collisional scattering between the ions and the neutral gas molecules.
Since the gain degradation cannot be avoided, a careful calibration of the measurement parameters is fundamental before using the RGA.

2.2.1 Residual Gas Analyzer Calibration

The Residual Gas Analyzer (RGA) is controlled via a LabView program which converts the current reading related to the mass under analysis into the partial pressure of the molecular gas having that mass. Before using the RGA we need to calibrate it, opening the molecular deuterium bottle until the pressure gauge in the UHV chamber reads a stable partial pressure of D_2 of around 9×10^{-10} mbar. In the meanwhile we record the reading current of the RGA and obtain the conversion coefficient:

$$C_{RGAsignal \to D_2 PartialPressure} = (3.04 \pm 0.06) \cdot 10^{-2} \text{ mbar/A} \tag{2.5}$$

The above equation will be used to convert the current signal recorded during our Thermal Desorption Spectroscopy (TDS) measurements in partial pressure, in order to analyse the TDS spectra.

2.2.2 Thermal Desorption Spectroscopy

In chapter 4 we will test our thermometer in a hydrogen adsorption experiment. The idea is to detect and analyse the exothermic reaction that binds atomic hydrogen to gold atoms via two processes. The hydrogen adsorption is detected by

calorimetric measurements, from which the total heat released H_r can be extracted, as in [1]. The subsequent hydrogen desorption is investigated by thermal desorption spectroscopy, in order to estimate the average binding energy and the amount of hydrogen adsorbed. The aim is to compare the heat release obtained from the calorimetric technique with that one obtained from the desorption analysis.
In order to determine the binding energy of H atoms and the amount of adsorbed hydrogen we can heat the surface and measure the desorbed atoms with a mass spectrometer. The desorption spectrum, that is the pressure-time curve, allows us to know the quantity of gas desorbed, the activation energy of desorption and the order of desorption, which gives information on the kinetics of the process.
After making some assumptions, thermal desorption can be described with a simplified Arrhenius equation:

$$N(t) = -\frac{d\sigma}{dt} = \nu_n \cdot \sigma^n \cdot exp\left(-\frac{E_d}{RT}\right) \tag{2.6}$$

where:

- n is the order of desorption
- σ is the surface coverage
- ν_n is the rate constant
- E_d is the activation energy of desorption
- R is the gas constant

We have assumed that the rate constant and the activation energy of desorption are independent of the coverage. In case of linear heating rate, following the relation $T = T_0 + \beta t$ (β= heating rate), and for a pump rate large enough to neglect the re-adsorption during the desorption process (as in our case), we can solve Eq. (2.6) and determine the activation energy of desorption for $n = 1$ (from Ref. [41]):

$$\frac{E_d}{R \cdot T_p^2} = \frac{\nu_1}{\beta} \cdot exp\left(-\frac{E_d}{R \cdot T_p}\right) \tag{2.7}$$

where T_p is the temperature at which the desorption rate is maximum. (It is known that hydrogen desorption on Au(111) follows first-order desorption kinetics, see Ref. [42] for details). Defining τ_m as the time from the start of the desorption ramp to the moment at which T_p is reached, we have:

$$\frac{E_d}{R \cdot T_p} = A\tau_m exp\left(-\frac{E_d}{k_B \cdot T_p}\right) \tag{2.8}$$

where $k_B = 8.625 \cdot 10^{-5}$ eV·K^{-1} is the Boltzmann constant and A is the Arrhenius constant, whose typical value is 10^{13} s^{-1}.
Therefore, by analysing the TDS spectrum it is possible to obtain the average binding energy per atom from the activation energy of desorption.
The amount of desorbed (and therefore previously stored) hydrogen can be estimated from the TDS spectra showing the partial pressure of atomic hydrogen as a function of time.
At a given pressure, if we assume no re-adsorption on the sample during the desorption measurement and we neglect the adsorption on the walls of the chamber (see Ref. [41]), the amount of desorbed gas is equal to the pumping speed of the vacuum system S (in L/s). This parameter depends on the gas and on the base pressure. We can extract the effective pumping speed for hydrogen from the datasheet of our Diode Ion Pump (Fig. 2.3). With a base partial pressure in the range of $(0.2 - 0.6) \cdot 10^{-10}$ mbar, we have an effective pumping speed (S) varying from 90% to 110% of the nominal speed, which is 300 L/s. Therefore we use an average pumping speed of 300 L/s.

After the subtraction of the background, the TDS spectrum can be integrated in order to obtain the area under the curve, F (in mbar·s).
From the gas equation we can write:

$$p \cdot V = F \cdot S = n \cdot R \cdot T \tag{2.9}$$

with $R = 8.314$ J·K^{-1}· mol^{-1} the gas constant, and use it to calculate n, the number of moles of desorbed hydrogen and from it the number of atoms N (1 mol= 6.022×10^{23} molecules). In this equation T is the room temperature ($T_{amb} = 295\,K$) and not the sample temperature, which varies from 300 K to 600 K. That

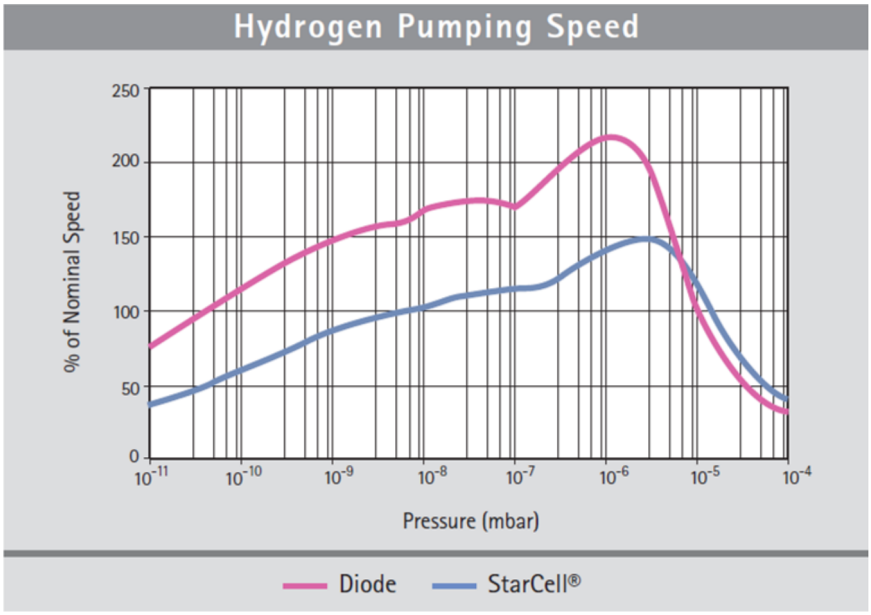

Figura 2.3: Effective pumping speed for hydrogen (Diode Ion Pump).

because the calibration of the RGA has been performed using as reference the total pressure of the chamber, read by the pressure gauge of the UHV chamber, which is thermalized at T_{amb} (see section 2.2).
Finally we can estimate the heat release during the adsorption of atomic hydrogen on gold. It can be obtained by multiplying the average binding energy per atom and the number of hydrogen atoms desorbed: $H_r = E_b \cdot N$.

2.3 Thermal Hydrogen Cracker

Figura 2.4: Scheme of the Tectra thermal hydrogen cracker.

The Tectra h-flux Atomic Hydrogen Source works by thermally dissociating hydrogen in an electron bombardment heated fine tungsten capillary (thermal hydrogen cracker). By bouncing along the hot walls, the molecular hydrogen is cracked to atomic hydrogen.
Equilibrium thermodynamics shows that in the dissociation equation for molecular hydrogen into atomic hydrogen, the dissociation fraction becomes very large at low pressures and high temperatures, reaching values >95% at temperatures of ∼1800 K and pressures lower than 10^{-8} mbar. Although flowing through the tungsten tube, the hydrogen molecules make a number of wall collisions establishing a quasi-equilibrium, making the above theory applicable.
The power applied to the capillary depends on the values of the high voltage and the emission current. The high voltage is controlled directly by the voltage dial, on the front panel of the power supply. Controlling the emission current is a little more tricky, because it depends on the temperature of the filament and can only be controlled indirectly by changing the filament current. For user convenience,

the power supply can regulate the heating of the filament to hold the emission current constant. The filament is conditioned and ready for use when $\sim$ 9 Amps (filament current) and 1 kV have been reached, and the chamber pressure is falling again (it is normal that the chamber pressure rises as the filament outgasses).
The Tectra atomic hydrogen source is equipped with a shutter blade at the end of the source, in order to control the gas flow, and with Swagelok fittings useful to connect a suitable water supply, in order to cool the system. As concerns the actual hydrogen supply, a leak valve is slowly opened until the required gas flow is established [43].

2.4 Low Energy Electron Diffraction (LEED)

Diffraction techniques utilizing electrons are widely used to investigate surface structures. From the analysis of the particles/waves elastically scattered by the crystal, structural information can be obtained. The information on the atomic arrangement inside a unit cell is provided by the intensity of the diffracted beams, while the spatial distribution of the diffracted beams provides information about the crystal lattice.
In particular, Low-Enegy Electron Diffraction (LEED) is the principal technique for the determination of surface structures: a collimated electron beam of low energy (20-200 eV) hits the sample surface, thus producing diffracted electrons which are observed as spots on a fluorescent screen.

2.4.1 LEED Theory

For electrons the relationship between energy and wavevector is $E = \hbar^2 k^2/2m$, where $k = 2\pi/\lambda$ and m is the electron mass; we have:

$$\lambda\,[\text{Å}] = \frac{12.264}{\sqrt{E\,[eV]}} \tag{2.10}$$

Therefore, in the typical energy range used in LEED ($\sim$ 20-200 eV) the electrons have a wavelength of 1-2 Åwhich satisfies the atomic diffraction condition: λ is of

the order of the interatomic distances. This is a necessary condition to observe diffraction effects associated with atomic structure.
Electrons are charged particles and thus they interact strongly with the nuclei and the electrons of a crystal via Coulomb forces. Electrons penetrate into the crystal for small distances and elastic electron diffraction is particularly convenient for investigation of surfaces and thin layers.
In periodic systems such as crystals, the occurrence of diffraction peaks requires:

$$\boldsymbol{k_i} - \boldsymbol{k_f} \equiv G \tag{2.11}$$

where $\boldsymbol{k_i}$ is the incident wave vector, $\boldsymbol{k_f}$ is the scattered wave vector and $\boldsymbol{G}$ is a reciprocal lattice vector. Thus a necessary condition for diffraction is that the difference between the incident and scattered radiation wavevectors equals a reciprocal lattice vector [44].
Eq. (2.11) can be written in the form:

$$\hbar\boldsymbol{k_i} = \hbar\boldsymbol{k_f} + \hbar\boldsymbol{G}; \tag{2.12}$$

thus in the scattering process the moment is preserved within reciprocal lattice vectors times $\hbar$.
We can show that the diffraction condition deduced by von Laue (Eq. (2.11)) is equivalent to the intuitive description by Bragg, who considered specular reflection of the incident radiation by a family of lattice planes [44]; as illustrated in Fig. 2.5, the geometrical condition for the coherent scattering from two successive planes (and hence from the whole sequence of parallel planes) requires:

$$2dsin\theta = n\lambda \tag{2.13}$$

where n is a positive integer, λ is the wavelength of the scattered (and incident) wave, θ is the scattering angle and d is the distance between adjacent planes of the family.

Fig. 2.5 also shows the geometrical construction of the vector $\boldsymbol{Q} = \boldsymbol{k_i} - \boldsymbol{k_f}$. Since for elastic scattering $|\boldsymbol{k_i}| = |\boldsymbol{k_f}| = 2\pi/\lambda$, we have:

$$|Q| = 2|k_i|sin\theta = 2\frac{2\pi}{\lambda}sin\theta = n\frac{2\pi}{d} \tag{2.14}$$

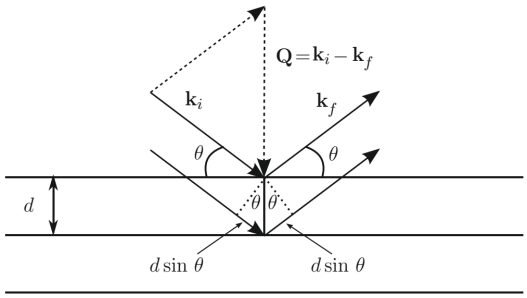

Figura 2.5: Waves reflected from successive planes reinforce if $2dsin\theta$ equals an integer number $n\lambda$ of wavelengths. The geometrical construction of $\boldsymbol{Q} = \boldsymbol{k_i} - \boldsymbol{k_f}$ is also provided. Image from Ref. [44].

where the last equality follows from the Bragg law (Eq. (2.13)).
From Fig. 2.5 it is seen that $\boldsymbol{Q}$ is perpendicular to the family of lattice planes with distance d; furthermore, equation 2.14 shows that the magnitude $|\boldsymbol{Q}|$ is an integer multiple of the quantity $2\pi/d$; these two observations (together with the general properties of real and reciprocal spaces) allow us to conclude that $\boldsymbol{Q}$ must be a reciprocal lattice vector.
In conclusion, the Laue condition (Eq. (2.11)) for occurrence of "diffracted beams" is fully equivalent to the Bragg condition (Eq. (2.13)) for occurrence of "reflected beams", and the expressions diffracted beam and reflected beam in this context become synonymous.
From the Bragg condition (Eq. 2.13)), the possibility of elastic scattering occurs only if $\lambda < 2d$. Thus λ must be of the order of the Å or less. Furthermore λ cannot be much smaller than the interatomic distance, otherwise experimental arrangements at glancing angles are necessary to detect diffraction peaks with small momentum transfer. This restricts the ordinary frequency range of interest to the X-ray region.

2.4.2 Ewald construction

We can consider the following geometrical construction due to Ewald for an easy determination of the occurrence of (elastic) diffraction peaks [44].

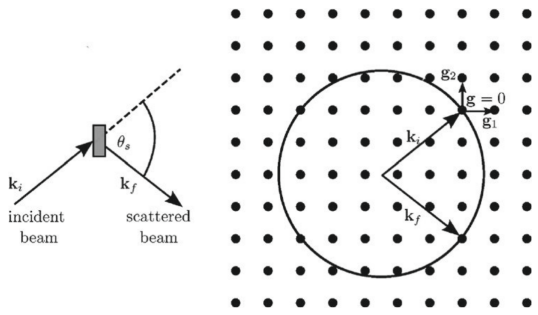

Figura 2.6: Schematic representation of the Ewald construction in the reciprocal lattice (supposed cubic for simplicity) of allowed wavevectors for elastic diffraction. Image from Ref. [44].

Suppose to have an incident monochromatic beam of particles of wavevector $\boldsymbol{k_i}$ and a diffracted beam with propagation wavevector $\boldsymbol{k_f}$. For elastic scattering, the conservation of energy and the conservation of momentum (within reciprocal lattice vectors $\boldsymbol{G}$ times $\hbar$) imply:

$$|\boldsymbol{k_i}| = |\boldsymbol{k_f}| \text{ and } \boldsymbol{k_i} = \boldsymbol{k_f} + \boldsymbol{G} \tag{2.15}$$

The Ewald construction (see Figure 2.6) permits a simple geometrical interpretation of Eq. (2.15).
In reciprocal space, the vector $\boldsymbol{k_i}$ is drawn in such a way that its tip terminates at the reciprocal lattice vector $\boldsymbol{G} = 0$. With the center at the origin of the vector $\boldsymbol{k_i}$, the sphere of radius k_i is drawn; if this sphere intersects, besides $\boldsymbol{G} = 0$, one (or more) points of the reciprocal lattice, conditions (2.15) are satisfied and elastic diffraction is possible. It is evident that diffraction may occur only if the magnitude of k_i exceeds one half of the magnitude of the smallest (non-vanishing) $\boldsymbol{G}$ vector.

2.4.3 LEED setup

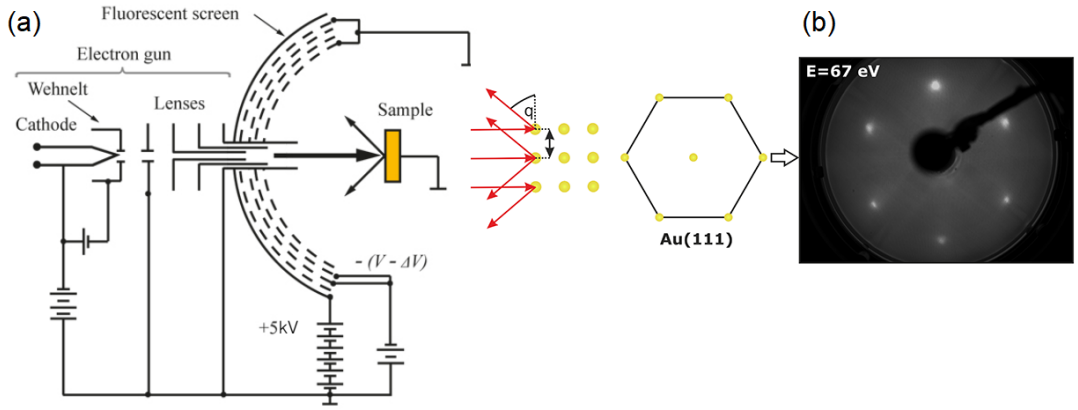

Figura 2.7: (a) Schematic diagram of a standard LEED setup and (b) LEED pattern of a Au(111) reconstructed surface. Image adapted from Ref. [45].

The experimental setup of LEED is schematically represented in Fig. 2.7. The main components of LEED are:

- an electron gun, which produces the low-energy electrons in a collimated beam;
- a sample holder with the sample under investigation;
- an hemispherical fluorescent screen with a set of four grids to observe the diffraction pattern of the elastically scattered electrons (the sample is placed at the center of curvature of the grids and screen);
- a camera connected to a PC in order to observe the diffraction pattern directly on the PC screen.

The electron gun unit consists of a cathode filament with a Wehnelt cylinder followed by electrostatic lenses. The cathode is at negative potential, -V , while the last aperture of the lens, the sample, and the first grid are grounded. The

electrons emitted by the cathode are accelerated to an energy of eV within the gun, and then propagate and scatter from the sample surface in the field-free space. The second and third grids reject the electrons not elastically scattered. The fourth grid is grounded and screens the other grids from the field of the fluorescent screen, which is biased to a high voltage of about +5 kV . Therefore, the elastically scattered, diffracted electrons are re-accelerated to a high energy to cause fluorescence on the screen, so that the diffraction pattern can be observed.

2.5 Scanning Tunneling Microscopy (STM)

The scanning tunneling microscope (STM) was invented and implemented by Binnig and Rohrer who received the Nobel prize in physics 1986 for this invention [46]. The basic principle of the STM is to take advantage from the tunneling electrons to create a map of the density of the states of a surface at a given energy. The resolution of the images obtained with this microscope is usually on the atomic scale and allows to visualize the positions of the atoms on the sample surface. The physical principle on which STM is based is the *tunneling effect*. The concept of tunneling can be explained through an elementary one-dimensional model [47].
In classical mechanics, an electron with energy E moving in a potential $U(z)$ is described by:

$$\frac{p_z^2}{2m} + U(z) = E \tag{2.16}$$

where m is the electron mass. In regions where $E > U(z)$, the electron has a nonzero momentum p_z. On the other hand, the electron cannot penetrate into any region with $E < U(z)$, or a potential barrier. In quantum mechanics, the state of the same electron is described by a wavefunction $\Psi(z)$, which satisfies Schrödinger's equation:

$$-\frac{\hbar^2}{2m}\frac{d^2}{dz^2}\Psi(z) + U(z)\Psi(z) = E\Psi(z) \tag{2.17}$$

Consider the case of a piecewise-constant potential, as shown in Fig. 2.8. In the classically allowed region, $E > U$, and Eq. (2.17) has the following solutions:

$$\Psi(z) = \Psi(0)e^{\pm ikz} \tag{2.18}$$

where

$$k = \frac{\sqrt{2m(E-U)}}{\hbar} \tag{2.19}$$

is the wave vector. The electron is moving (in either a positive or negative direction) with a constant momentum $p_z = \hbar k = \sqrt{2m(E-U)}$, or a constant velocity $v_z = p_z/m$, the same as the classical case. In the classically forbidden region, equation 2.17 has the solution:

$$\Psi(z) = \Psi(0)e^{-\kappa z} \tag{2.20}$$

where

$$\kappa = \frac{\sqrt{2m(U-E)}}{\hbar} \tag{2.21}$$

is the decay constant. It describes a state of the electron decaying in the $+z$ direction. The probability density to observe an electron near z is proportional to $|\Psi(0)|^2 e^{-2\kappa z}$, which has a non-zero value in the barrier region and thus a non-zero probability to penetrate the barrier. Another solution, $\Psi(z) = \Psi(0)e^{\kappa z}$ describes an electron state decaying in the $-z$ direction.

From this elementary model, the tip-vacuum-tip tunneling can be understood (see Fig. 2.9). The minimum energy required to remove an electron from the bulk to the vacuum level is defined as work function ϕ. For materials commonly used in STM experiments, a typical value of ϕ is $\sim$4 eV. Neglecting the thermal energy, the Fermi level is the upper limit of the occupied states in a metal, and its energy is the Fermi energy $E_F = -\phi$. In order to make things simpler, we can assume that the work functions of the tip and the sample are approximately equal. The electrons in the sample can tunnel into the tip and vice versa. Without a bias voltage, there is no net tunneling current, which however occurs applying a bias voltage V. A sample state Ψ_n with energy E_n between $E_F - eV$ and E_F can tunnel into the tip.

If we assume that the bias is much smaller than the work function, $eV \ll \phi$, the energy levels of all sample states of interest are very close to the Fermi level: $E_F \approx -\phi$. The probability w for an electron in the nth sample state to extend to

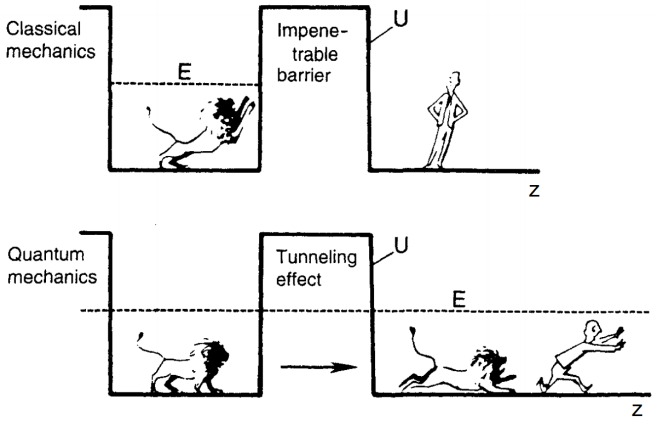

Figura 2.8: The difference between classical theory and quantum theory. In quantum mechanics, an electron has a nonzero probability of tunneling through a potential barrier. Image from Ref. [47].

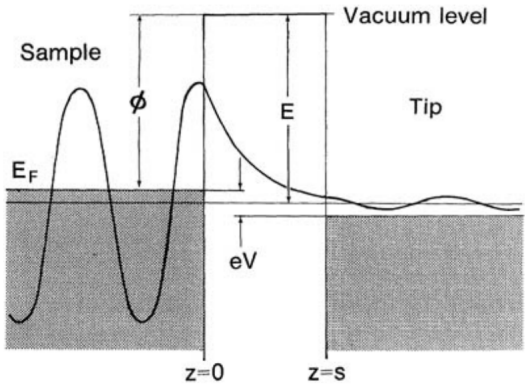

Figura 2.9: A one-dimensional metal-vacuum-metal tunneling taken from Ref. [47]. The sample, left, and the tip, right, are modeled as semi-infinite pieces of free-electron metal.

the tip surface, $z = s$, is:

$$w \propto |\Psi_n(0)|^2 e^{-2\kappa s}, \text{ with } \kappa = \sqrt{\frac{2m\phi}{\hbar}} \tag{2.22}$$

in which $\Psi_n(0)$ is the value of the nth sample state at the sample surface (z=0), and κ is the decay constant of a sample state near the Fermi level in the barrier region. Using eV as unit of the work function, and Å^{-1} as the unit of the decay constant, κ can be estimated as:

$$\kappa = 0.51\sqrt{\phi \text{ (eV)}}\text{Å}^{-1}. \tag{2.23}$$

Typically s is of the order of 10 Åand, considering a typical value for $\phi \sim 4$ eV, the tunneling current decreases by one order of magnitude with a distance increase of 1 Å.
Bardeen's formalism gives a more developed result of the tunneling current I, which in first order approximation is [47]:

$$I = \frac{2\pi e}{\hbar} \sum_{\mu\nu} f(E_\mu)[1 - f(E_\nu + eV)]|M_{\mu\nu}|^2 \delta(E_\mu - E - \nu) \tag{2.24}$$

where $f(E)$ is the Fermi function, $M_{\mu\nu}$ is the tunneling matrix between tip and sample, and V is the bias voltage applied between tip and sample. ν and μ are referred to the sample and the tip, respectively. The meaning of the equation is that the tunneling current is the sum of all tunneling events between the occupied states, $f(E_\mu)$, of the tip and the unoccupied surface states in the energy range from E_ν to $E_\nu + eV$. If the bias voltage polarity is reversed, the occupied and unoccupied states as defined above are inverted. The previous mentioned results are obtained by harnessing the electron tunneling from (to) a very sharp metallic tip (usually tungsten W is used) to (from) a conducting surface, very close to the tip (order of few Å). The tip apex is approximated as a sphere with radius R. The sample surface is scanned by the tip, and the scan allows to obtain a topographical image which can be created recording the tunneling current, or the distance between the tip and the surface corresponding to a constant current.
In *constant current mode*, feedback electronics adjust the height by a voltage to

the piezoelectric height control mechanism [48]. This leads to a height variation and thus the image comes from the tip topography across the sample and gives a constant charge density surface; this means that contrast on the image is due to variations in charge density [49]. In constant height mode, the voltage and height are both held constant while the current changes to keep the voltage from changing; this leads to an image made of current changes over the surface, which can be related to charge density [49].
Each mode has advantages and disadvantages. Constant-height mode is faster because the system doesn't have to move the scanner up and down, but it provides useful information only for relatively smooth surfaces. Constant-current mode can measure irregular surfaces with high precision, but the measurement takes more time.
All the images that we shall display in this thesis are obtained using constant current mode.

In Fig. 2.10 a schematic view of an STM main elements is reported. The STM setup consists of: a scanning tip (usually made of tungsten, as in our case), a piezoelectric controlled scanner, a coarse sample-to-tip control, a vibration isolation system, and computer.
The tube scanner moves the probe tip on the sample, in order to scan the surface, and allows the motion in three orthogonal directions. It consists of a tube made of piezoceramics, covered inside and outside with metal electrodes. A motion in z-direction can be achieved by applying a voltage between the inner and the outer electrodes, while a deflection in xy-direction is induced by voltages of opposite polarity applied to the two opposite outer electrodes.

By moving the tip in z-direction, the tip and the sample are approached up to few angstroms, in such a way that the electron wavefunction in the tip apex overlaps the electron wavefunction of the sample surface atom. Applying a bias voltage between the tip and the sample, an electrical current starts to flow between the tip and the sample surface due to the quantum-mechanical phenomena of the tunneling previously explained. Such tunneling current is amplified by a current amplifier to become a voltage, which is compared with a reference value. The difference is then amplified again to drive the z piezo. If the tunneling current is

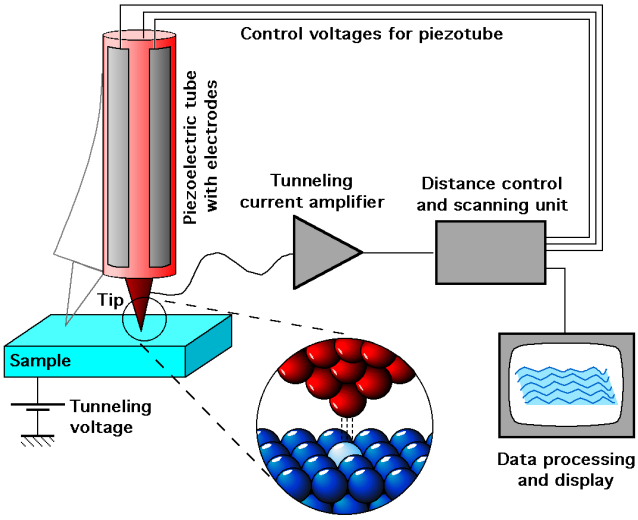

Figura 2.10: Schematic diagram of the scanning tunneling microscope from Ref. [50].

larger than the reference value, then the voltage applied to the z piezo tends to withdraw the tip from the sample surface, and vice versa. Therefore, an equilibrium z position is established when the measured tunneling current is exactly equal to the set point. As the tip scans over the xy plane, a two-dimensional array of equilibrium z positions, representing a contour plot of the equal tunneling-current surface, is obtained and displayed on a computer screen. In such image, the bright areas represent high z values (protrusions), and the dark areas represent low z values (depressions). This makes STM a powerful tool not only to investigate the surface on the xy plane but also in z direction, allowing an height/depth analysis in z.

Current and bias values are important parameters to control during the STM acquisition but also the external conditions must be controlled. Indeed, to achieve atomic resolution, vibration isolation is essential. In order to isolate the STM system as much as possible, the STM unit must be as rigid as possible, and the transmission of environmental vibrations to the STM unit has to be reduced. The vibration isolation system consists, in general, of a set of suspension springs and

a damping mechanism, in order to reduce as much as possible the transmission of vibrations to the system. Moreover, the STM is usually placed on a table in floating condition, to allow isolation from the ground vibrations. The scan occurs in floating conditions in vacuum, to reduce as much as possible the external noise. During the data acquisition, the turbo and scroll pumps are disengaged, and the entire apparatus is floating on a pneumatic vibration isolation system.
The STM experiments can be performed in a variety of environments: in air, in inert gas, in ultra-high vacuum, or in liquids, including insulating and cryogenic liquids, and even electrolytes. The operating temperature ranges from near absolute zero for a low-temperature STM (LT-STM) to a few hundred degrees centigrade for a variable temperature STM (VT-STM).
In our setup, the STM is a variable temperature (from 100 K to 1500 K) ultra high vacuum STM from RHK Technologies. The STM system is a standalone unit mounted on a steel frame, supported by four air legs. A flange on the top holds the scan head and the feedthroughs for electrical contact and temperature measurement. The large flange that supports the microscope contains the motion feedthrough for raising and lowering the sample stage. The entire STM assembly (head+sample stage) can be removed from the chamber by lifting this flange.
The scan head consists of three identical piezoelectric tubes and a "Mexican hat"-shaped body. Three outer tubes are mounted 120° apart on a circle, to form the "legs" of the scan head. Glass balls are attached to the end of each of the legs with an intermediate ceramics adapter. The fourth tube located in the center of the head is the scanning tube which holds the tip. A transverse pin is mounted to the top of the scan head body and is used to pick up the scan head by the head manipulator when it is not sitting on the sample holder. During imaging, the STM head rests on the sample holder which is on the STM stage, in order to allow to the tip to scan the sample surface.
A wobble stick with a fork is used for tip/sample handling with a large range of motion. This allows to the wobble stick to reach the sample stage, the storage elevator, and the tip storage.

2.6 Sample Holder

The sample holder for inserting samples in the RHK system is shown in Fig. 2.11. It consists of a double grooved copper body, useful to clasp it in the sample stage and for its transfer, and a helical top ramp, which acts as base for the scan head during STM imaging, as shown in Fig. 2.11.

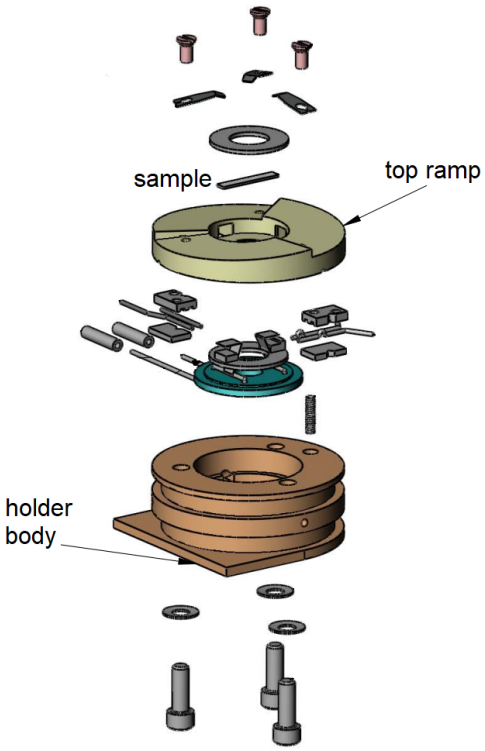

Figura 2.11: Scheme of the sample holder used for the RHK system.

Round or squared flat samples (of maximum dimensions 7 mm x 7 mm) can be mounted in the holder, sandwiched between two sapphire washers in order to be electrically and thermally isolated from the body. The diameter of the round

hole of the washers is 5.35 mm. The sample holder has a built-in thermocouple (TC) which measures the sample temperature. The two leads of the TC stick out on one side of the sample holder. These connections mate with a pair of spring thermocouple contacts on the sample stage, when the sample holder is placed on the stage. In addition, there are two more contacts (additional contacts) on the back of the holder, for electrical contact to the sample. In our experiments we performed a direct current heating of the sample by the use of tantalum foils, mounted at the bottom of the sample holder, which heated a piece of silicon underneath, whose electrical connections (filament contacts) protruded from the side of the holder body, below the TC leads. The tantalum foils were in touch with a piece of silicon underneath our sample, in order to warm it up by direct current heating.

2.7 Thermal evaporation of metals

The most common methods of Physical Vapour Deposition (PVD) of metal are thermal evaporation, e-beam evaporation, plasma spray deposition, and sputtering. Metals and metal compounds can be deposited by PVD. Evaporation occurs when a source material is heated above its melting point in a vacuum chamber. The evaporated atoms then travel in straight line due to a long mean free-path allowed by the vacuum (10^{-5} mbar minimum), and deposit on the substrate. The metal source can be melted by resistive heating, RF heating or by a focused electron beam. The metal evaporation done by resistive heating is usually called thermal evaporation.
The substrates are loaded into a high-vacuum chamber that is commonly pumped with either a diffusion pump, a cryo-pump, or a turbomolecular-pump, as in our case. The material to be deposited is loaded into a heated container called the crucible (boat). Boats are usually made from tungsten, tantalum, molybdenum, or ceramic materials capable of withstanding high temperatures. They can be heated very simply by means of an embedded resistance heater and an external power supply. As the material in the crucible becomes hot, it increases its vapour pressure. Since the pressure in the chamber is much less than 1 mbar, the atoms of the vapour travel across the chamber in a straight line, without hitting any

gas molecules left in the vacuum chamber, until they strike a surface where they accumulate as a film (see Tab. 2.1). To help start and stop the deposition abruptly, mechanical shutters are used in front of the crucibles to control the deposited metal thickness.
To obtain large deposition rates, evaporators are often operated with high crucible temperatures. To obtain the best uniformity, the evaporation rate should be fairly low (1 Å/s in our case). Operation at such low rates requires extremely high vacuum to avoid contamination of the film. The deposition rate is commonly measured using a quartz crystal rate monitor. This device is a resonator plate that is allowed to oscillate at the resonance frequency, which is measured. The resonance frequency shifts due to the additional mass, as the material is deposited on top of the crystal. With an increase of its mass, the resonance frequency shifts by several percent. By linking the output of the frequency measurement system to the mechanical shutters, the thickness of the deposited layers can be well controlled over a wide range of deposition rates.
In our experiments we used two different evaporators to deposit the gold thin film: a Sistec evaporator and a Kurt J. Lesker (KJL) evaporator (shown in Fig. 2.12), both located in the clean room of the NEST Laboratory where this work was performed. In particular the KJL evaporator allows to heat the substrate prior (and/or during) the metal deposition.

Figura 2.12: Kurt J. Lesker Thermal evaporator.

2.8 Resistance measurements

In order to measure the extremely small resistance variation of our gold sensor (of the order of hundredths of Ω) during the hydrogenation process, we need a sensitive measurement setup. Firstly, we supply the sensing current and collect the voltage signal through a Lock-In Amplifier (LIA), which allows to detect and measure very small signals even when they are obscured by noise sources. Then, the resistance measurements are performed with a Wheatstone Bridge cascaded to a high quality PreAmplifier. In the following paragraphs these experimental methods are briefly explained.

2.8.1 Lock-In Amplifier

The operation principle of a Lock-In Amplifier is based on the Phase-Sensitive Detection technique, which permits to select the component of the signal at a specific reference frequency and phase. Noise signals at frequencies different from the reference one are rejected and do not affect the measurement.
Typically an experiment is modulated at a fixed frequency (from an oscillator or function generator) and the lock-in detects the response from the experiment at the reference frequency, as shown in Fig. 2.13, where the reference signal is a square wave with frequency ω_r.

The LIA used in our measurements generates its own sinusoidal wave (Lock-In reference in Fig. 2.13):

$$V_L sin(\omega_L t + \theta_{ref}) \tag{2.25}$$

whereas the response might be the signal waveform:

$$V_{sig} sin(\omega_r t + \theta_{sig}) \tag{2.26}$$

where V_{sig} is the signal amplitude. The Lock-In Amplifier amplifies the signal and then multiplies it by the lock-in reference using a phase-sensitive detector (PSD).

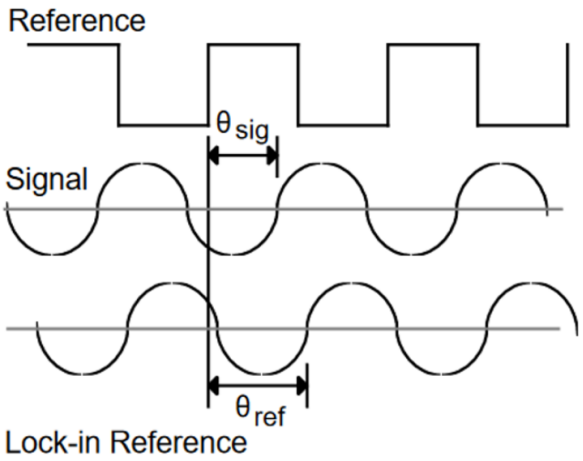

Figura 2.13: Diagram of the reference and output signals, and the Lock-In reference.

The output of the PSD is simply the product of two sinusoidal waves:

$$\begin{aligned} V_{PSD} &= V_L V_{sig} sin(\omega_L t + \theta_{ref}) sin(\omega_r t + \theta_{sig}) = \\ &= \frac{1}{2} V_L V_{sig} cos[(\omega_r - \omega_L)t + \theta_{sig} - \theta_{ref}] + \\ &+ \frac{1}{2} V_L V_{sig} cos[(\omega_r + \omega_L)t + \theta_{sig} + \theta_{ref}] \end{aligned} \tag{2.27}$$

The PSD output consists in two AC signals, one with the difference frequency $(\omega_r - \omega_L)$ and the other with the sum frequency $(\omega_r + \omega_L)$. If this signal passes through a low pass filter the AC signal with the sum frequency is removed and only if $\omega_r = \omega_L$ the difference component will be the DC signal:

$$V_{PSD} = \frac{1}{2} V_{sig} V_L cos^2(\theta_{sig} - \theta_{ref}) \tag{2.28}$$

This DC signal is proportional to the signal amplitude.
Let us suppose that the input is made up of signal plus noise. The PSD and low pass filter only detect signals whose frequencies are very close to the lock-in reference frequency. Noise signals at frequencies far from the reference are

attenuated at the PSD output by the low pass filter (neither $\omega_{noise} - \omega_{ref}$ nor $\omega_{noise} + \omega_{ref}$ are close to DC). Noise at frequencies very close to the reference frequency will result in very low frequency AC outputs from the PSD ($|\omega_{noise} - \omega_{ref}|$ is small). The noise attenuation depends on the low pass filter bandwidth. A narrower bandwidth will remove noise sources very close to the reference frequency, a wider bandwidth allows these signals to pass. Only the signal at the reference frequency and in phase with the reference signal will result in a true DC output and will not be affected by the low pass filter. This is the signal we want to measure.

2.8.2 Wheatstone Bridge

Following Ref. [1], the film resistance is measured with a volt-amperometric technique, using a Wheatstone Bridge (Fig. 2.14) cascaded to a low-noise voltage Pre-Amplifier (by Stanford Research Systems) with a gain factor set to 10 and very high quality filters. Since the frequency of our LIA output is set at 17 Hz, we can use the High Pass filter at 10 Hz (with a suppression of 6 dB) and the Low Pass filter at 30 Hz (with a suppression of 6 dB).
Usually the unknown resistance is fixed, so for balancing the bridge it is necessary to regulate the variable resistance, until the voltage output is zero and no current flows through the detecting instrument. In this condition, the unknown resistance equals the value assumed by the variable resistance. However, during a calorimetric experiment the sample resistance varies during the measurement because of the temperature increase of the sensor. For this reason, in order to work with the best sensitivity of LIA, we balance the bridge varying R_3 until the signal read by the LIA is as low as possible.

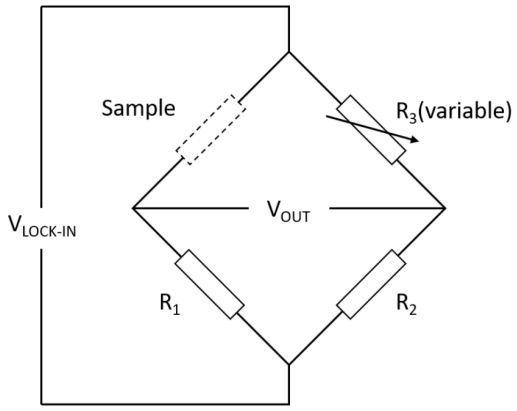

Figura 2.14: Scheme of the Wheatstone bridge set-up: $R_1 \approx R_2 \approx 1$ kΩ and $R_3 \approx R_{sample}$. $V_{LIA} = 0.200$ V.

The sample is mounted in the sample holder in a 2-wire set-up, and when the resistance is measured by using the same two contacts for both supplying current

and measuring the voltage difference, the contact resistance cannot be avoided.

Au thermometer on mica

3

3.1 Thermometer Fabrication

In this section we will explain the steps of the fabrication procedure which led to an improved thermometer.
It has been already stressed (section 1.3) that, by changing the Si substrate of the sensor with a mica foil, we can improve the thermometer sensitivity because the thermal conductivity of mica is about 300 times lower. Besides mica surfaces are classical templates for atomically smooth surfaces: it is therefore of interest to study evaporated thin films on mica with STM to see just how atomically smooth these thin films are [20,34]. Moreover it is known from literature that the annealing procedure can induce gold re-crystallization along the [111] direction [27,34], thus the scanning tunneling microscope capability can be exploited to analyse this feature, as well.
In order to properly compare the performance of our new setup with that one of the early sensor we decided to only replace the silicon support with a $\sim$250 μm-thick mica substrate and then to deposit a 5 nm film of titanium and a 20 nm layer of gold with a SISTEC evaporator (see section 2.7 for details), following the same procedure used in [1]. "M2 series" consists of the samples produced following the above procedure.

3.1.1 M2 series

The mica was cleaved in air with a standard scotch-tape technique prior to its introduction into the evaporator chamber. After the evaporation, the mica was cut into $\sim$5$\times$5 mm^2 squares with scissors, which resulted in 16 samples.

Generally, thermal annealing of metal films causes the grain boundaries to diffuse so that grains can merge to produce larger grains [33]. We have already seen in section 1.5 that flame annealing can remove moderate amounts of contaminants from the surface of gold films, as explained in Ref. [27]. So, right after the metal deposition, we annealed two samples of the M2 series with a small butane torch, heating them to the point where a faint reddish glow was visible. Our samples became almost immediately milky, presumably because our films are too thin to obtain the intended effect. So we decided to anneal the samples by performing safer heating ramps in an Ultra-High Vacuum (UHV) environment, inside the STM chamber, following the procedure described in [34].

The ramps were controlled via PC, using a specific LabVIEW software which allows to set the heating rate as a parameter. We explored a wide range of temperatures in order to grow thin films that are atomically flat and [111] oriented. In agreement with Ref. [34], surface reconstruction is achieved at temperatures ranging from 170 to 200°C. Furthermore, our thermometers should be able to tolerate a heating up to about 400°C during the TDS experiments. For these reasons, we studied several samples of the M2 series, which underwent heating ramps up to temperatures ranging from 100 °C to 400°C with an heating rate of 1 °C/minute.

M2-samples were mounted on the sample holder in order to perform experiments in the UHV chamber. We performed the first heating ramp up to 100 °C, with a rate of 1 °C/minute. We plotted the temperature data (measured with the thermocouple), recorded by the LabVIEW software, and we performed a linear fit in order to obtain the heating rate and check its correctness, as shown in Fig. 3.1, in the next page. From the slope we obtain the heating rate of the ramp: 1.2 °C. This control procedure has been repeated for all the heating ramps and for all the samples.

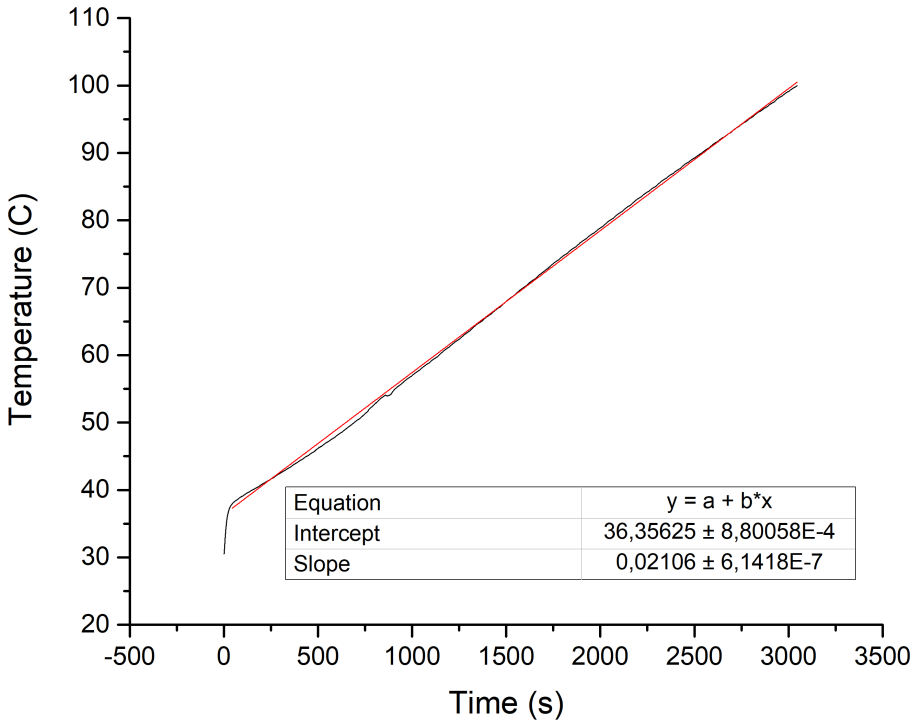

Figura 3.1: Linear fit of the heating ramp up to 100 °C performed on sample M2-5.

To complete the analysis of the samples we performed LEED measurements and took several STM images of different areas of the gold layer.
The LEED diffraction pattern, reported in Fig. 3.2, shows a broad, diffuse diffraction "half-moon", indicating a random orientation of the gold grains.
The STM images, shown in Fig. 3.3, are in good agreement with the LEED results. Stable and reproducible images were obtained by setting 1.3 V as bias voltage and 0.7-0.8 nA as set point current. We can see that, after the first heating ramp, the gold surface consists of rolling hills without many atomically flat regions and the few visible terraces are very narrow.

Therefore, from LEED and STM results, it is quite clear that a temperature of 100°C is not enough to obtain the surface re-crystallization.

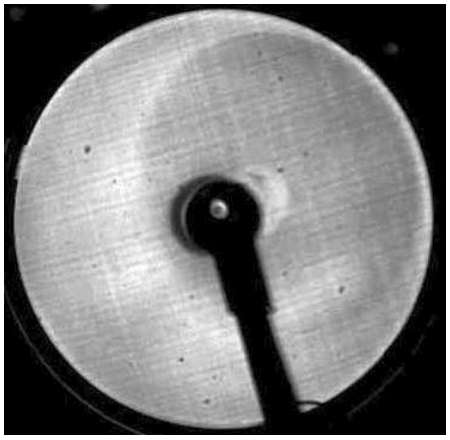

Figura 3.2: LEED diffraction pattern of sample M2-5 after the heating ramp up to 100°C. Electron energy 103.5 eV.

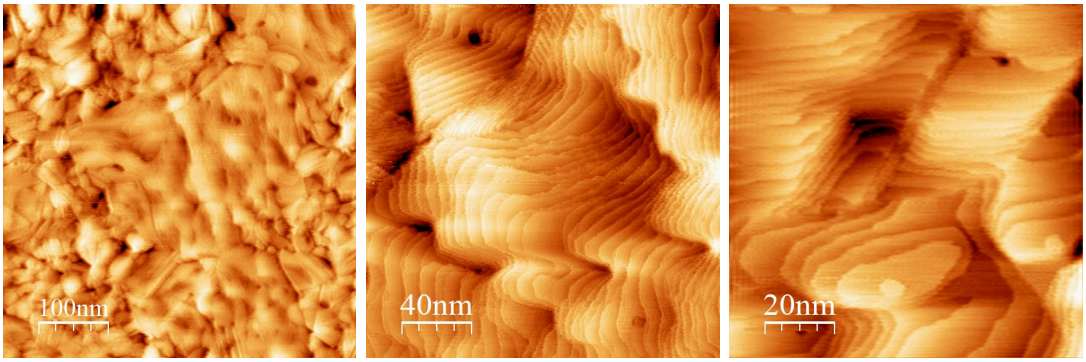

(a) (b) (c)

Figura 3.3: STM images of (a) 500×500 nm^2, (b) 200×200 nm^2, (c) 100×100 nm^2 of sample M2-5 after the heating ramp up to 100 °C.

Therefore, a heating ramp up to 150 ° has been performed, with a heating rate of 1°C/minute.
This time a weak hexagonal pattern can be recognized in the LEED pattern (Fig. 3.4), corresponding to the existence of a predominant in-plane orientation of the

gold film. However the elongated shape of the diffraction spots, with their blurry appearance, indicate that film areas with random in-plane orientation are still present on the surface.

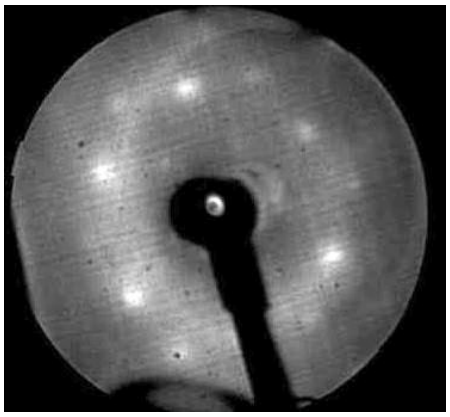

Figura 3.4: LEED diffraction pattern of sample M2-5 after the heating ramp up to 150°C. Electron energy 103.5 eV.

Coherently, the STM images illustrate a much smoother surface, with wider terraces, and the first signs of re-crystallization can be observed (Fig. 3.5). More in detail, Fig. 3.5(c) shows a rather irregular reconstruction pattern, which is visible especially on narrow terraces, indicating that the reconstruction layer is not well ordered [20].

Then, a heating ramp up to 200°C has been performed (1°C/minute).
The LEED diffraction pattern, reported in figure 3.6, displays the well-known [111] reconstruction pattern of the gold surface, with bright spots, typical of a clean and ordered surface [24].

The LEED diffraction pattern is in good agreement with the STM results. We can see that the topography of the clean and well-annealed Au(111) surface is characterized by large, atomically flat terraces, which often extend over many hundred angstroms (Fig. 3.7). The terraces exhibit the typical periodic pattern of pairwise-arranged, parallel lines, running in the $[11\bar{2}]$ direction (see section 1.4

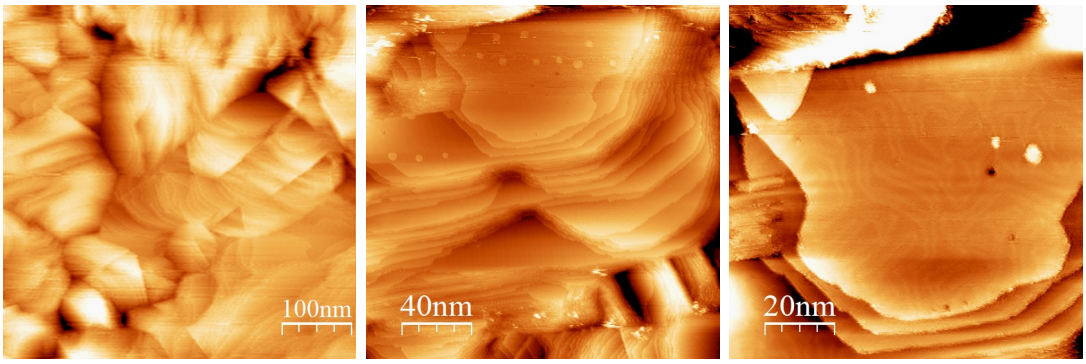

(a) (b) (c)

Figura 3.5: STM images of (a) 500×500 nm^2, (b) 200×200 nm^2 (c) 100×100 nm^2 of M2-5 after the heating ramp up to 150 °C.

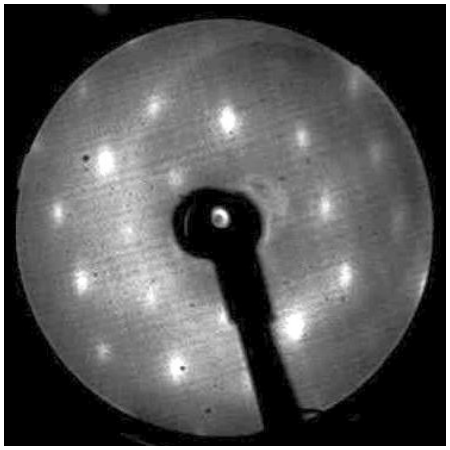

Figura 3.6: LEED diffraction pattern obtained on M2-12 after a heating ramp up to 200°C. Electron energy 103.5 eV.

for details), as can be seen in Fig. 3.7(c). The distance between neighbored pairs, in the $[1\bar{1}0]$ direction, has been measured, and amounts to 56 ± 7 Å, and the vertical corrugation amplitude, which is 0.18 ± 0.05 Å. The depression of the narrow regions between the two lines of each pair is less pronounced, 0.15 ± 0.05 Å. All these measured values are in good agreement with results from literature (see section 1.4). We know from literature that high-resolution STM images of the surface reveal an additional, more dense corrugation which is attributed to the atomic structure of the surface. Unfortunately, the resolution needed to observe this structure requires low temperatures because the imaging resolution is limited by the spatially large d orbitals of gold and thermal vibrations, so, at room temperature, we can only appreciate the pairwise-arranged corrugation lines associated with the reconstruction of the surface.

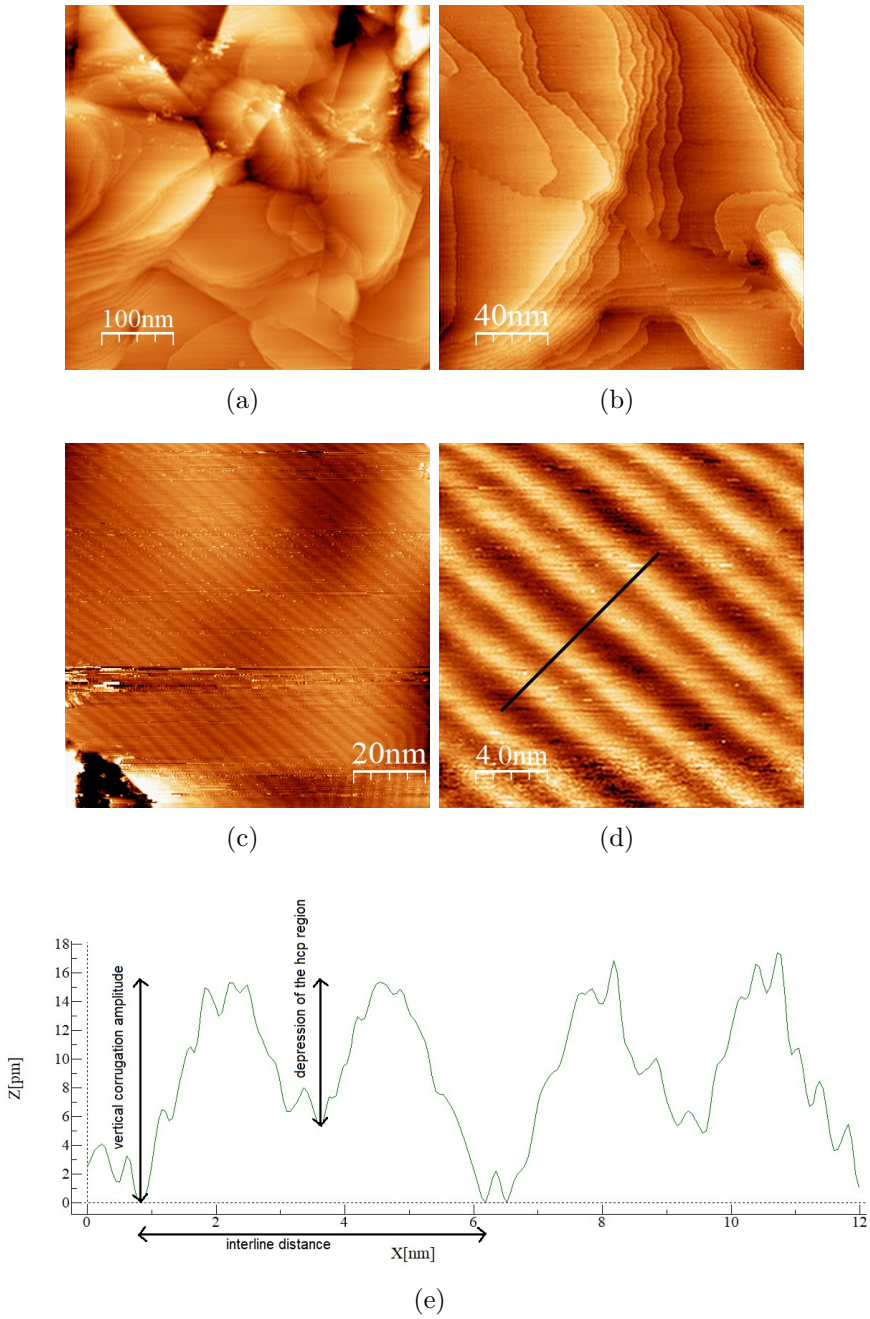

Figura 3.7: STM images of (a) 500×500 nm^2, (b) 200×200 nm^2, (c) 100×100 nm^2 and (d) 20×20 nm^2 of sample M2-12 after the heating ramp up to 200 °C. (e) Section view taken along the black line.

After the above measurements, a heating ramp up to 250°C has been performed, with a rate of 1°C/minute. As usual, the samples have been characterized by the use of STM and LEED.
The LEED pattern obtained after the heating ramp up to 250°C is illustrated in Fig. 3.8 and is quite similar to that obtained after the previous heating ramp.

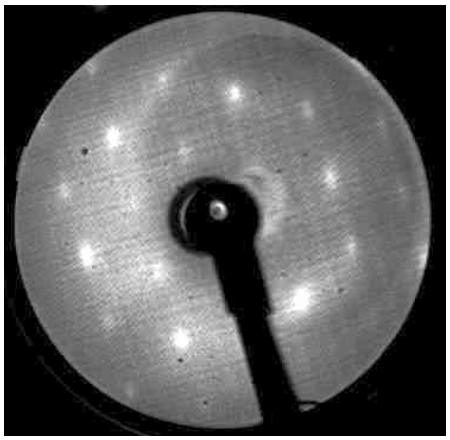

Figura 3.8: LEED diffraction pattern obtained on sample M2-12 after a heating ramp up to 250°C. Electron energy 103.5 eV.

As can be seen in the STM images reported in Fig. 3.9(a) and Fig. 3.9(b), the gold surface is flat and well reconstructed. Fig. 3.9(c) illustrates the impact of surface defects on the re-crystallization: the surface is distorted by the holes in the topmost Au layer. It may be speculated that these holes relate to the contraction of the topmost layer during the reconstruction process [20]. This defects cause a long-range modification in the re-crystallization pattern, indeed the parallel line pairs follow the perimeter of the holes. On the other hand Fig. 3.9(d) shows the behaviour of the corrugation lines where steps are present: the corrugation lines pass over the steps as explained in section 1.4.

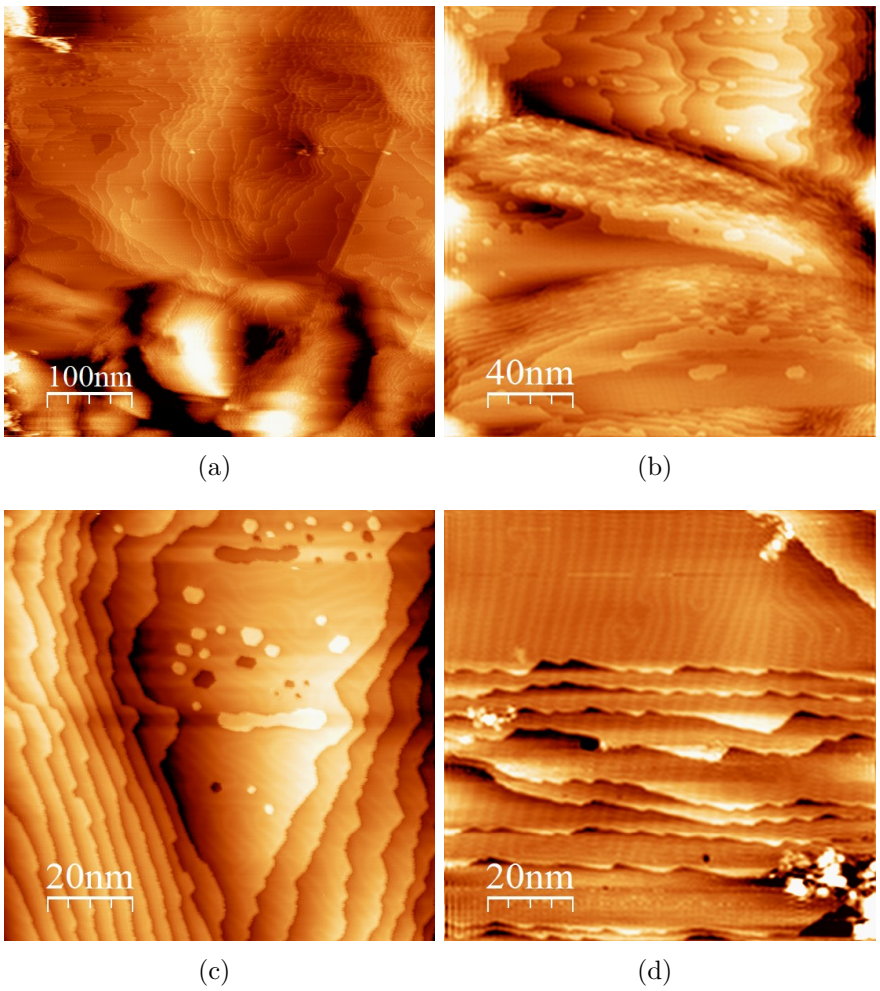

Figura 3.9: STM images of (a) 500×500 nm^2, (b) 200×200 nm^2,(c) and (d) 100×100 nm^2 of M2-12 after the heating ramp up to 250 °C.

Subsequently, a heating ramp up to 300°C (1 °C/minute) has been performed in order to investigate the evolution of the reconstruction pattern with temperature. The LEED diffraction pattern is quite different from the previous ones: the spots are less bright, and the appearance of a diffraction ring indicates the contextual presence of a random orientation of gold grains (Fig. 3.10).

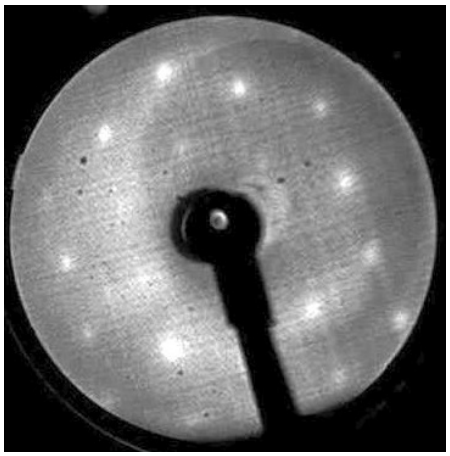

Figura 3.10: LEED diffraction pattern of M2-12 after a heating ramp up to 300°C. Electron energy 103.5 eV.

The STM images reported in Fig. 3.11 reveal a peculiar dendritic structure which emerges on the gold surface and partially covers the Au(111) pattern. Obviously this apparently inexplicable behaviour is quite troubling because this strange structure prevents us from studying the film surface.

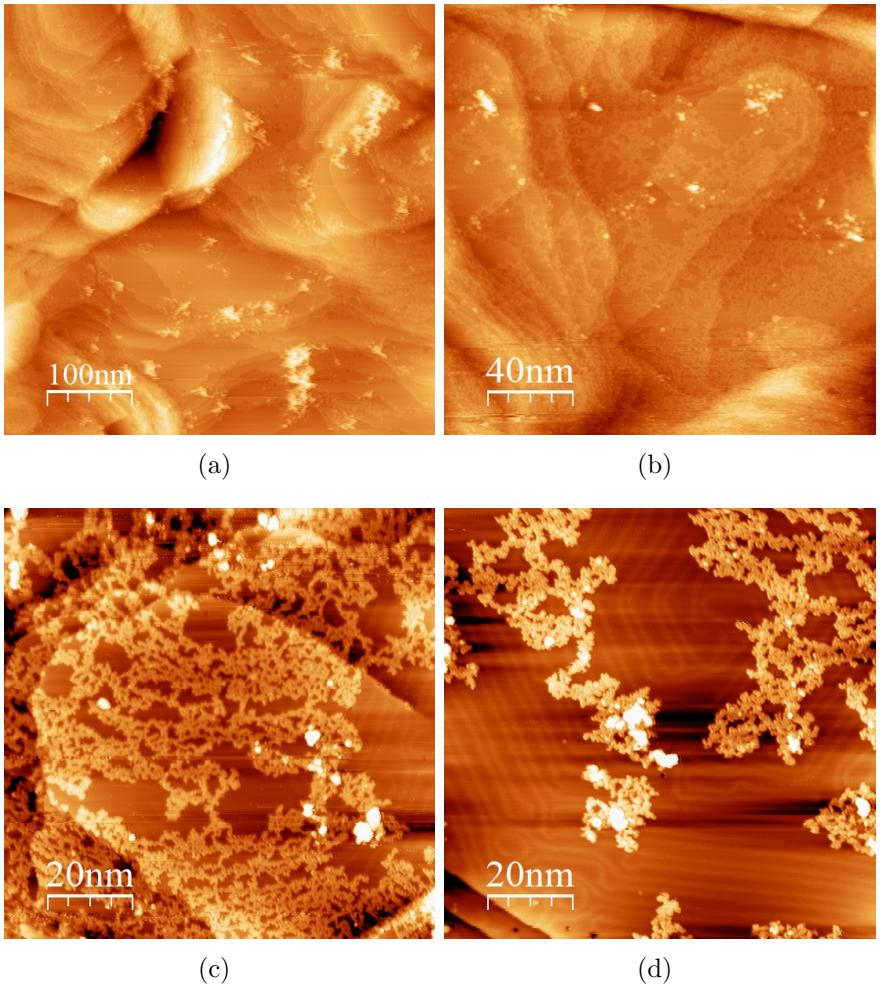

Figura 3.11: STM images of (a)500×500 nm^2, (b) 200×200 nm^2, (c), (d) 100×100 nm^2 of M2-12 after the heating ramp up to 300 °C.

In order to understand the phenomenon shown above, a last heating ramp up to 400°C has been carried out, this time with a rate of 1°C/second (the same rate we will use for the TDS experiments). Finally the samples have been studied by using LEED and STM.
The LEED diffraction pattern, illustrated in Fig. 3.12, is similar to that obtained after the previous heating ramp.

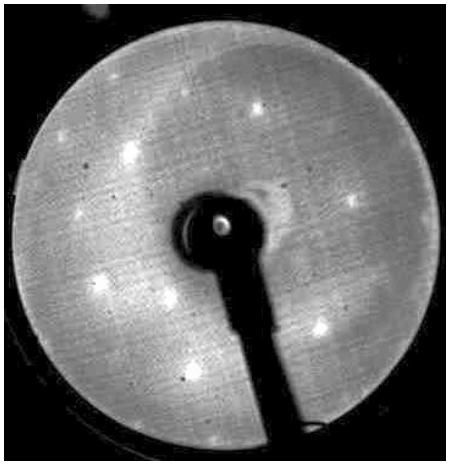

Figura 3.12: LEED diffraction pattern of M2-12 after a heating ramp up to 400°C. Electron energy 103.5 eV.

From the STM images we can see that the dendritic framework is even more prominent, but the corrugation lines are still present, as can be seen in Fig. 3.13. Now it is of primary interest to understand the peculiar behaviour of the sample after the annealing ramp up to 300°C in order to adjust our working procedure thus preventing the appearance of the dendritic structure.
Our first guess has been titanium diffusion in the gold thin film induced by the temperature increase. Indeed, thin films are exposed to the risk of undergoing severe interdiffusion phenomena. Titanium/gold pads are largely utilized in electronic devices, so such a behaviour has been already studied. Diffusion phenomena in titanium/gold thin films occurring at temperatures ranging between 200 and

400°C have been investigated in Ref. [51], whose research work will be explained in appendix A. It is right to point out that the results reported in Ref. [51] were obtained with much thicker films and after annealing in air; however the great impact of their outcome suggests that our observations could have been induced by a similar behavior.

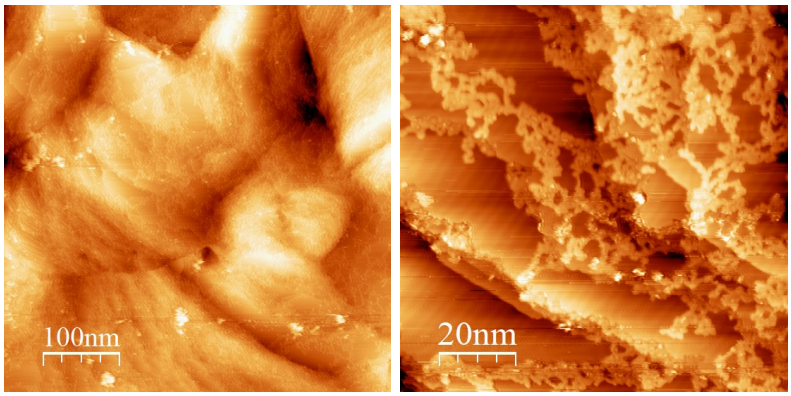

(a) (b)

Figura 3.13: (a) STM images of 500×500 nm^2 of the Au film after the heating ramp up to 400 °C. (b) STM images of 100×100 nm^2 of M2-12 after the heating ramp up to 400 °C.

So a new series of samples has been prepared, "M3", without using titanium as adhesion promoter between mica and gold.

3.1.2 M3 series

In order to prepare the new series of samples, the mica was cleaved in air by using adhesive tape just before its introduction in the evaporator chamber, where a 20 nm-thick film of gold was deposited. After the evaporation, the mica was cut into ∼5×5 mm^2 squares with scissors, obtaining 16 samples. Several samples of this series have been loaded in the UHV chamber in order to study their behaviour after several annealing ramps, with temperatures ranging from 150 to 450°C.
Firstly the sample was subjected to a heating ramp up to 150°C with a rate of

1°C/minute, then LEED and STM measurements have been performed.
The LEED diffraction pattern, shown in Fig. 3.14(a) and 3.14(b), is comparable to that obtained for the previous series of samples (see Fig. 3.4) after the same annealing ramp. A weak hexagonal pattern can be distinguished but the overlapped ring-like structure indicates that the reconstruction process is not completed yet. Two diffraction patterns, corresponding to different electron energies, are reported, because this time the energy of 103.5 eV was not enough to appreciate the LEED pattern. So we performed another measurement, with an electron energy of 120.4 eV.
The STM images are quite noisy and reveal a surface characterized by small terraces (Fig. 3.14(c)). Besides it looks like the reconstruction process has already started: indeed in Fig. 3.14(d) the corrugation lines are clearly visible, even if the signal is noisy.

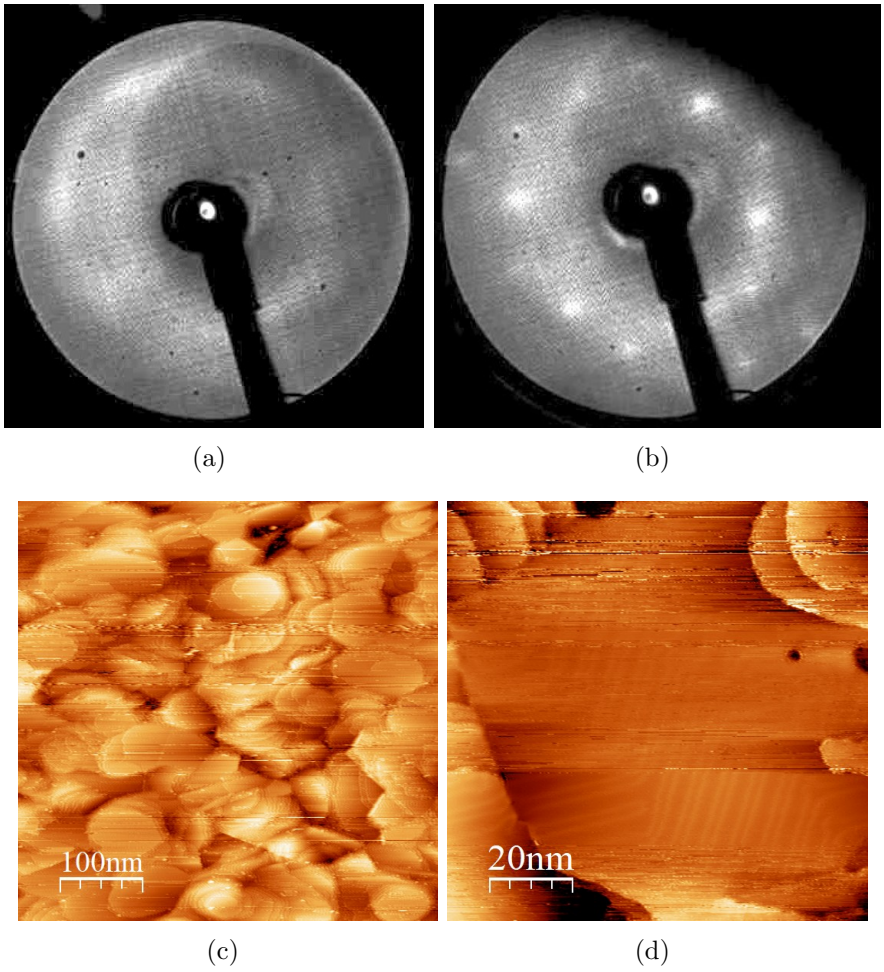

Figura 3.14: LEED diffraction pattern of sample M3-9 after the heating ramp up to 150°C. (a) Electron energy 103.5 eV. (b) Electron energy 120.4 eV.
STM images of (c) 500×500 nm^2 and (d) 100×100 nm^2 of sample M3-9 after the heating ramp up to 150 °C.

Fig. 3.15 shows the LEED pattern after a further heating ramp, up to 200°C. The diffraction spots are getting weaker while the ring-like diffraction pattern is increasingly evident.
From the STM images we can see the dendritic structure which arises on the surface, and this time it is already visible in the larger scan area, as shown in Fig. 3.15(c).

After having annealed the sample up to 250°C the situation has worsened: the LEED image is not so different from the one recorded after the previous annealing, but the dendritic network covers the greater part of the gold surface, as shown in the STM images.

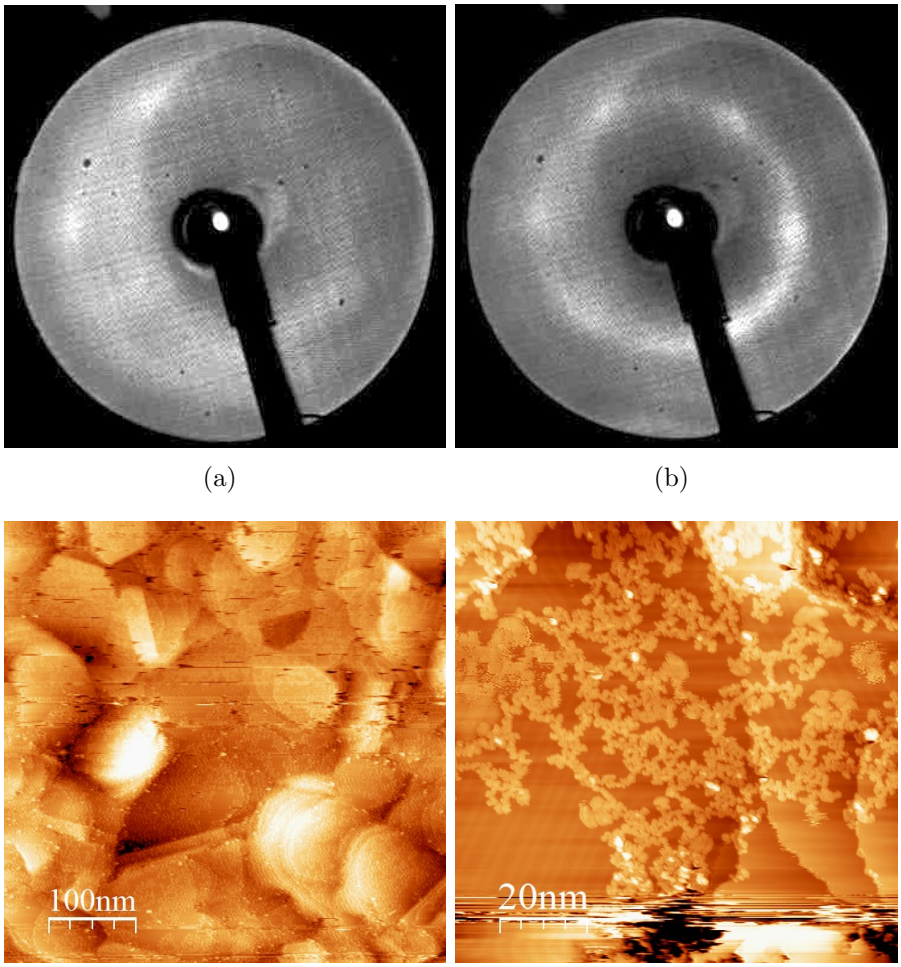

Figura 3.15: LEED diffraction pattern of sample M3-9 after the heating ramp up to 200°C. (a) Electron energy 103.5 eV. (b) Electron energy 120.6 eV.
STM images of (c) 500×500 nm^2 and (d) 100×100 nm^2 of sample M3-9 after the heating ramp up to 200 °C.

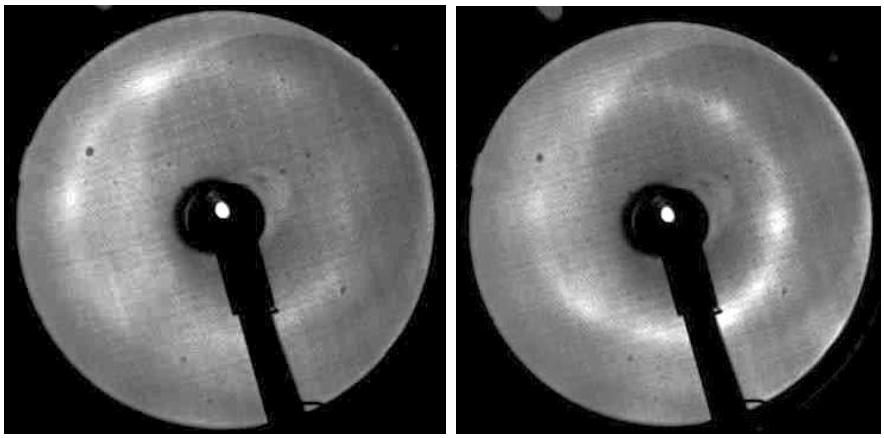

(a) (b)

Figura 3.16: LEED diffraction pattern of sample M3-9 after the heating ramp up to 250°C. (a) Electron energy 103.5 eV. (b) Electron energy 199.9 eV.

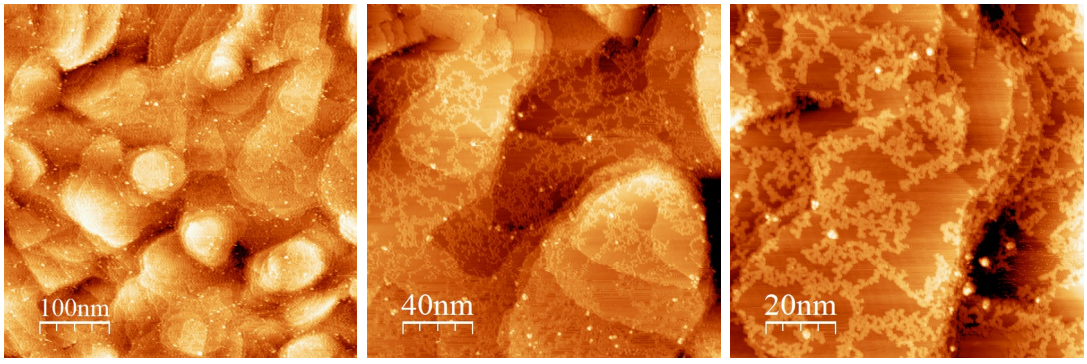

(a) (b) (c)

Figura 3.17: (a) STM images of 500×500 nm^2, (b) 200×200 nm^2 and (c) 100×100 nm^2 of M3-9 after the heating ramp up to 250 °C.

So a further heating ramp, up to 350°C, has been performed. Some diffraction spots are still visible in the LEED diffraction pattern, as shown in Fig. 3.18(a), and even if the dendritic formation covers almost entirely the surface of the sample, some areas still present the corrugation lines which characterize the [111] reconstruction (Fig. 3.18(c)).

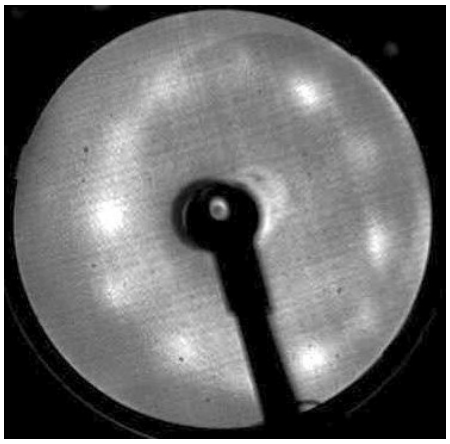

(a)

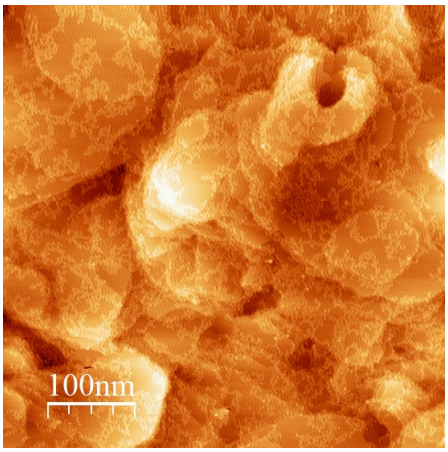

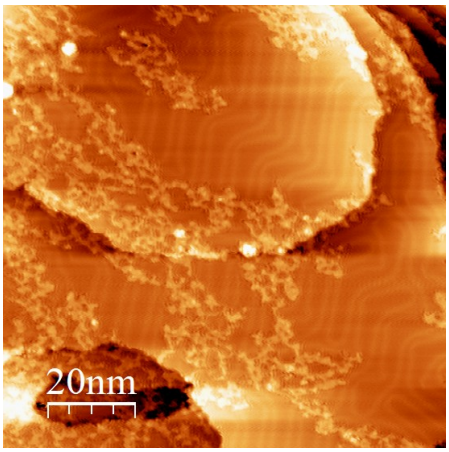

(b) (c)

Figura 3.18: (a) LEED diffraction pattern of sample M3-9 after the heating ramp up to 350°C. Electron energy 103.5 eV. STM images of (b) 500×500 nm^2 and (c) 100×100 nm^2 of M3-9 after the heating ramp up to 350 °C.

Finally, M3-9 was subjected to the last annealing ramp up to 450°C. At this point the dendritic conformation has completely covered the gold surface and the Au[111] reconstruction is no more visible, as illustrated in Fig. 3.19. Moreover the LEED analysis reveals a diffraction pattern which can be attributed to the mica substrate [52]. Indeed, the measured distance between the diffraction spots is different from that measured for the Au(111) diffraction pattern relating to the M2-samples.

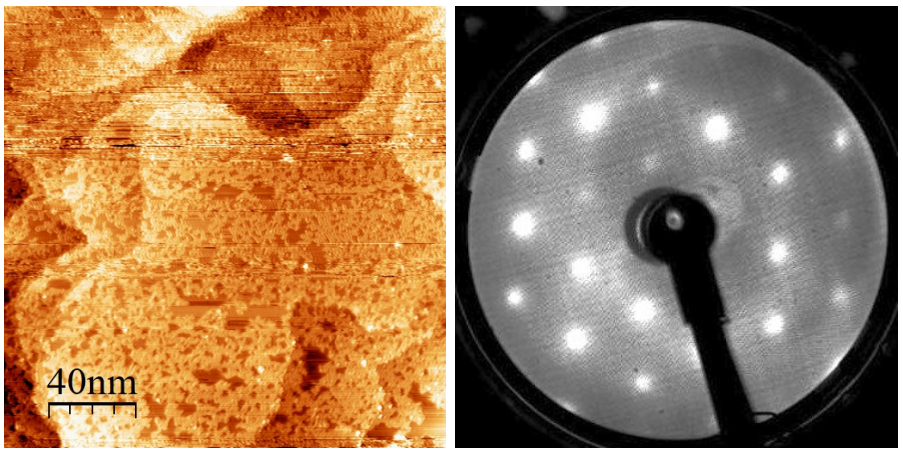

(a) (b)

Figura 3.19: (a) STM image of 200×200 nm^2 of the Au film after the heating ramp up to 450 °C. (b) LEED diffraction pattern of sample M3-9 after the heating ramp up to 450°C. Electron energy 103.5 eV.

So, besides the issue of the dendritic structure, it seems likely that the agglomeration of the gold film has occurred, as described in [53]. In order to confirm our hypothesis, the M3-samples have been examined under an optical microscope. The resulting images are reported in Fig. 3.20.

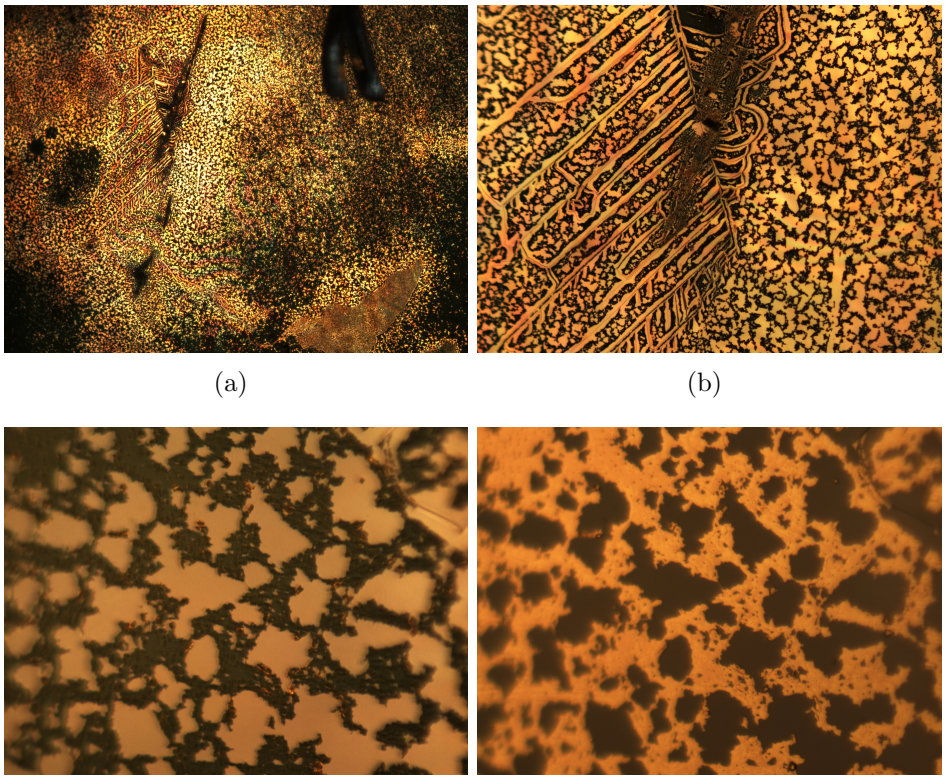

(a) (b)

(c) (d)

Figura 3.20: (a) Optical microscope images of M3-9 after its annealing up to 450°C with 5X magnification and dark-field illumination, (b) 20X magnification and dark-field illumination, (c) 50X magnification and dark-field illumination, (d) 50X magnification and bright-field illumination.

The process of island formation in thin gold films after annealing at high temperatures is well known: the agglomeration process consists of three stages, hole formation, hole enlargement and separation into islands [53]. This process is well discernible in Fig. 3.20(d). Gold islands are clearly visible in the images above, so it is not surprising that the LEED diffraction pattern reveals the mica substrate below the gold thin film.
After the careful analysis of M3-samples it is safe to say that the dendritic fra-

mework observed with M2-samples was not due to the interdiffusion between titanium and gold. Therefore, another explanation needs to be developed in order to account for this unexpected phenomenon. After a careful study of relevant literature, has been considered the water intercalated between the gold and the mica, as extensively explained in appendix B.
All surfaces exposed to ambient conditions are covered by a thin film of water. Except at high humidity conditions, namely relative humidity (RH) higher than 80%, those water films have nanoscale thickness. Nevertheless, even the thinnest film can profoundly affect the physical and chemical properties of the substrate. In Ref. [54,55] Scanning Polarization Force Microscopy (SPFM) was used to study water films on a mica surface. While in Ref. [56] the graphene template technique has been used to visualize and measure water adlayers on mica under ambient conditions. In the light of the results reported in these research works, the STM images relating to M3-samples have been analysed and the dendritic structure height has been measured, with a value in agreement with many works. However, the reliability of thickness measurements, as extensively explained in appendix B, is not so high. Moreover no evidence of water adlayers between mica and the gold film deposited on it has been reported so far. Even though it has not been possible yet to confirm this conjecture, it is sure that the water which quickly covers the mica surface after its cleavage is generally removed by heating in vacuum. And those (rare) authors who use titanium as adhesion promoter deposited much thicker metal films.
So, in order to prove that water is the disruptive factor, a new series of samples has been prepared by the use of another evaporator, which allows to anneal the sample in the evaporation chamber before the deposition.

3.1.3 M4 series

It is well known that the preparation of high quality thin films dependents upon the precise control of temperature, pressure, growth rate, cleanliness and thickness. The essential requirements for the production of gold thin films are the employment of the best possible vacuum, a clean chamber , a smooth dry substrate, and an appropriate combination of substrate temperature and deposition rate [27]. In order to obtain a high quality gold film, the water adsorbed on the

mica surface immediately after its cleavage has been desorbed in the evaporation chamber by a sample annealing at 200°C overnight. The Au deposition rate and the sample temperature are strongly linked, and conditions must be controlled to favor two-dimensional growth to produce large flat grains of [111] oriented gold [33]. A deposition rate of 1 Å/s has been chosen, and the gold film has been deposited at 200°C, at a pressure of 4×10^{-6} mbar. Once the deposition was completed, a temperature of 200°C was kept in the chamber for half an hour, following Ref. [35]. After the venting of the chamber the sample was cut in 16 pieces with scissors. Then a detailed study of the thermal annealing of these new samples has been performed, in order to provide additional energy for surface atoms and clusters to react and diffuse, and for the surface to relax and re-crystallize.
Before studying M4-samples with STM and LEED, they have been subjected to an overnight annealing at about 120°C in order to degas the samples.
After this step, the LEED pattern corresponds to an already re-crystallized surface, as shown in Fig. 3.21(a). While the STM images are quite noisy, even if the terraces look rather wide, as can be seen in Fig. 3.21(b).

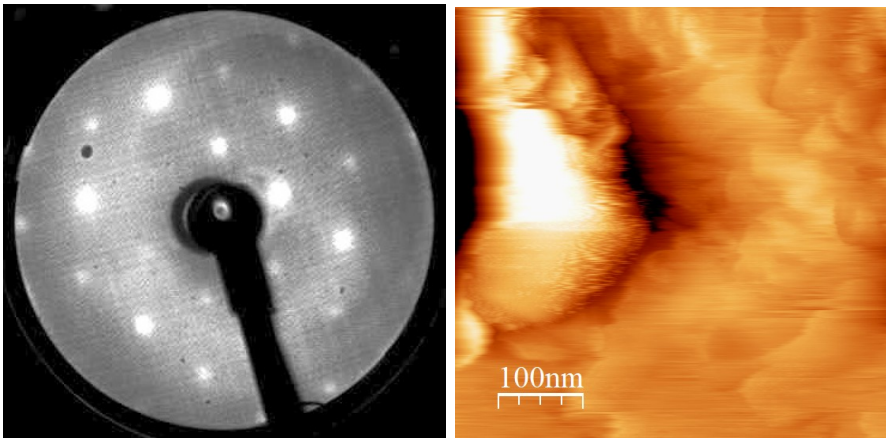

(a) (b)

Figura 3.21: (a) LEED diffraction pattern of sample M4-8 after the degassing at about 120 °C. Electron energy 103.5 eV. (b) STM images of 500×500 nm^2 of sample M4-8 after the degassing at about 120 °C.

In order to get a better reconstruction and a better resolution for the STM images, an annealing ramp up to 200°C has been performed, with the usual rate of 1°C/minute.
The diffraction spots in the LEED pattern obtained after this ramp are brighter and more focused, indicating a progress in the surface reconstruction (Fig. 3.22). The STM images continue to be quite noisy, but show a surface characterized by very flat terraces. Besides the first corrugation lines become visible (Fig. 3.23(b)).

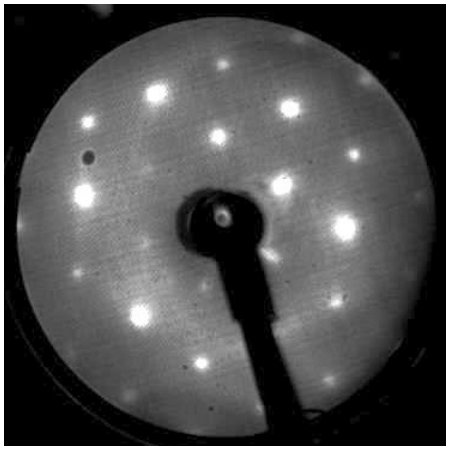

Figura 3.22: LEED diffraction pattern of M4-8 after the annealing ramp up to 200°C. Electron energy 103.5 eV.

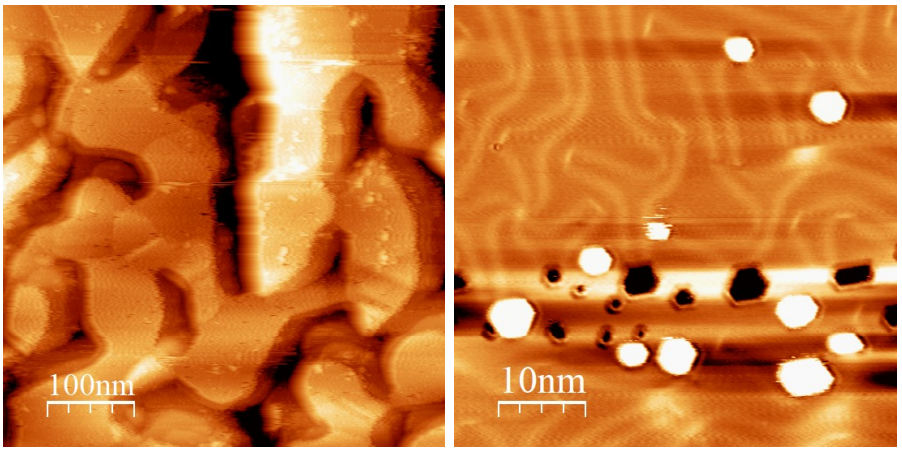

(a) (b)

Figura 3.23: (a) STM images of 500×500 nm^2 and (b) 50×50 nm^2 of M4-8 after the heating ramp up to 200 °C.

Then the samples have been subjected to a further heating ramp, up to 300°C.

So their surfaces have been studied by the use of LEED and STM.
The LEED diffraction spots continue to be bright and well focused (see Fig. 3.24). The terraces keep getting bigger and bigger but a good resolution is impossible to achieve due to the noise and the apparent dirt on the sample surface (Fig. 3.25).

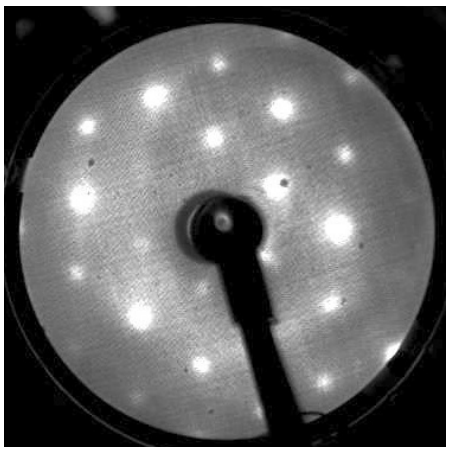

Figura 3.24: LEED diffraction pattern of sample M4-8 after the annealing ramp up to 300°C. Electron energy 103.4 eV.

Finally, a last annealing ramp has been performed, up to 400°C, with a rate of 1°C/second. However, before analysing the samples with STM, we realized that they have been damaged by the ramp because their surfaces look milky. Therefore M4-samples have been observed with the optical microscope which confirmed that the agglomeration process had taken place.

In view of the above, it seems that the "water issue" has been solved, because dendritic structures were no longer observed. However, the deposition procedure needs to be improved, because, even if the gold terraces are larger, the surface presents some detachments producing noisy images.
We speculate that the problem is due to the different thermal expansion coefficients of gold and mica which produces stresses on the gold surface.
Indeed, in very thin films, internal mechanical strain is an important parameter.

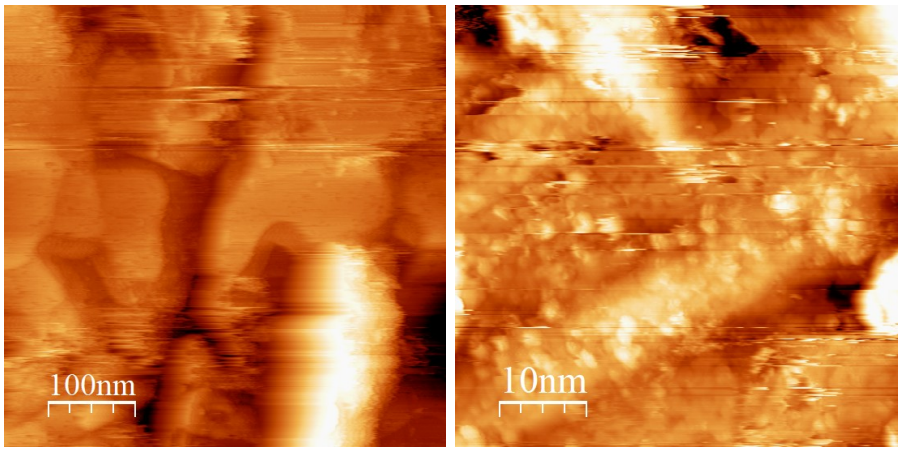

(a) (b)

Figura 3.25: STM images of (a) 500×500 nm^2 and (b) 50×50 nm^2 of sample M4-8 after the heating ramp up to 300 °C.

This characteristic can be the leading cause of deformation in the film-substrate system and, in this respect, the thermal expansion coefficients of the film and the substrate play a major role. In this context, changes in temperatures are particularly insidious, because they can cause the adhesion loss and detachments. It can be found that typical thermal expansion coefficients, perpendicular to the cleavage plane, for muscovite mica are in the range $\alpha_{\perp}$=13-17×10^{-6} °C^{-1} in the temperature range 20-300 °C, and 16-24×10^{-6} ° C^{-1} over 300-600 °C. Parallel to the cleavage plane, values of $\alpha_{\parallel}$=8.0-12×10^{-6} °C^{-1} are reported, in the same temperature range, with the coefficient increasing wth temperature [57]. On the other hand, the thermal expansion coefficient for a 10-nm thick Au film is 5 to 6 times higher than its corresponding bulk value of $14.2 \times 10^{-6} °C^{-1}$, and its value increases with increasing deposition rate [58]. It is evident that the two thermal expansion coefficients differ by almost one order of magnitude. So when the sample (Au+mica) cools off after the deposition procedure (at about 200°C) the Au film shrinks much more than its substrate. Therefore, possible micro-detachments associated with this behaviour could have caused the noise which has affected the STM measurements.

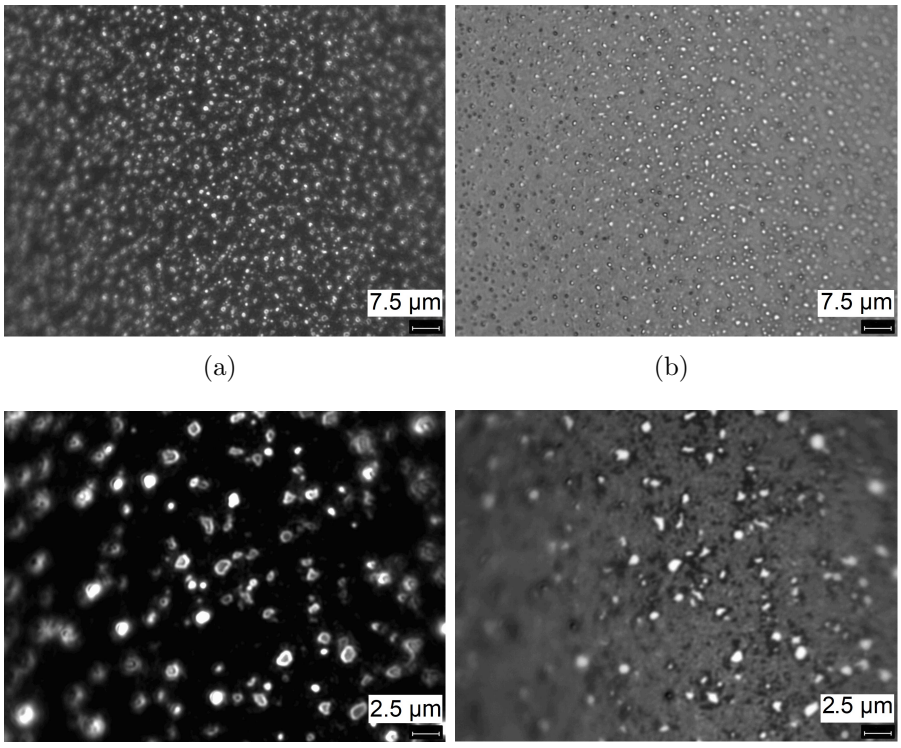

Figura 3.26: (a) Optical microscope images of sample M4-8 after its annealing up to 400°C with 50X magnification and dark-field illumination, (b) 50X magnification and bright-field illumination, (c) 150X magnification and dark-field illumination, (d) 150X magnification and bright-field illumination.

3.1.4 M5 series

In order to prevent the possible detachment of the gold film from the mica substrate, the M5 series of samples has been produced following a different procedure. To reduce the thermal stress due to their different thermal expansion coefficients, the metal film has been deposited once the substrate was completely cooled (after an overnight annealing at 200°C). Then, as usual, the sample was cut into the 16 pieces which constitute the M5 series.
Before analysing the M5-samples through STM and LEED, they were degassed at about 140°C in the UHV chamber. As shown in Fig. 3.27 the terraces extension reaches 100 nm and the corrugation lines typical of the [111] gold reconstruction are already visible, but not everywhere. The LEED diffraction pattern is consistent with these images: it illustrates bright spots within a high contrast background, typical for a well ordered surface.

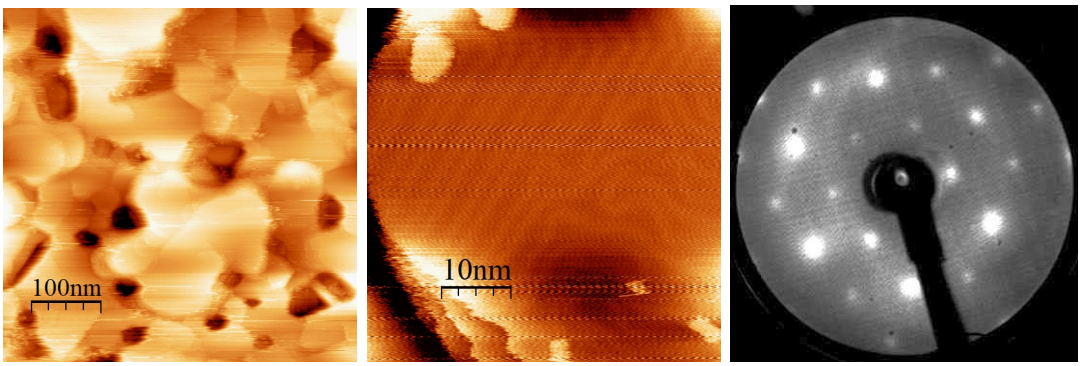

(a) (b) (c)

Figura 3.27: STM images of (a) 500×500 nm^2 and (b) 50×50 nm^2 of M5-1 after the degassing at about 140°C. (c) LEED diffraction pattern of M5-1 after the degassing at about 140°C. Electron energy 103.5 eV.

In order to get a better reconstruction, the samples have been annealed up to 200°C, with the usual rate of 1°C/minute.
The LEED analysis reveals bright spots arranged in the hexagonal pattern which characterizes the [111] gold surface (see Fig: 3.28).

The terraces obtained after this heating ramp have a width of up to 300 nm, and exhibit the well-known periodic pattern of pairwise-arranged lines which characterize the [111] gold reconstruction (Fig. 3.29). Moreover the U-shaped connections between neighbouring corrugation lines are clearly visible. At last, the three different rotational domains which characterize the herringbone reconstruction can be observed. As seen in section 1.4, the corrugation line pairs are characteristically deformed in the vicinity of the bending points.

We know from literature that on clean and fully relaxed Au(111), one typically finds large regions where the pairwise-arranged parallel lines form a herringbone pattern with remarkable long range order. However, the structure of the surface of an Au thin film can be changed by bending the mica substrate to which the film is attached, as explained in Ref. [59, 60]. Therefore, the fact that we often do not observe the elbows typical of the herringbone pattern, could be explained in

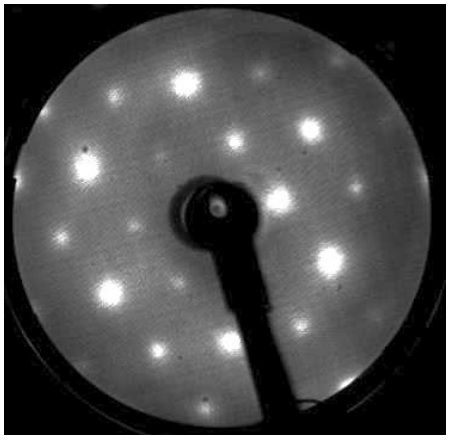

Figura 3.28: LEED diffraction pattern of M5-1 after the heating ramp up to 200°C. Electron energy 103.5 eV.

terms of the compressive strain on the mica substrate, exerted by the washers in the sample holder.
Finally, in order to characterize the evolution of the reconstruction process on these new samples, a heating ramp up to 300°C with a rate of 1°C/minute has been performed. However it has not been possible to characterize the samples by the use of STM and LEED because the surface became milky after reaching 300°C, as can be seen in Fig. 3.30.

It is worth recalling that we have to do with a very thin film, and the thermal stress induced by the heating ramp can damage the samples evidently. In principle this fact is not a problem, because the annealing ramp up to 200°C ensures a perfect reconstruction on the gold surface with flat and wide terraces. However, it should be kept in mind that a measurement which involves the heating of the sample up to higher temperatures, as the Thermal Desorption Spectroscopy (TDS), is completely destructive. Nevertheless, the M5 series confirmed the absence of dendritic structures, supporting the hypothesis that the water issue has been solved.
In summary, the surface reconstruction obtained with the M5 samples after the

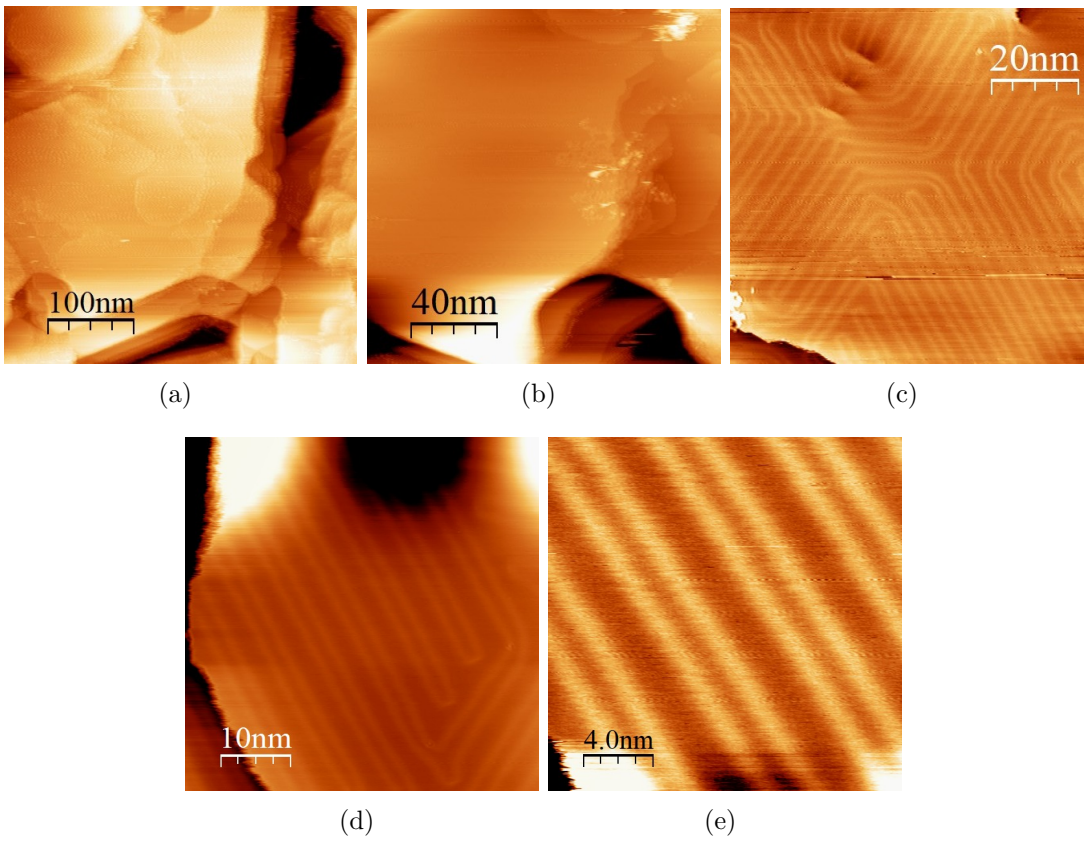

Figura 3.29: STM images of (a) 400×400 nm^2, (b) 160×160 nm^2, (c) 80×80 nm^2, (d) 50×50 nm^2 and (e) 20×20 nm^2 of sample M5-1 after the heating ramp up to 200°C.

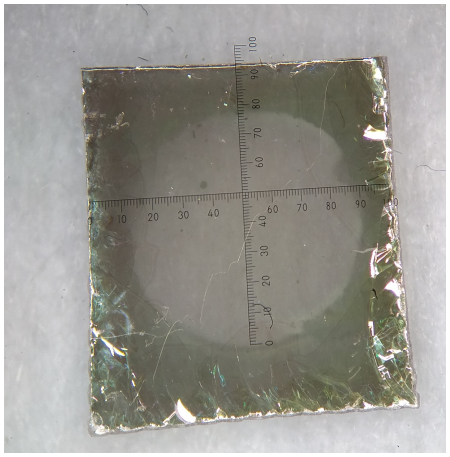

Figura 3.30: Optical microscope image of sample M5-1 after the annealing ramp up to 300°C. The microscope ruler is visible.

annealing ramp up to 200°C performed with a heating rate of 1°C/minute is the best obtained. In order to have enough samples to characterize the sensor another series has been prepared, M6, following a procedure identical to that used to prepare the M5 series. So the next step is the thermometer calibration.

3.2 Thermometer Calibration

Before using the sensor as a thermometer, we need to know its thermal and electrical properties by performing a proper calibration. As a result of the calibration, the temperature coefficient and the electrical resistivity of the gold thermometer can be obtained, in order to compare them with the standard ones listed in literature.

3.2.1 Resistance vs Temperature

In order to calibrate the thermometer, the samples M5-4 and M6-2 have been subjected to several annealing ramps.

Sample M5-4

After the overnight degassing of the sample at about 140°C and its annealing up to 200°C, STM and LEED measurements have been performed in order to verify that the surface appearance was comparable to that of the other M5 samples after the same procedure. Then, two calibration ramps were recorded with the Wheatstone Bridge set-up described in section 2.8. Taking into account the maximum temperature rating to avoid sample damage, it is possible to perform the calibration measurement with the Wheatstone Bridge by doing 2 slow ramps up to about 100°C. The ramp profile has been set as follows: 2100 s of heating, 2100 s of cooling and 1800 s of pause at the end, before the next ramp. The last pause period is applied in order to slowly cool down the sample and allowing possible mechanical adjustments of the contacts. During the heating ramp we record the temperature of the gold sensor measured by the thermocouple, the current and the voltage supplied to heat the sample and the sample resistance. The ramps are controlled via LabView, and the data are recorded with a time interval of 1 s and a time constant of integration of the lock-in amplifier of 1 s. So it is possible to plot the resistance vs the temperature.

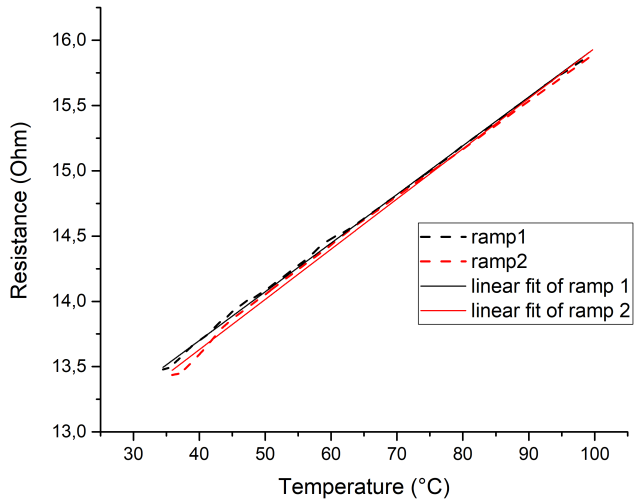

Figura 3.31: Data and linear fit of the calibration ramps.

As shown in Fig. 3.31 there is the expected linear proportionality, therefore we can perform a linear fit of the data using the relation:

$$R(T) = R_0[1 + \alpha(T - T_0)] \tag{3.1}$$

The parameters obtained for M5-4 are listed in Table 3.1. The average values are the results of the weighted average and the errors are the standard deviations.

Ramp	**Slope** $(R_0 \cdot \alpha)$ $\Omega{\cdot}^{\circ}\mathrm{C}^{-1}$	**Error**	**Intercept** (R_0) Ω	**Error**	**Adjusted** R^2
1	0.03730	$2{\cdot}10^{-5}$	12.208	0.001	0.999
2	0.03847	$4{\cdot}10^{-5}$	12.092	0.003	0.998
average	0.03808	$8{\cdot}10^{-4}$	12.12	0.08	

Tabella 3.1: Parameters of the linear fit and the weighted average.

The slopes obtained from the fit correspond to the product $R_0 \cdot \alpha$ and the intercepts correspond to R_0; T_0, the reference temperature, is the temperature measured by the thermocouple just before the start of the calibration ramp.
From the average parameters we can obtain the average temperature coefficient of resistance for M5-4:

$$\alpha_{M5-4} = (3.1 \pm 0.3) \cdot 10^{-3}\,^{\circ}\mathrm{C}^{-1} \tag{3.2}$$

Another important parameter for calibrating and comparing samples is the electrical resistivity, which is defined as:

$$\rho = \frac{A}{l} \cdot R$$

where R is the resistance of the sample, A is the cross-sectional area of the conductor and l is its length. The average section can be obtained from the ratio between the volume of the gold layer and its diagonal length d, and the same diagonal length can be used as l (we are neglecting the area occupied by the electrical contacts):

$$\rho = \frac{V/d}{d} \cdot R_0 \tag{3.3}$$

Measuring the dimensions of the sample:

$$a = 7.00 \pm 0.01\,\text{mm} \quad b = 6.35 \pm 0.01\,\text{mm}$$

and knowing the thickness of the metal film:

$$thickness = (20 \pm 1)\,\text{nm}$$

the volume and the diagonal length can be calculated in order to obtain the electrical resistivity:

$$\rho_{M5-4} = (12.0 \pm 0.7) \cdot 10^{-8}\,\Omega \cdot \text{m} \tag{3.4}$$

In order to study the repeatability of this calibration the above operations have been performed for another sample belonging to the M6-series.

Sample M6-2

After the overnight degassing of the sample and its annealing up to 200°C, its surface has been analysed by STM and LEED. So 5 calibration measurements have been performed with the usual Wheatstone Bridge set-up by doing 5 ramps up to about 100°C. After plotting the data and performing the linear fit we obtained the average coefficient listed in Table 3.2.
The average temperature coefficient obtained from the fit is:

$$\alpha_{M6-2} = (2.8 \pm 0.1) \cdot 10^{-3}\,^{\circ}\text{C}^{-1} \tag{3.5}$$

In order to obtain the electrical resistivity we measure the dimensions of the second sample:

$$a = 6.90 \pm 0.01\,\text{mm} \quad b = 6.60 \pm 0.01\,\text{mm}$$

and we obtain (for the usual thickness of (20±1) nm):

$$\rho_{M6-2} = (14.7 \pm 0.8) \cdot 10^{-8}\,\Omega \cdot \text{m} \tag{3.6}$$

Comparing the average values of α for M5-4 and M6-2 we see that they correspond within the error range. Moreover, this result is in good agreement with the bulk value of $\alpha = 3.4 \cdot 10^{-3}\,^{\circ}\text{C}^{-1}$ [9]. As for the electrical resistivity, our results turn out to be one order of magnitude higher than those listed in literature for bulk

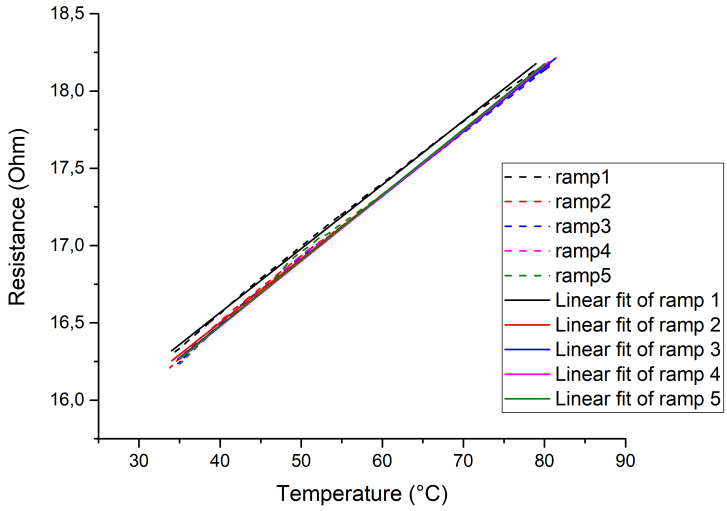

Figura 3.32: Data and linear fit of the ramps.

Ramp	**Slope** $(R_0 \cdot \alpha)$ $\Omega{\cdot}^{\circ}\mathrm{C}^{-1}$	**Error**	**Intercept** (R_0) Ω	**Error**	**Adjusted** R^2
1	0.04139	$3{\cdot}10^{-5}$	14.910	0.001	0.999
2	0.04159	$2{\cdot}10^{-5}$	14.832	0.001	0.999
3	0.04177	$3{\cdot}10^{-5}$	14.813	0.001	0.999
4	0.04225	$3{\cdot}10^{-5}$	14.786	0.002	0.999
5	0.04237	$4{\cdot}10^{-5}$	14.786	0.002	0.998
average	0.0419	$4{\cdot}10^{-4}$	14.81	0.05	

Tabella 3.2: Parameters of the linear fit and the weighted average.

gold ($\rho = 2.44 \cdot 10^{-8}\,\Omega m$ [9]). However this is not surprising for two reasons. First of all, the resistance measurements are 2-probe measurements (performed with a Wheatstone Bridge), characterized by the presence of a *contact resistance*, that is the additional contribution to the total resistance of the system attributed to the contacting interfaces of the electrical connections. In the previous version of the thermometer, with a Si substrate, the contact resistance was about one half of the 2-wire measurements. Mica is a softer substrate and the contact wire could produce easily a local damaging of the gold film, resulting in a even greater contact resistance. Compared to the old 4-wire measurements, the gold film resistance of a sample of the same thickness and area size was between 3 and 4 Ω. The resistivity in that condition was around $4 \cdot 10^{-8}\,\Omega \cdot m$, so we have roughly the same factor between the measured resistance and resistivity. A 4-wire measurements has not been performed because the working configuration is 2-wire and resistivity is not a vital parameter in the measurement economy.

3.2.2 Heat Transfer Calibration

In order to describe the heat transfer through the sample, we need to calculate the heat transfer coefficient for the different parts of the sample. In particular we can expect three different contributions: since the mica substrate acts as a thermal insulator, we expect a first and fast thermalization of the upper gold film with the underlying mica substrate, followed by a slower thermalization of the substrate with the sample holder, and finally a very slow thermalization of the sample holder with the environment. Moreover, we can separate the fast heat losses of the upper layer through the substrate from the subsequent losses towards the sample holder, described by two different heat transfer coefficients.
For the purpose of deriving these parameters we illuminate the sample for 60 seconds by using a lamp focused on the surface: the absorption of the optical power increases the temperature of the sample. Then we record the cooling of the system, which can be described with the following exponential decay:

$$\Delta T(t) = \Delta T(0) + A_1 exp\Big(-\frac{t}{\tau_1}\Big) + A_2 exp\Big(-\frac{t}{\tau_2}\Big) + A_3 exp\Big(-\frac{t}{\tau_3}\Big) \qquad (3.7)$$

in order to verify the presence of three different characteristic times of decay.
As shown in Fig. 3.34, we can fit the data, obtaining:

$$\tau_1 = (11.01 \pm 0.04)\, s \quad \tau_2 = (61.6 \pm 0.2)\, s \quad \tau_3 = (592 \pm 5)\, s$$

Since we are interested in the heat transfer through the sample, we can focus only on the first part of the cooling, which can be described without considering the longer thermalization with the environment:

$$\Delta T(t) = \Delta T(0) + A_1 exp\Big(-\frac{t}{\tau_1}\Big) + A_2 exp\Big(-\frac{t}{\tau_2}\Big) \qquad (3.8)$$

From the linear fit of the data (Fig. 3.33(b)) we obtain:

$$\tau_1 = (9.9 \pm 0.1)\, s \quad \tau_2 = (56 \pm 1)\, s$$

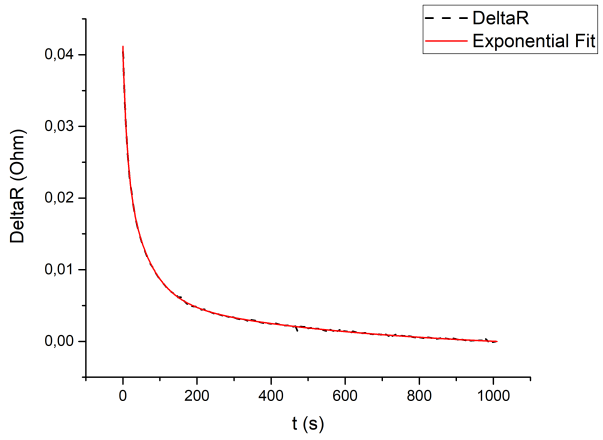

(a)

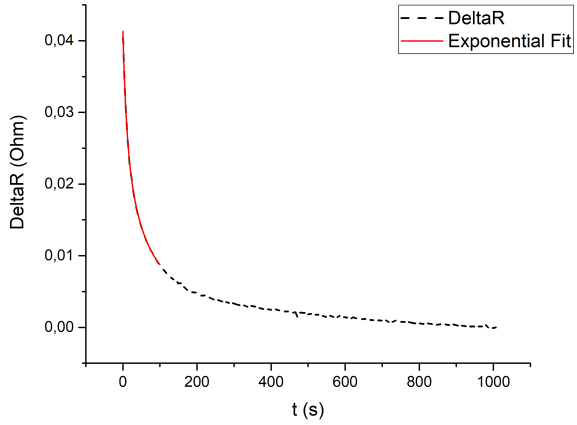

(b)

Figura 3.33: (a) Exponential fit (red line) of the cooling of the sample with three different characteristic times. (b) Exponential fit (red line) of the cooling of the sample with two different characteristic times.

Moreover, it is possible to compare the response of our sensor to the 60 seconds illumination with that of the first prototype of a gold film thermometer [1], which exploited a silicon substrate instead of a mica substrate:

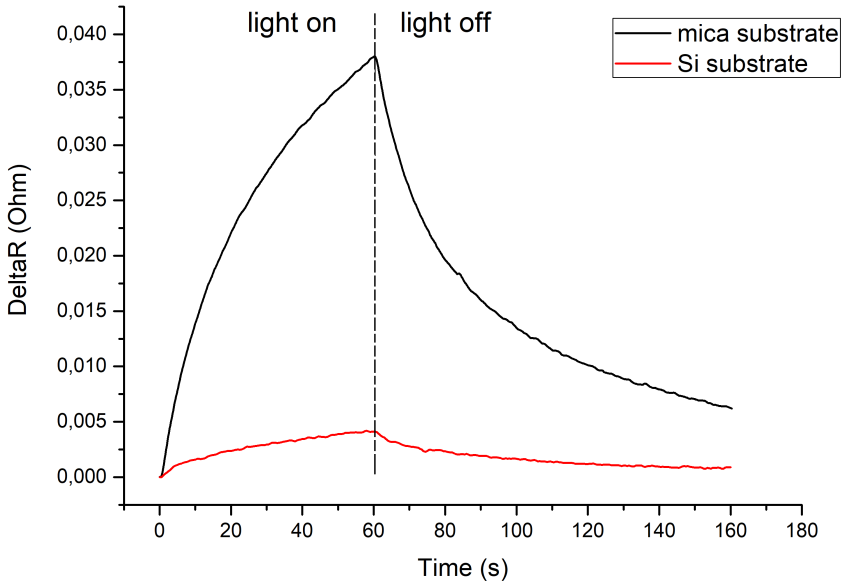

Figura 3.34: Plot of the response of our sensor to the illumination with a lamp for 60 seconds and comparison with the first prototype of gold film thermometer (silicon substrate).

It is evident that the resistance increase with the mica substrate is almost 10 times that of the old sensor ($\Delta R_{mica} = 0.038\,\Omega$, $\Delta R_{Si} = 0.004\,\Omega$), thus confirming that the sensitivity achieved with the new set-up is significantly higher.

Thermometer Application: atomic hydrogen adsorption

4

In order to test the performance of the gold film thermometer in a proof-of-principle experiment, we aim to detect the enthalpy released during the adsorption process of atomic hydrogen on the gold film itself. Indeed, in contrast to H_2 molecules, H atoms can be adsorbed on gold surfaces, at least at low temperatures [61–63]. Moreover we would like to compare the performance of our new thermometer with that of the first prototype of the sensor (silicon substrate).

4.1 Hydrogen adsorption on amorphous gold

We recall that the physical support of this thermometer is a ∼300 μm-thick substrate of silicon whose top face has been oxidized to have a 280 nm layer of SiO_2 acting as an electrical and thermal insulator. Then a thin layer of 5 nm of titanium, deposited on the substrate, allows the proper sticking of the upper 20 nm layer of gold. The STM images of the gold layer show a corrugated and inhomogeneous surface, as illustrated in Fig. 4.1 in the next page, taken from Ref. [1].

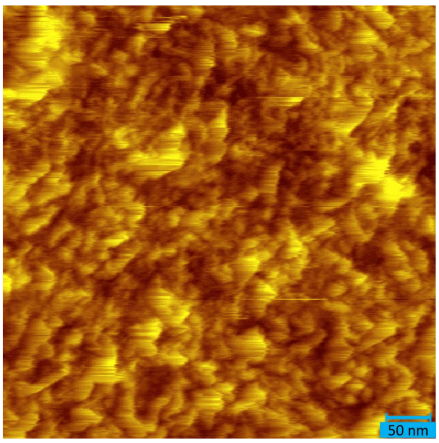

Figura 4.1: STM image of the Au layer from Ref. [1]. Image parameters: V=1.0 V, I=1.0 nA, average RMS roughness: (0.8±0.2) nm.

4.1.1 Calorimetric measurement

We have seen in section 1.1 that, in order to extract the unknown heat release which will heat the sensor during the exothermic adsorption of hydrogen, we can use the following equation:

$$\frac{\delta H_r}{\delta t} = C_{sensor} \cdot \frac{\delta \Delta T(t)}{\delta t} + \lambda \cdot \Delta T(t) \tag{4.1}$$

During the exposure of the sample to atomic hydrogen, we record the resistance evolution. The heat is released on the gold thermometer and slowly to the silicon substrate underneath. The sample can be considered as composed by two parts: the silicon substrate and the sensor. So we can calculate the heat capacity of the sensor:

$$C_{sensor} = C_{Au} + C_{Ti} + C_{SiO_2} \tag{4.2}$$

where C is the heat capacity and can be calculated by knowing c, the specific heat capacity, as:

$$C_{Au} = mass_{Au} \cdot c_{Au}$$
$$C_{Ti} = mass_{Ti} \cdot c_{Ti}$$
$$C_{SiO_2} = mass_{SiO_2} \cdot c_{SiO_2}$$

From the well known physical properties of gold, titanium and silica [64], we obtain for gold:

$$\rho_{Au} = 19.3\,\mathrm{g/cm^3}$$
$$c_{Au} = 0.129\,\mathrm{J/K \cdot g}$$

for titanium:

$$\rho_{Ti} = 4.507\,\mathrm{g/cm^3}$$
$$c_{Ti} = 0.52\,\mathrm{J/K \cdot g}$$

and for silica:

$$\rho_{SiO_2} = 2.196\,\mathrm{g/cm^3}$$
$$c_{SiO_2} = 0.703\,\mathrm{J/K \cdot g}$$

Knowing the dimensions (5.10 mm×5.95 mm of lenght and width for each layer) of the gold layer:

$$t_{Au} = 20\,\mathrm{nm}$$
$$A_{Au} = 30.345\,\mathrm{mm^2}$$

the titanium layer:

$$t_{Ti} = 5\,\mathrm{nm}$$
$$A_{Ti} = 30.345\,\mathrm{mm^2}$$

and the silica layer:

$$t_{SiO_2} = 280\,\mathrm{nm}$$
$$A_{SiO_2} = 30.345\,\mathrm{mm^2}$$

we finally obtain:

$$C_{Au} = \rho_{Au} \cdot t_{Au} \cdot A_{Au} \cdot c_{Au} = 1.51 \times 10^{-6}\,\mathrm{J/K}$$

$$C_{Ti} = \rho_{Ti} \cdot t_{Ti} \cdot A_{Ti} \cdot c_{Ti} = 0.36 \times 10^{-6}\,\mathrm{J/K}$$
$$C_{SiO_2} = \rho_{SiO_2} \cdot t_{SiO_2} \cdot A_{SiO_2} \cdot c_{SiO_2} = 13.12 \times 10^{-6}\,\mathrm{J/K}$$

Therefore the heat capacity of the sensor is:

$$C_{sensor} = 14.95 \times 10^{-6}\,\mathrm{J/K} \tag{4.3}$$

Next, we can calculate the heat transfer coefficient as $\lambda = C/\tau$, where τ is the characteristic time of cooling of the sample obtained as in section 3.2. For $\tau = (2.9 \pm 0.6)$ s we have:

$$\lambda = \frac{C_{sensor}}{\tau} = (5.1 \pm 1.1) \times 10^{-6}\,\mathrm{W/K} \tag{4.4}$$

With the values of C_{sensor} and λ we can now calculate $\delta H_r/\delta t$ from Eq.1.9 by using the $\Delta T(t)$ curve that we will obtain from the calorimetric measurement and performing a point-by-point derivative of the recorded data to obtain $\delta\Delta T(t)/\delta t$, as in Ref. [1]. Finally the enthalpy release H_r can be calculated from a point-by-point integration of $\delta H_r/\delta t$.

The sample has been exposed to atomic hydrogen for 5 minutes at a pressure of 1.0×10^{-7} mbar, while recording the sensor resistance.

As illustrated in Fig. 4.2 four different trends can be identified:

- the time interval between t_0 (instant at which we switch on the filament of the hydrogen cracker) and t_1 (instant at which the filament degassing is completed and the shutter in front of the hydrogen cracker is open) shows a linear trend of the sensor resistance against time, due to the gradual heating by the hot filament;

- the time interval between t_1 and t_2 (instant at which the hydrogen supply starts but the sample is backside oriented) is characterized by an exponential increase of the sensor resistance with time (now the shutter in front of the cracker is open);

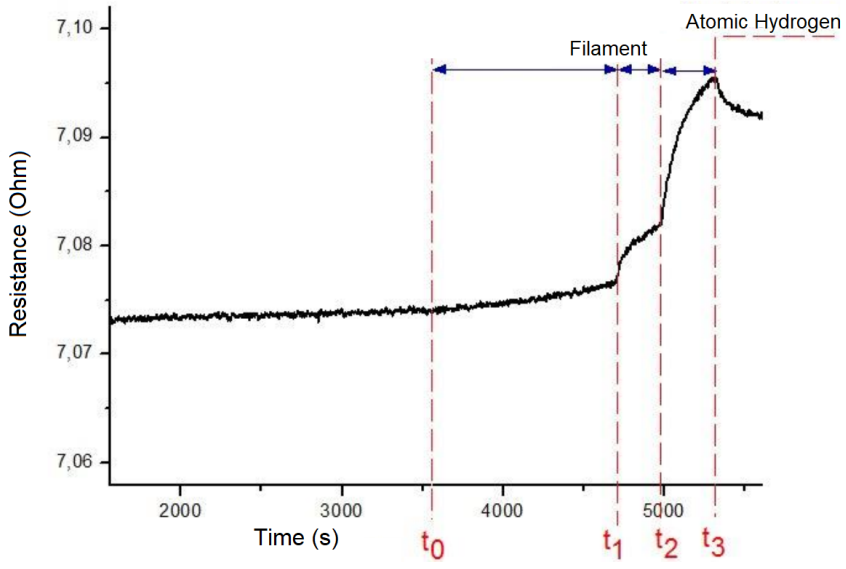

Figura 4.2: Sensor resistance variation during the the hydrogen exposure on the old sensor.

- finally, the time interval between t_2 and t_3 (instant at which the hydrogen supply is delivered on the sample which faces the cracker) exhibits a more pronounced exponential growth;
- after t_3 the hydrogen supply is stopped and the sample starts to cool down.

In order to analyse the interest period, related to the effective hydrogen exposure (from t_2 to t_3), the contributions due to the heating of the sample caused by the hot filament of the cracker must be subtracted, as shown in Fig. 4.3. In this way the resistance variation linked to the temperature increase can be estimated from the exponential fit of the curve presented in Fig. 4.3(c): $\Delta R \simeq 0.01\,\Omega$.

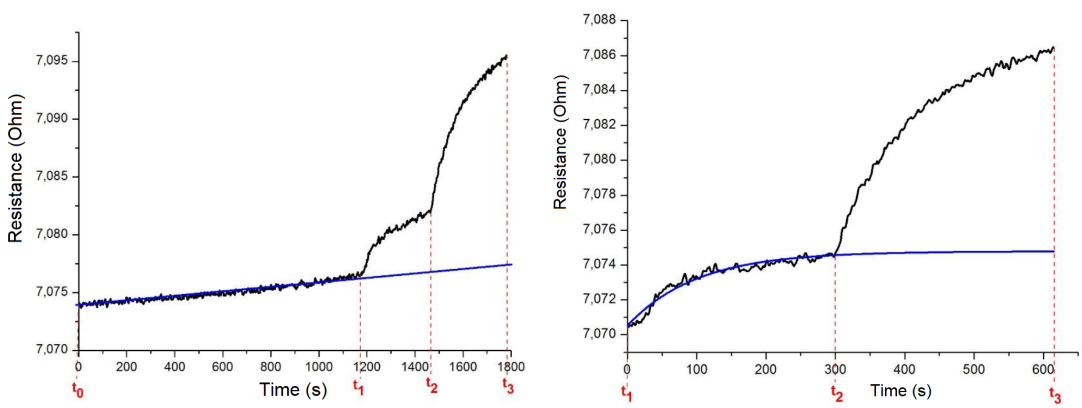

(a)

(b)

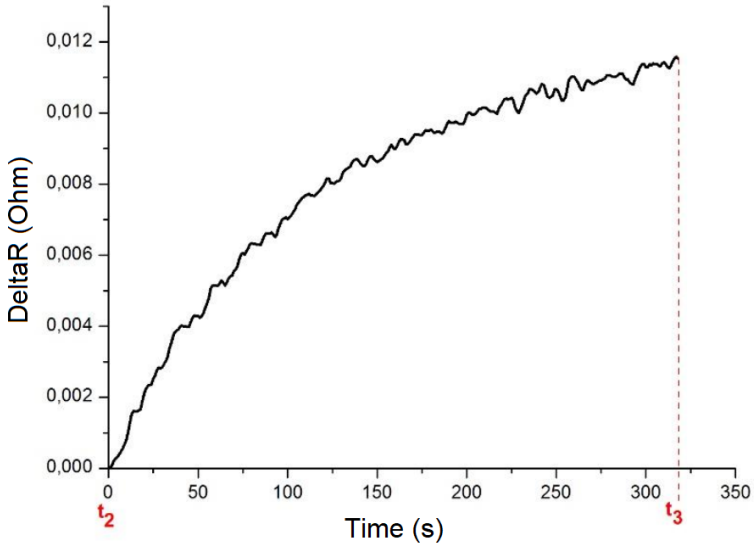

(c)

Figura 4.3: (a) Linear fit of the region related to the hot filament contribution (shutter closed). (b) Exponential fit of the region related to the hot filament contribution (shutter opened). (c) Sensor resistance variation after the subtraction of the unwanted contributions.

Therefore, we can perform a point-by-point derivative of $\Delta T(t)$ (obtained dividing $\Delta R(t)$ by $\alpha \cdot R_0$), thus obtaining the first term of Eq. 1.9. The second term is the simple product of the thermometric signal and the heat transfer coefficient previously calculated. Via point-by-point integration, from Eq. 1.9 we calculate the enthalpy release. $\delta H_r/\delta t$ is reported in Fig. 4.4, also showing the area integration which gives the value of H_r (yellow area).

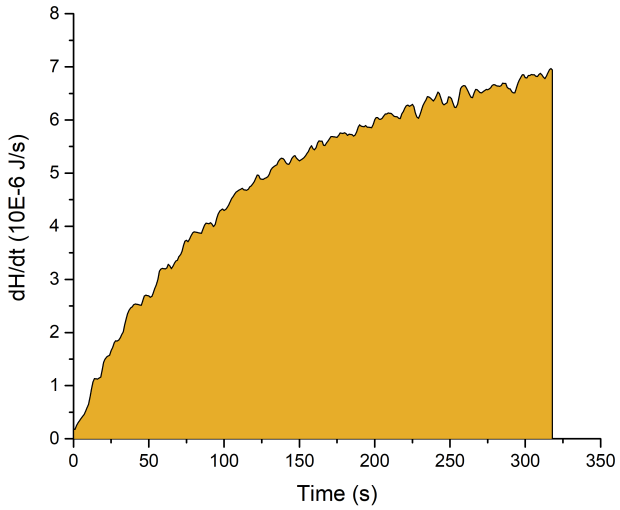

Figura 4.4: $\delta H_r/\delta t$ for H exposure of the old sensor (the integration area is shown in yellow).

In summary, for the amorphous gold sensor we have:

- $C_{sensor} = 14.95 \times 10^{-6}$ J/K
- $\tau = (2.9 \pm 0.6)$ s
- $\lambda = (5.1 \pm 1.1) \times 10^{-6}$ W/K

The enthalpy release H_r obtained for the adsorption process is: $H_r = 1.55 \pm 0.2$ mJ.

In order to determine the binding energy of H atoms and the amount of adsorbed hydrogen the TDS spectrum has been recorded.

4.1.2 Thermal Desorption Spectroscopy (TDS) measurement

The adsorption energy is measured more frequently by desorption, by breaking the adsorbate-surface bond. When the adsorbed layer of atoms (or molecules) is heated, the surface species can desorb because their surface residence time depends on temperature by an exponential law:

$$\tau = \tau_0 exp\left(\frac{\Delta E}{RT}\right) \tag{4.5}$$

where R is the gas constant, ΔE is the energy needed for the desorption process and τ_0 is the surface residence time when the surface is not heated.
If the adsorbate is not replenished from the gas phase, its concentration on the surface quickly decreases with increasing temperature, until the surface comes back clean. There is a preferential temperature at which the adsorbed atoms are removed from the surface for each adsorbate-substrate combination. By rapidly heating the surface to this optimal temperature, the adsorbed atoms are removed until their surface concentration is null. From the temperature at which the desorption peak occurs we can calculate the activation energy of desorption, which is linked to the binding energy of the adsorbed species.

Therefore, after the hydrogen exposure, the sample is placed in front of the Residual Gas Analyser (RGA) to perform a TDS measurement. The sample is heated at a constant rate of ~ 0.5 K/s from room temperature to around 650 K. A clear peak, related to the recombinative H_2 desorption, is detected at $T_p = 575 \pm 3$ K, as shown in Fig.4.5.

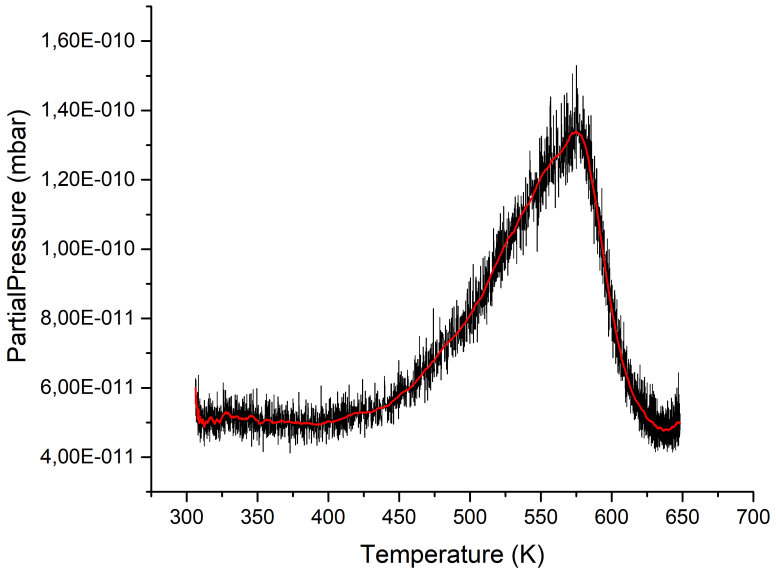

Figura 4.5: TDS spectrum vs Temperature for the old sensor, after 5 minutes of atomic hydrogen exposure at $P_H = 1.0 \times 10^{-7}$ mbar. It shows a clear desorption peak at $T_p = 575 \pm 3$ K.

The activation energy of desorption is obtained from eq. 2.8, after having extracted the time τ_m from the start of the desorption ramp to the moment at which the desorption peak is reached. The calculated activation energy amounts to $E_d = 1.65 \pm 0.04$ eV.
Since the recombination and desorption of H_2 includes the formation of H-H bonds, in order to calculate the binding energy between the H atom and the amorphous gold surface, we need to know the relation between the H-H binding energy E_{H-H}, the H-Au binding energy E_b (the value we are interested in) and the H_2 activation energy E_d (that we have just calculated):

$$2E_b = E_d + E_{H-H} \tag{4.6}$$

Using the value of 4.52 eV for E_{H-H} [42], the binding energy between the H atom and the gold surface is estimated to be: $E_b \simeq 3$ eV, slightly higher than that reported in [42] (2.40 eV).
From equation 2.9 we can estimate the amount of desorbed hydrogen: $n = 2.2 \times 10^{-10}\, mol$ in mol which corresponds to $13.25 \times 10^{13}\, molecules$ of H_2. The heat release is obtained by multiplying the average binding energy per atom and the number of hydrogen atoms desorbed: $H_r \simeq 1.3\, m$J in good agreement with the calorimetric evaluation.

4.2 Hydrogen adsorption on Au(111)/mica

In order to compare the performance of our new sensor with that of the old one, we have exposed to atomic hydrogen two samples, M5-4 and M6-2.

4.2.1 Calorimetric measurement

During the exposure to atomic hydrogen, we record the resistance evolution. The heat released during the experiment is rapidly transferred to the gold thermometer and the mica substrate underneath. Indeed the sample is composed of two parts: the mica substrate and the sensor, which is the gold film thermometer. We can therefore calculate the heat capacity of the sensor:

$$C_{sensor} = C_{Au} \tag{4.7}$$

where the heat capacity C can be calculated knowing the specific heat capacity c as:

$$C_{Au} = mass_{Au} \cdot c_{Au} \tag{4.8}$$

From the well known properties of gold [64] we obtain:

$$\rho_{Au} = 19.3\,\mathrm{g/cm^3}$$

$$c_{Au} = 0.13\,\mathrm{J/K \cdot g}$$

Knowing the dimensions (7.00 mm × 6.35 mm for M5-4 and 6.90 mm × 6.60 mm for M6-2) of the gold layer:

$$t_{Au} = 20\,\text{nm}$$

$$A_{AuM5-4} = 44.45\,\text{mm}^2 \quad A_{AuM6-2} = 45.54\,\text{mm}^2$$

we finally obtain:

$$C_{sensorM5-4} = \rho_{Au} \cdot t_{Au} \cdot A_{AuM5-4} \cdot c_{Au} = 2.21 \times 10^{-6}\,\text{J/K}$$

$$C_{sensorM6-2} = \rho_{Au} \cdot t_{Au} \cdot A_{AuM6-2} \cdot c_{Au} = 2.27 \times 10^{-6}\,\text{J/K}$$

We have calculated the total heat capacity of the sensor C_{sensor}; so we can calculate the heat transfer coefficient as $\lambda = C_{sensor}/\tau$, where τ is the characteristic time of cooling of the sample calculated in section 3.2.2, $\tau = 9.9 \pm 0.1$ s. Therefore we obtain:

$$\lambda_{M5-4} = C_{sensorM5-4}/\tau = (2.23 \pm 0.02) \times 10^{-7}\,\text{W/K}$$

$$\lambda_{M6-2} = C_{sensorM6-2}/\tau = (2.29 \pm 0.02) \times 10^{-7}\,\text{W/K}$$

So $\delta H_r/\delta t$ can be calculated from eq. 1.9, as explained in the previous section.

M5-4 and M6-2 have been exposed to atomic hydrogen after their degassing and annealing up to 200°C (in order to obtain a sensor with a reconstructed, atomically flat surface), and after the proper calibration.
The samples have been exposed to atomic hydrogen for 5 minutes at a pressure of 1.0×10^{-7} mbar, while recording the sensor resistance. We expected to observe a resistance (and thus temperature) increase due to the adsorption process, as with the amorphous gold sensor, however we observed a peculiar trend.

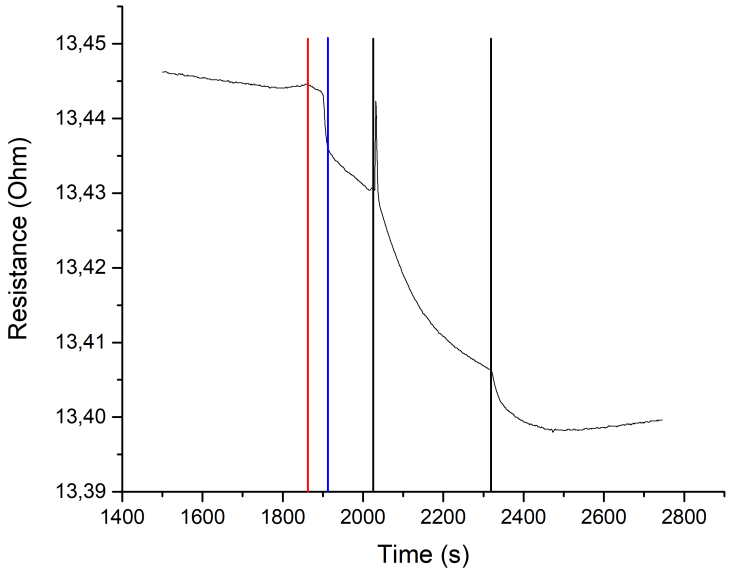

(a)

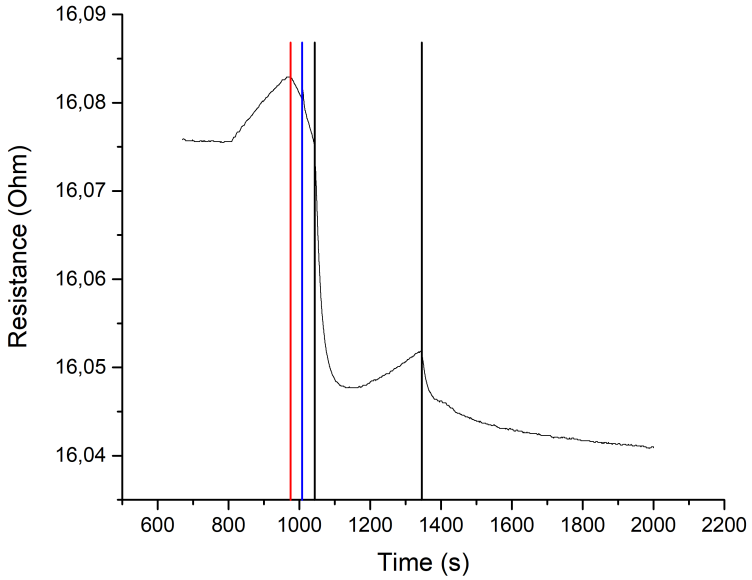

(b)

Figura 4.6: (a) Sensor resistance variation during the the hydrogen exposure on the sample M5-4.(b) Sensor resistance variation during the the hydrogen exposure on the sample M6-2.

The black lines in Fig. 4.6(a) and 4.6(b) delimit the time interval corresponding to the effective hydrogen exposure, during which the shutter in front of the hydrogen cracker is opened. The red line indicates the instant at which the pressure reaches the desired value of 1.0×10^{-7} mbar, while the blue line indicates the instant at which the sample is rotated with its frontside facing the hydrogen cracker.
It is evident that the experiment starts in the tail of a slightly decreasing trend (cooling of the sample) due to the previous calibration ramps which heated the sample, the sample resistance starts to increase because it is heated by the hot filament of the hydrogen cracker, as expected. Then, once reached the target pressure (red line) a linear decreasing trend gets going and it becomes even more marked when the sample is rotated with its frontside upwards, facing the cracker, and the effective hydrogen exposure takes place (shutter opened). When the shutter is closed a cooling tail reflects the fact that the sample has been actually heated in spite of the resistance decrease.
The exponential fit of the part of the curve delimited by the black lines gives a resistance variation of $\Delta R \simeq 0.03\,\Omega$. This behaviour is completely unexpected: the exothermic reaction that binds atomic hydrogen to gold atoms should determine a heating, and so the increase of the sensor resistance, according to the relation 3.1, and as observed with the old sensor.
In order to better understand this peculiar behaviour, the samples are subjected to a Thermal Desorption Spectroscopy measurement. It is worth recalling that the TDS measurement is a destructive measurement because it involves the heating of the sample up to temperatures that damage the sample itself, as deeply explained in section 3.1.4.

4.2.2 Thermal Desorption Spectroscopy (TDS) measurement

In order to determine the binding energy of H atoms (if they have been adsorbed on the gold sensor) and the amount of adsorbed hydrogen we heat the surface and measure the desorbed atoms with a mass spectrometer. Therefore, after the hydrogen exposure, the samples are placed in front of a Residual Gas Analyser (RGA) to perform a Thermal Desorption Spectroscopy (TDS) measurement. The samples are heated at a constant rate of ~ 0.6 K/s from room temperature up

to around 600 K. The heating rate has been checked by the linear fit of the TDS ramp, as shown in Fig.4.7(c) and 4.7(d). A clear peak, related to the recombinative H_2 desorption, is detected at $T_p = 408 \pm 2$ K (Fig. 4.7(a), 4.7(b)); this peak is followed by the typical ascending tail which characterizes the degassing of the sample. Indeed, it should be remembered that the samples have been degassed up to temperatures of about 400 K ($\sim$100 °C), because higher temperatures would have damaged the samples, as shown in section 3.1.4. We can see that the desorption peak relating to M6-2 is lower than that observed for M5-4, most likely because in this case the TDS measurement has been performed several hours after the hydrogenation process has been completed.

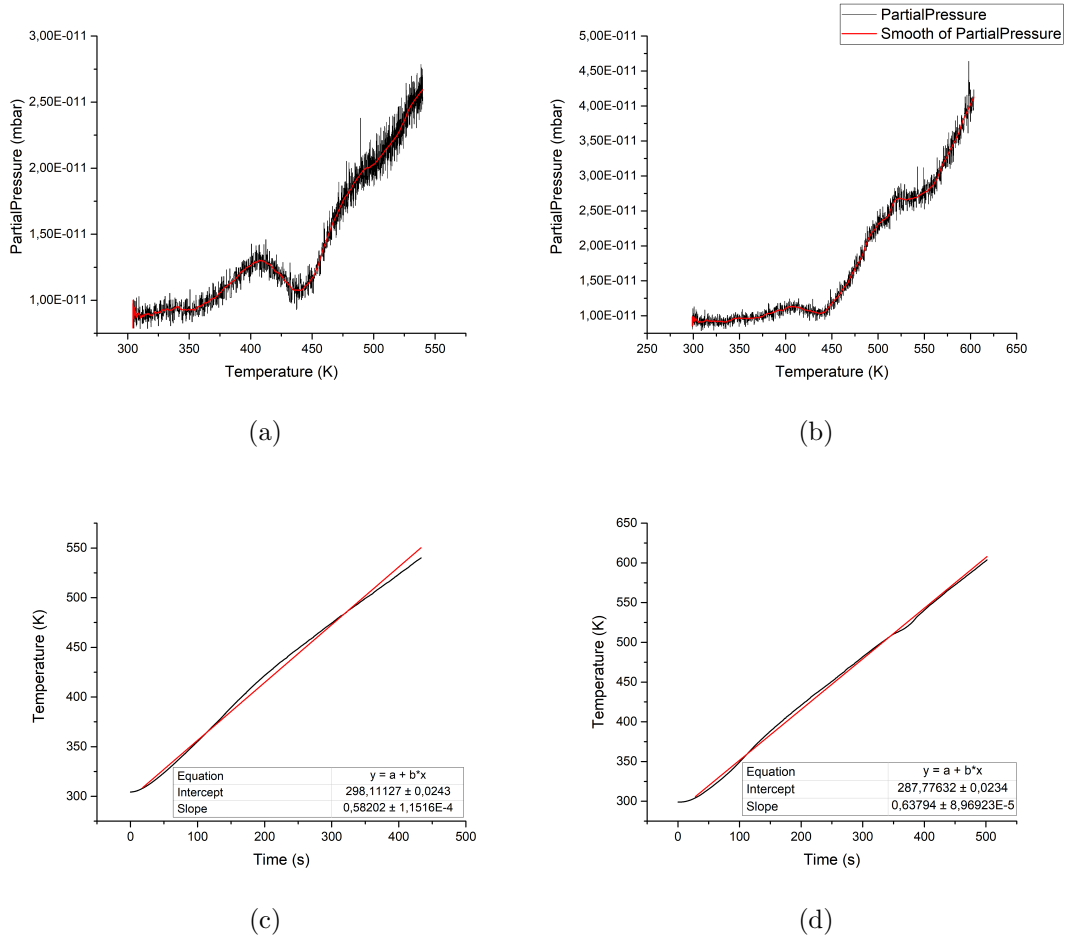

(a) (b) (c) (d)

Figura 4.7: (a) TDS spectrum vs Temperature for sample M5-4, after 5 minutes of atomic hydrogen exposure at $P_H = 1.0 \times 10^{-7}$ mbar. It shows a desorption peak at $T_p = 408 \pm 2$ K. (b) TDS spectrum vs Temperature for sample M6-2, after 5 minutes of atomic hydrogen exposure at $P_H = 1.0 \times 10^{-7}$ mbar. It shows a desorption peak at $T_p = 408 \pm 2$ K. (c) Linear fit of the TDS ramp performed on sample M5-4. (d) Linear fit of the TDS ramp performed on sample M6-2.

After having extracted the desorption temperature, we can calculate the time from the start of the desorption ramp to the moment at which the desorption peak T_d is reached, so as to obtain the activation energy of desorption E_d from eq. 2.8:

Sample	T_p (K)	τ_m (s)	E_d/molecule (eV)
M5-4	(408±2)	(178±1)	(1.11±0.03)
M6-2	(408±2)	(180±1)	(1.12±0.08)

Tabella 4.1: Temperature of the desorption peak T_p, heating time τ_m and activation energy of desorption E_d/molecule, calculated from the TDS measurements.

Using Eq. 4.6 and knowing that $E_{H-H} = 4.52$ eV, we estimate the binding energy between the H atom and the Au(111): $E_b = 2.82$ eV for both the samples, lower than the value calculated for amorphous gold.

The amount of desorbed (and therefore previously stored) hydrogen can be estimated from the TDS spectra showing the partial pressure of atomic hydrogen in function of the time, using Eq. 2.9. Therefore, after the subtraction of the background, we perform an integration of the TDS spectrum, obtaining the area under the curve, F (in mbar·s), as shown in Fig. 4.8.

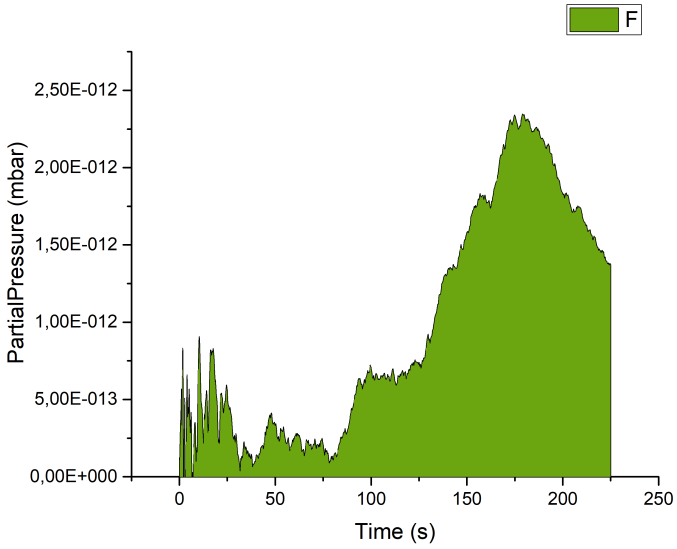

Figura 4.8: Integration of the TDS spectrum obtained for M6-2.

The resulting amount of desorbed hydrogen for M5-4 and M6-2 is reported in Table 4.2.

Sample	F (mbar·s)	H_2 (mol)	H_2 (molecules)
M5-4	$(3.36\pm0.02)\times10^{-10}$	4.11×10^{-12}	24.75×10^{11}
M6-2	$(2.21\pm0.02)\times10^{-10}$	2.70×10^{-12}	16.26×10^{11}

Tabella 4.2: Amount of desorbed hydrogen, in mol and number of H_2 molecules (1 mol= 6.022×10^{23} molecules).

Finally we can estimate the heat release during the adsorption of atomic hydrogen on gold. It can be obtained by multiplying the average binding energy per atom and the number of hydrogen atoms desorbed:

$$H_r(M5-4) = 2.24 \pm 0.02\,\mu\text{J}$$

We only reported the result relating to M5-4 because the the value for M6-2 has no meaning, since the TDS measurement for this sample has been performed several hours after the hydrogenation process. We can see that this time the amount of hydrogen stored in the sample is about three orders of magnitude lower than that recorded for amorphous gold.

It is possible to conclude that hydrogen atoms adsorbed on gold surface, even in smaller amounts, but probably something happened (in addition to the adsorption process) that caused the resistance decreasing. The behaviour observed with M5-4 and M6-2 is completely different from that recorded for the first prototype of the sensor (described in the previous section). It appears from the TDS analysis that the amount of hydrogen stored in the new gold sensor is much lower than that recorded for amorphous gold. Moreover the calorimetric behaviour of the old sensor is consistent with our expectations. If we neglect the substrate, which merely affects the sensitivity of the thermometer, the only difference between the two sensors is the surface reconstruction. Let us remember that our new thermometer allows to fully exploit the STM capability: so we can use it to

investigate the sensor surface after the hydrogenation process.
In order to do that, a new sample, M6-3, has been exposed to atomic hydrogen.

4.2.3 STM analysis

M6-3 has been exposed to atomic hydrogen after its degassing and annealing up to 200°C (in order to obtain a sensor with a reconstructed, atomically flat surface), and after the proper calibration. The sample has been exposed to atomic hydrogen for 5 minutes at a pressure of 1.0×10^{-7} mbar, while recording the sensor resistance. We observed the same trend recorded for M5-4 and M6-2. The exponential fit of the part of the curve delimited by the black lines gives a resistance variation of $\Delta R \simeq 0.04\,\Omega$, slightly higher than that recorded for the other two samples. After the hydrogenation, we did not perform a TDS measurement (which is destructive), but instead we studied the sample with STM to assay any changes in the surface reconstruction.

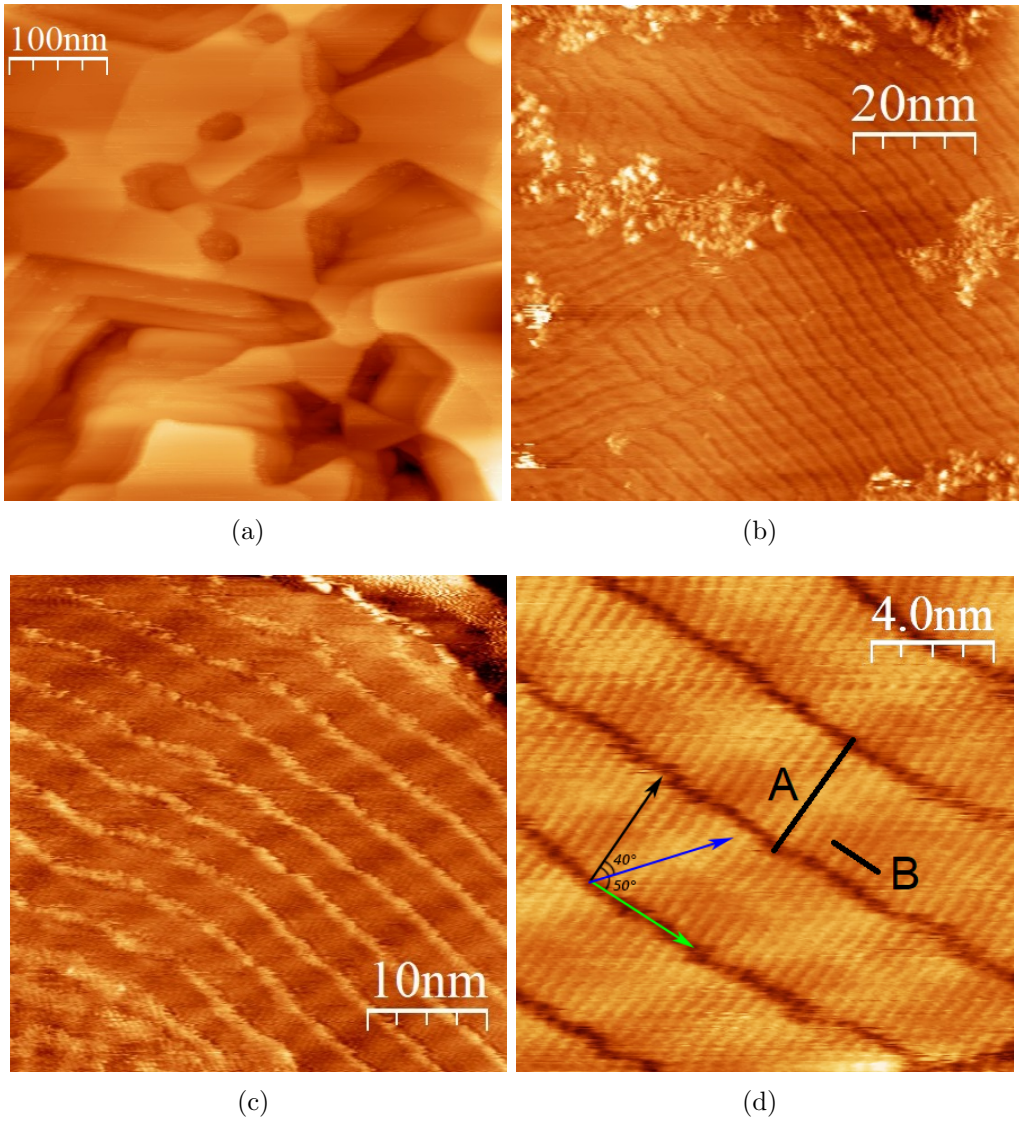

Figura 4.9: (a) STM images of 500×500 nm^2, (b) 80×80 nm^2, (c) 40×40 nm^2 and (d) 16×16 nm^2 of sample M6-3 after the hydrogenation process.

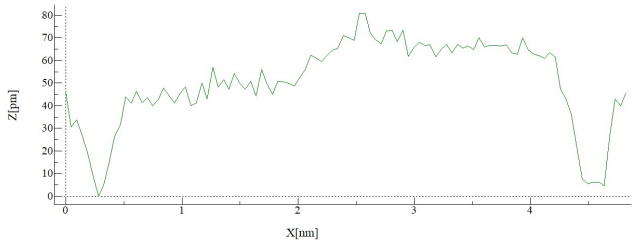

(a)

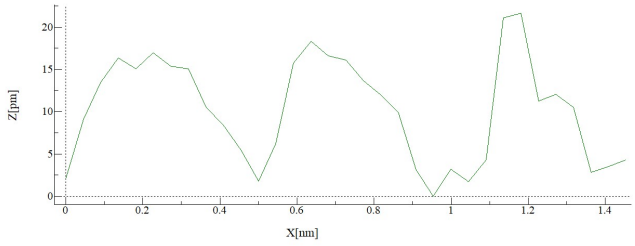

(b)

Figura 4.10: (a) and (b) Line scans shown in Fig. 4.9 along A and B, respectively.

We can see that the topography of the gold surface is characterized by large, atomically flat terraces, which extend over many hundred nanometres (Fig.4.9(a)). If we zoom in, down to 80×80 nm^2, it is evident that the periodic pattern of pairwise-arranged, parallel lines which characterizes the (111) reconstruction is different from that previously observed (see section 3.1). The corrugation lines are closer together and sometimes orthogonal pairs criss-cross and blend without U connections, as shown in Fig. 4.9(b).
The distance between neighbouring pairs now amounts to 38 ± 3 Å, and has to be compared with 56 ± 7 Å, which is the value obtained after the annealing of the sample (before hydrogenation), when the (111) reconstruction has been completed (see section 3.1.1). The corrugation amplitude is different as well. Whereas before the ratio between the vertical corrugation line and the depression in the hcp regions (between the two lines of each pair) was about 1, now it is almost 2.

Moreover, in some areas, a peculiar striped pattern can be observed (Fig. 4.9(c) and4.9(d)), even if the herringbone reconstruction pattern underneath is still faintly visible. The striped pattern is composed of fine stripes and vacancy lines that are oriented perpendicular to these fine stripes. Sometimes the vacancy lines appear as corrugations (as in Fig. 4.9(c)) rather than as depressions. This behaviour is due to the changes in the tunneling parameters (V_t, I_t). Moreover, the vacancy line exhibit a frizzy appearance, which could be related to the occurrence of dynamic events during imaging and mainly occurs at the edges of the vacancy lines. The STM image shown in Fig. 4.9(d) reveals an angle of about 40° for orientation of the fine stripes (indicated by the black arrow in the same figure) with respect to the ridges of the Au herringbone reconstruction (indicated by the blue arrow); while the angle between the herringbone reconstruction and the broad stripes (indicated by the green arrow) is about 50°. In addition the fine stripes are often out-of-phase with respect to their neighbouring fine stripes at the other side of the vacancy line.
The spacing between the vacancy lines amounts to $4.12 \pm 0.25\,nm$. The line scan in Fig. 4.10(a) reveals that the depth of the trough between the broad stripes is between 50 and 60 pm. The stripes are composed of fine stripes which are aligned in a direction perpendicular to the vacancy lines (see Fig. 4.9(d)). The separation between these fine stripes is $0.5 \pm 0.1\,nm$ and their vertical corrugation amplitude is $25 \pm 5\,pm$ (see the line scan in Fig. 4.10(b)). This structure is consistent with results reported in Ref. [65] as discussed in the following.

It is known that the act of adsorption gives rise to a dynamic change of surface structure, often reversible, sometimes permanent. Thus, the surface structure cannot be viewed as being static during adsorption reactions, but can change markedly as the nature and the concentration of adsorbates are varied (see [66]). When atoms or molecules adsorb on relaxed clean surfaces and form chemical bonds, the surface atoms are placed in a different chemical environment. They change their equilibrium positions as a result. Upon adsorption, any clean surface relaxation is generally reduced, as the surface atoms of the substrate move back towards the ideal bulk-like positions. This phenomenon is perhaps the simplest form of adsorbate-induced restructuring of surfaces. Moreover adsorbates frequently destroy existing reconstructions of clean surfaces: the substrate then

usually takes on the bulk structure again. It appears that the adsorbate substitutes for the missing atoms due to the original creation of the surface: the adsorbate places the surface atoms in a more bulk-like environment. Even small amounts of adsorbate may be sufficient to destroy or modify a reconstruction. Besides an unreconstructed clean substrate can be induced to reconstruct by adsorbates or there are cases where a clean-surface reconstruction is changed by an adsorbate into another type of reconstruction. Hydrogen on W(100) and Mo(100) provides examples of this process [67]. Clean W(100) and Mo(100) are characterized by a reconstructed surface with long zigzag chains of surface metal atoms. When hydrogen is adsorbed, the tendency is to break up these chains into individual W-H-W or Mo-H-Mo trimers. Each H atom bridges a pair of W or Mo atoms, replacing the zigzag chain geometry.
Given the above, it might be thought that the structure observed with the STM measurement is linked to the hydrogen adsorption on the sample. Moreover very similar STM images are reported in Ref. [65]. In this research work, self-assembled monolayers of 4-[4'-(phenylethynyl)-phenylethynyl]-benzenethiolate (PPB-S) molecules on flame annealed Au(111) have been investigated by UHV scanning tunneling microscopy. They have found a self-assembled monolayer phase which consists of a fine-striped pattern that is aligned along the close packed $[1\bar{1}0]$ directions of the Au(111) surface. The fine-striped pattern is separated by narrow vacancy lines which are oriented perpendicular to the fine-striped pattern. Besides, spatially resolved current-time scanning tunneling microscopy experiments revealed that the PPB-S molecules at the edges of the vacancy lines exhibit dynamic behaviour and frequently jump back and forth between neighbouring stripes.
Therefore we could suspect that the striped pattern observed in our STM images is related to the arrangement of the H_2 molecules on the gold surface. It would be interesting performing an experiment of current-time scanning tunneling microscopy at the edge of our vacancy lines, in order to understand the dynamics that lies beyond the frizzy appearance of the vacancy lines.
The resistance descrease could be explained in terms of the scattering mechanisms related to surface defects (see [68]). Indeed, the pattern of pairwise-arranged lines which characterizes the Au(111) surface can be considered as a surface defect, because it involves the emergence of an additional corrugation on the gold surface, thus reducing the mean free path of the conduction electron and therefore

decreasing the electrical resistivity. The appearance of the new denser structure could have homogenised the gold surface (the fine stripes are closer together than the corrugation lines in a pair, or in neighboured pairs) thus increasing the mean free path of the conduction electron, and this behaviour could be reflected in the calorimetric measurement.

Conclusions and Outlook

5

In this thesis work we have developed a sensitive atomically flat gold film thermometer, which consists of a 20 nm-thick gold layer, having as physical support a ∼250 μm-thick substrate of mica. The first important result of this research is the improvement, in terms of sensitivity, of gold film thermometers. This upgrade originated from the replacement of the silicon substrate (used in Ref. [1]) with a *mica* substrate, whose thermal conductivity is about 300 times lower [16, 17]. Therefore, the heat transfer coefficient, which represents the heat losses of the sensor (gold layer) towards the substrate, (see the simple thermal model described in section 4), turns out to be more than one order of magnitude lower than that reported in Ref. [1]: $\lambda \sim 2 \cdot 10^{-7}$ W/K (to be compared with $\lambda \sim 5 \cdot 10^{-6}$ W/K of silicon), thus improving the thermal decoupling by a factor ∼25.
Our detailed STM measurements on these gold film thermometers have demonstrated that they are stable up to a temperature of 250 °C, above which they change morphology due to agglomeration of the gold. A possible solution to this issue could be an additional Ti layer underneath gold, utilizing the fabrication procedure set up in this thesis work.
The gold surface re-crystallization allowed by the mica substrate has been extensively studied, by varying the fabrication procedure in order to optimize the process. In particular, we have analysed the sensor behaviour with changing substrate conditions and annealing temperatures. The re-crystallized gold surface offers large flat terraces suited to investigate the processes which can affect the surface structure with atomic resolution. This new feature has allowed to discover

that atomic hydrogen binds to amorphous gold and crystalline gold in different ways. In particular we found that the hydrogen arranges itself in a peculiar striped pattern, composed of fine stripes and vacancy lines that are oriented perpendicular to these fine stripes. This observation highlights the opportunities offered by the atomically flat surface of the gold re-crystallization on a mica substrate. This kind of sensors open the way to the systematic use of STM capabilities in understanding physics at surface. In order to better investigate this phenomenon, observed on the gold surface after the hydrogenation, we suggest to repeat the hydrogen supply experiment and then analyse the sample with both STM and LEED measurements (the latter have not been performed yet).
Moreover, our atomically flat thermometer would allow a detailed study of graphene functionalization with alkali metals or organic molecules, which was not possible with the first prototype of the sensor, due to its atomically rough surface.
Finally, mica properties make this sensor suitable to have a remarkable impact on flexible electronics. Indeed, in the present era of "Internet-of-Things", the demand for flexible, light-weight, low-cost, low-power consumption, multifunctional and environmentally friendly electronics has moved to the forefront of materials science research.

Titanium diffusion in gold thin films

Titanium thin films are widely employed in electronic and micro-electromechanical devices as adhesion layer between insulators and conductive metallic layers, such as gold, used for electric contacts and signal transmission lines [69]. Thin films and multilayered systems are exposed to the risk of undergoing severe interdiffusion phenomena because the constantly decreasing size of electronic components imposes severe service conditions, such as high current densities and therefore high local temperatures. These interdiffusion phenomena can induce dramatic changes of the material properties and compromise performance and reliability of the components. This is why diffusion phenomena in titanium/gold thin films occurring at temperatures ranging between 200 and 400°C have been investigated [51]. In Ti/Au thin films, due to local high current density, the temperature can increase to such high values to induce interdiffusion between Ti and Au. Such diffusion process can promote the formation of TiAu intermetallics and/or, if Ti diffuses through Au up to the free surface, the formation of TiO_2, which in turn can cause an undesired ohmic resistance. As an example, in [51] the samples were prepared by sputtering Ti (thickness 200 nm) and Au (260 nm) on silicon substrates that then underwent different annealing treatments in air at temperatures ranging between 200 and 400°C. The specific atomic concentration profiles necessary to determine the diffusivity coefficients were obtained by Secondary Ion Mass Spectroscopy (SIMS). X-ray Photoelectron Spectroscopy (XPS), X-ray Diffraction (XRD) and Scanning Electron Microscopy (SEM) analyses were also

employed to characterize the samples upon the different thermal treatments. The report is briefly summarized in the following.
Fig. A.1 shows the composition profiles for the Au/Ti system upon exposure to different heat-treatments; a depth equal to zero corresponds to the gold free surface. In the case of the sample "as-deposited", these profiles allow for the identification of the different layers before interdiffusion occurred: from left to right, the Au film first, then the Ti layer followed by the thin thermally grown SiO_2, and finally the silicon substrate. Exposure to 200°C for 10h already affects the atomic composition profile of the sample, as shown in Fig. A.1(b). The Ti concentration increases at depth ranging between 100 and 150 nm and also above 550 nm suggesting that Ti diffuses also into the Si substrate. However, it is only upon heat treatment at 250°C that a significant concentration of Ti ($\sim$5%) as well as O atoms could be detected on the Au free surface (Fig. A.1(c)). Annealing at 300°C for 1h (Fig. A.1(d)) results in a concentration of Ti atoms of about 10% (for depth=0). Notably, upon exposure at 350°C for 10h, Au and Ti result highly intermixed. XPS analysis was performed on the sample annealed at 400°C, in order to determine the chemical composition of the species present on the surface. The strong signals corresponding to Ti and O suggest that, once reached the surface, Ti can easily react with oxygen present in the environment and create an oxide layer. Samples annealed for 10h in air at 300°C, 350°C and 400°C underwent also XRD analysis, which confirmed the SIMS results.

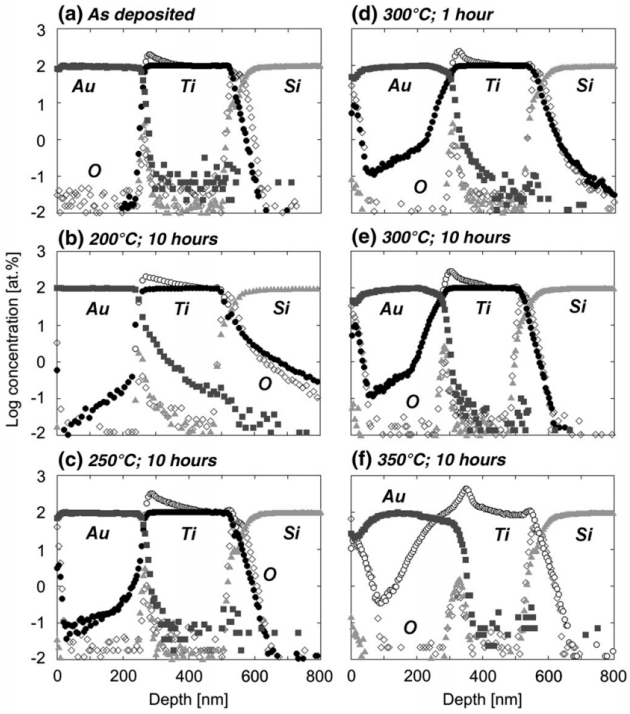

Figura A.1: Concentration profiles obtained from the SIMS analysis of the thin film samples from [51].

The water issue

B

All surfaces exposed to ambient conditions are covered by a thin film of water. Except at high humidity conditions, namely relative humidity (RH) higher than 80%, those water films have nanoscale thickness. Nevertheless, even the thinnest film can profoundly affect the physical and chemical properties of the substrate. Water films alter the adhesion and lubricating properties of surface and the reactivity of solids with ambient gas molecules.

Information on the structure of these water films can be obtained from spectroscopic techniques based on photons, but these usually have poor lateral resolution. Although modern scanning probe microscopes, like STM and AFM, have atomic-scale resolution, they cannot be easily used to study free liquid surfaces. For liquids, if the probe tip comes into contact with the surface, strong capillary forces will cause the liquid to wet the tip and will strongly perturb the liquid. To avoid the bulging of the liquid surface that leads to wetting and capillary interaction, the tip must be kept at least several tens of angstroms from the surface.

In this respect, different non-contact AFM modes have been proposed to obtain robust measurements of surface liquid films [70, 71]. Non-contact means that, with these methods, mechanical contact between the tip and the sample is avoided. Long-range interactions between the tip and the sample are used that allow imaging at some distance from the sample thus minimizing water perturbation. The two main methods used for this purpose take advantage of long-range electrostatic [70] or van der Waals interactions [71].

A method which uses electrostatic interactions to image liquid films on surfaces, avoiding mechanical tip-sample interaction, was developed two decades ago based on a non-contact mode of operation known as Scanning Polarization Force Microscopy (SPFM) [70]. In SPFM, in order to perform non-contact electrostatic AFM imaging, a conductive tip is brought to about 10-20 nm above the sample surface and electrically biased to a few volts. This creates attractive electrostatic forces between the tip and the polarizable surface. Topographic images can be obtained by maintaining the polarization force constant through feedback control of the tip-sample distance. In the first SPFM measurements, the technique was used to study water films on a mica surface [54, 55]. In [54] the water-imaging experiments were carried out at room temperature (21°C) in an environment chamber housing the AFM. High humidity was achieved by evaporating water from a beaker. The mica samples were prepared by cleavage and were typically several tenth of millimetres thick. The condensation process is described as made up of two distinct structural phases. Up about 25% humidity, the water film grows by forming two-dimensional clusters of less than a few thousand angstroms in diameter (phase I). Above about 25% humidity, a second phase grows, forming large two-dimensional islands. An interesting finding of this study was that the the boundaries of the islands were often polygonal, with angles of 120° as shown in Fig. B.1. By comparing SPFM images with contact images of the mica lattice, it was found that the directions of the boundaries were related to the mica crystallographic directions. On the basis of this observation, the authors suggested that the molecularly thin water film has a solid, ice-like structure, in epitaxial relationship with the substrate.

The islands which characterize the second phase increase in size until they cover the surface uniformly at 40 to 50% humidity.
The apparent height of the islands in both phase I and II (∼2 Å) suggests that the thickness of the water layer is of molecular dimensions. This is supported by the ellipsometric measurements that indicate that for humidities up to 50% the average thickness of the water film on mica is around 2 Å, i.e. one molecular layer thick.
Let us remember that mica structure consists of stacked layers held together by

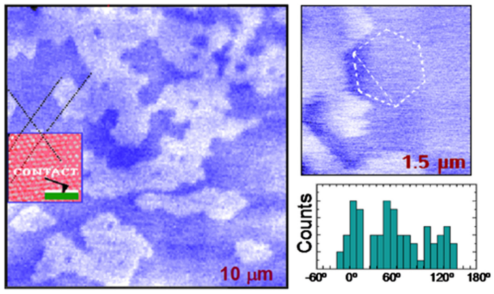

Figura B.1: SPFM images of structures formed by water on mica, from [54]. Bright areas correspond to a second water layer and dark areas to the first water layer. The boundaries tend to have polygonal shapes, as shown in the smaller image where a hexagon is drawn for visual reference. The directions are strongly correlated with the mica lattice. The inset in the large image shows a contact AFM image obtained after the SPFM images, which provides a reference for angle measurements. The histogram shows the angles of the water-film boundaries relative to the mica lattice.

electrostatic forces. Pairs of negative layers are held together by K^+ ions. When mica is cleaved into atomically smooth sheets, the aluminosilicate portion remains intact and the K^+ ions become divided onto the newly formed (001) faces. The positive ion partitioning is never quite even, and each sheet initially is electrostatically charged [72]. These charge soon dissipate from the ambient laboratory surroundings settle on the surface and neutralize them. Since the surface of mica is hydrophilic, water spreads readily on the freshly prepared surface. The authors of [70] propose that phase I includes water molecules solvating K^+ ions. This interpretation is supported by infrared spectroscopy studies of layered silicates that show that when the water content is low, the molecules are tied into solvation shells around the intercalated ions. At higher water contents, the formation of nonsolvated water (hydrogen bonded) is observed.

It is worth discussing the reliability of these thickness measurements.
In the SPFM images, output signals corresponding to topography and sample polarizability are coupled. When imaging thin films on a substrate exhibiting very different dielectric constants (ϵ), the apparent height of the films measured by

SPFM could be very different from the real value [70, 73]. As a general rule, the apparent thickness will be smaller (larger) than the real one if $\epsilon_{film} < \epsilon_{substrate}$ ($\epsilon_{film} > \epsilon_{substrate}$). From SPFM images, the real height can be estimated using different models [70, 73]; however, they increase uncertainty relative to experimental results. The thickness of the water films is measured by comparing the apparent height of the dry and wet areas of the images. At low RH conditions, very few water molecules are adsorbed on the dry regions and the apparent contrast due to differences in dielectric constant is very high. As RH increases, more water molecules adsorb on the dry regions. These water molecules are not observed on the images until high RH is reached because they behave as a two-dimensional gas, not forming structured films. However, they increase the polarizability response of the dry regions and thus reduce the contrast in the measured apparent height. This suggests that SPFM is not the best method to measure water films thickness accurately.

Dynamic AFM (dAFM) modes are based on the mechanical excitation of the AFM probe cantilever, usually at its resonant frequency, making it oscillate. Different parameters of the oscillation, such as amplitude, frequency and phase lag, are then monitored as the tip interacts with the surface. These parameters give information about topography and energy dissipation between the tip and the sample. Amplitude modulation (AM) AFM is one of the most broadly used dAFM modes and exploits the oscillation amplitude as feedback mechanism. AM-AFM has been used to study water layers on surfaces for several years [74]. This mode provides better resolution than electrostatic methods partly due to the fact that it oscillates in close proximity to the surface, where forces are more localized. Nevertheless, this proximity also implies that it is not easy to establish if truly non-perturbative imaging can be performed. When the AFM tip is brought down to the sample, surface forces control the dynamics of the cantilever in a nonlinear regime, making it difficult to interpret and control its motion. This is particularly so when dealing with water films, and liquid films in general, which can lead to discrete steps in force, for example due to the formation of a water neck between the tip and the sample during each oscillation cycle. The implications of such effects are beyond the measurement of water films on surfaces and known to induce artifacts in general ambient AM-AFM measurements [75, 76].

As regards the analysis of water adsorbed on gold, in [74] the [111] surface was flame-annealed and then transferred immediately into an air-tight chamber at a RH value of 35%. When imaged in non-contact dAFM, the typical triangular terraces of the Au [111] surface are seen. In addition, an inhomogeneous water layer has been observed, which grew as long irregular structures of 0.2 nm in height from the border of the terraces. The authors assume that a film of the height of one water molecule forms this layer, because 0.2 nm is a value close to the dimensions of a water molecule.

A complete different approach to visualize water films on surfaces, called graphene template, has been developed in the last decade [56]. In this approach, instead of avoiding perturbation of the water films by minimizing interactions with the AFM probe, water films are "protected" and then imaged using standard AFM operational modes. This "protection" was first achieved by coating water films with a graphene sheet. In this way, water films get trapped between the graphene sheet and the surface under study. Graphene is so flexible that, when an AFM image is taken on top of it, the water film below can be recognized and its thickness measured.
Graphene sheets are transferred mechanically to a surface in a controlled environment or under ambient conditions. During the transference, water layers present on the surface become enclosed by the thin graphene sheets. If the sheets are thin enough, by performing standard contact AFM imaging, the structure of the water layers adsorbed on the surface can be imaged. The technique was first used to study water films on mica in ambient conditions [56]. It was found that the first 1-2 water adlayers on mica showed a typical thickness of $\sim$3.7 Å, the same distance between two consecutive puckered bilayers in the basal plane of hexagonal ice, and they have been interpreted as ice-like structures (see Figure B.2).
The measurements performed using a graphene template correspond actually to water confined between a surface and a graphene sheet. Water, of course, also interacts with the graphene sheets, and this fact implies that the observations of how exactly water adsorbs on the surface under study must be interpreted very carefully. Interaction with the hydrophobic graphene is known to induce the formation of ice-like flat hexagonal sheets in order to maximize hydrogen bonds with other water molecules and to avoid exposing dangling bonds to the graphene [77].

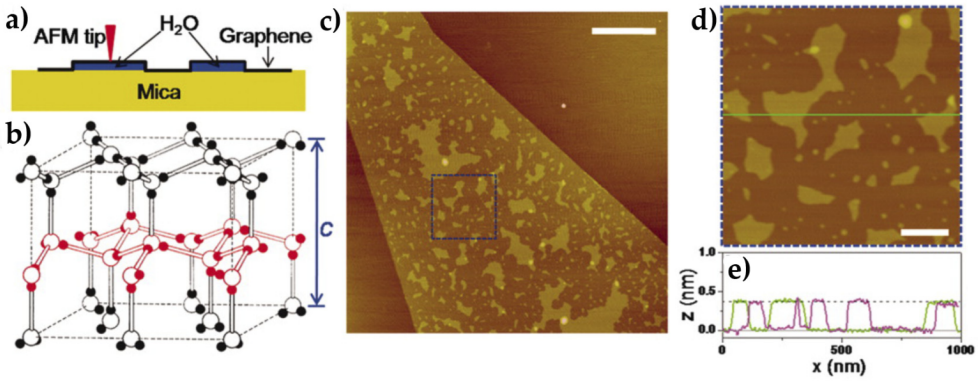

Figura B.2: (a) A schematic of how graphene locks the first water adlayer on mica into fixed patterns and serves as an ultrathin coating for AFM; (b) the structure of ordinary ice (ice I_h). Open balls represent O atoms, and smaller, solid balls represent H atoms. A single puckered bilayer is highlighted with red. Interlayer distance is c/2 = 0.369 nm when close to 0°C; (c) AFM image of a monolayer graphene sheet deposited on mica at ambient conditions; (d) A close-up of the blue square in (c); (e) Height profiles along the green line in (d) and from a different sample. The dashed line indicates z = 0.37 nm. Images adapted from Ref. [56].

Thus, is not obvious to determine to what extent the structure of the observed water films are also influenced by the presence of graphene.

In the light of these results, the STM images relating to M3-samples have been analysed. An hexagonal lattice has been superimposed on a STM image showing the dendritic structure, as shown in Fig. B.3. It is clear that the boundaries tend to have polygonal shapes, with angles of 120°. On the basis of this observation, we can suppose that this peculiar structure is in epitaxial relationship with the substrate.

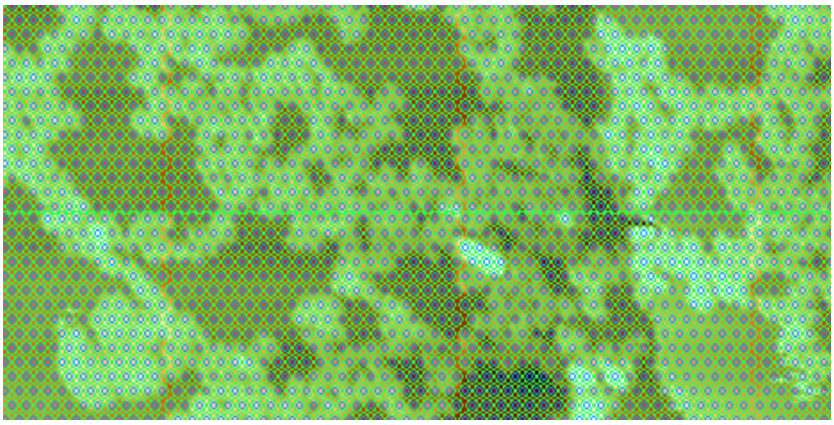

Figura B.3: STM image of sample M3-9 after the annealing up to 200°C. The hexagonal lattice has been superimposed to highlight the polygonal shapes of the dendrites' boundaries.

The dendritic structure height has been measured, as in Fig. B.4, taking into account that the relative humidity in cleanroom, where the mica was cleaved, was 31%. The dendrites' average height turned out to be 0.24±0.5 nm, in agreement with [74,78–80], but not with [56], for example. The recorded data were also tabulated into a histogram, with bins of 0.1 angstroms (Fig. B.4(c)). We can see that the highest occurrence lies in the range between 2.1 and 2.2 Å, and a Poissonian fit of the data gives an average value of 2.38 Å. Anyway, the reliability of thickness measurements, as explained above, is not so high. Moreover no evidence of water

adlayers between mica and the gold film deposited on it has been reported so far, because the physisorbed and chemisorbed water which quickly covers the mica surface after its cleavage is generally removed by heating in vacuum. And those (rare) authors who use titanium as adhesion promoter deposited much thicker metal films. After the fabrication of the M4-series, for which the mica substrate has been annealed before the Au deposition, we can say that the "water issue" has been solved. Indeed dendritic structures were no longer observed.

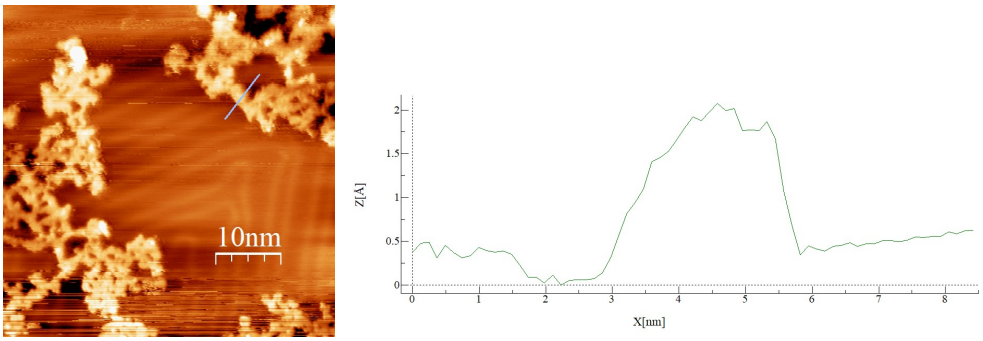

(a) (b)

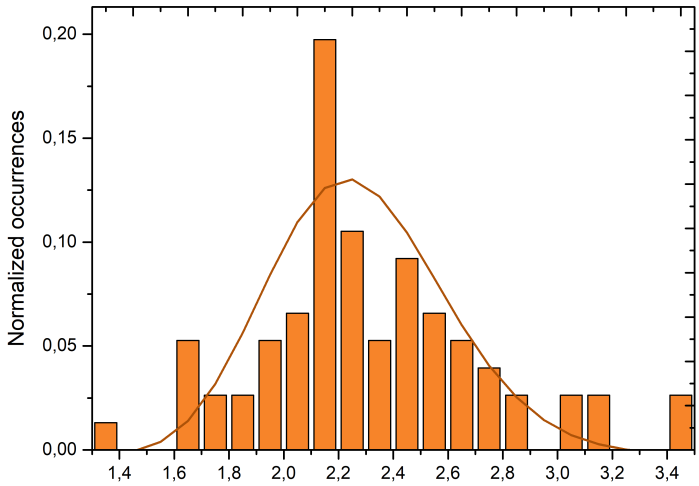

(c)

Figura B.4: (a) STM image of 400×40 nm^2 of sample M3-9 after the annealing ramp up to 350 °C. (b) Section view taken along the blue line. (c) Histogram of the dendrites' height counts. A bin width of 0.1 angstroms (approximately equal to the STM resolution) has been chosen.

Bibliografia

[1] Luca Basta, Stefano Veronesi, Yuya Murata, Zoe Dubois, Neeraj Prakash Mishra, Filippo Fabbri, Camilla Coletti, and Stefan Heun. A sensitive calorimetric technique to study energy (heat) exchange at the nano-scale. *Nanoscale*, 10:10079–10086, 2018.

[2] S. Horikoshi, R. F. Schiffmann, J. Fukushima, and N. Serpone. *Microwave Chemical and Materials Processing - A Tutorial*. Springer Singapore, 2018.

[3] Micheal E. Brown. *Handbook of Thermal Analysis and Calorimetry (volume 1)*. Elsevier, 2003.

[4] A. Mavalankar, S. J. Chorley, J. Griffiths, G. A. C. Jones, I. Farrer, D. A. Ritchie, and C. G. Smith. A non-invasive electron thermometer based on charge sensing of a quantum dot. *Applied Physics Letters*, 103(13):133116, 2013.

[5] Christoph Schick. Calorimetry. *Reference Module in Materials Science and Materials Engineering*, 2002.

[6] A. Barbini, D. Bertolini, M. Cassettari, F. Papucci, A. Salvetti, G. Salvetti, and S. Veronesi. Differential microcalorimeter for liquid samples. *Review of Scientific Instruments*, 60(7):1308–1311, 1989.

[7] D. Bertolini, M. Cassettari, G. Salvetti, E. Tombari, and S. Veronesi. A differential calorimetric technique for heat capacity and thermal conductivity measurements of liquids. *Review of Scientific Instruments*, 61(9):2416–2419, 1990.

[8] M. Cassettari, F. Papucci, G. Salvetti, E. Tombari, S. Veronesi, and G. P. Johari. Simultaneous measurements of enthalpy and heat capacity of a thermosetting polymer during the curing process. *Review of Scientific Instruments*, 64(4):1076–1080, 1993.

[9] Raymond Serway and John Jewett. *Principles of physics: a calculus-based text*. Nelson Education, 2012.

[10] P. Hidnert and G. Dickson. Some physical properties of mica. *Journal of Research of the National Bureau of Standards*, 35(4):309, 1945.

[11] Andres Castellanos-Gomez, Menno Poot, Albert Amor-Amorós, Gary A. Steele, Herre S. J. van der Zant, Nicolás Agraït, and Gabino Rubio Bollinger. Mechanical properties of freely suspended atomically thin dielectric layers of mica. *Nano Research*, 5(8):550–557, 2012.

[12] McCoul David, Hu Weili, Gao Mengmeng, Mehta Vishrut, and Pei Qibing. Recent Advances in Stretchable and Transparent Electronic Materials. *Advanced Electronic Materials*, 2(5):1500407, 2016.

[13] W.S. Wong and A. Sallelo. *Flexible Electronics: Materials and Applications*. Springer, New York, 2009.

[14] Yugandhar Bitla and Ying-Hao Chu. MICAtronics: A new platform for flexible X-tronics. *FlatChem*, 3:26–42, 2017.

[15] C.B. Carter and M.G. Norton. *Ceramic Materials: Science and Engineering*. Springer ebook collection / Chemistry and Materials Science 2005-2008. Springer New York, 2007.

[16] A. S. Gray and C. Uher. Thermal Conductivity of Mica at Low Temperatures. *Journal of Materials Science*, 12:959–965, 05 1977.

[17] C. J. Glassbrenner and Glen A. Slack. Thermal conductivity of silicon and germanium from 3 K to the melting point. *Phys. Rev.*, 134:A1058–A1069, 1964.

[18] Noboru Takeuchi, C. T. Chan, and K. M. Ho. Au(111): A theoretical study of the surface reconstruction and the surface electronic structure. *Phys. Rev. B*, 43:13899–13906, 1991.

[19] El-Batanouny, M. and Burdick, S. and Martini, K. M. and Stancioff, P. Double-sine-Gordon solitons: A model for misfit dislocations on the Au(111) reconstructed surface. *Physical Review Letter*, 58:2762–2765, 1987.

[20] J. V. Barth, H. Brune, G. Ertl, and R. J. Behm. Scanning tunneling microscopy observations on the reconstructed Au(111) surface: Atomic structure, long-range superstructure, rotational domains, and surface defects. *Phys. Rev. B*, 42:9307–9318, 1990.

[21] Ch. Wöll, S. Chiang, R. J. Wilson, and P. H. Lippel. Determination of atom positions at stacking-fault dislocations on Au(111) by scanning tunneling microscopy. *Phys. Rev. B*, 39:7988–7991, 1989.

[22] V. M. Hallmark, S. Chiang, J. F. Rabolt, J. D. Swalen, and R. J. Wilson. Observation of Atomic Corrugation on Au(111) by Scanning Tunneling Microscopy. *Physical Review Letter*, 59:2879–2882, 1987.

[23] Harten, U. and Lahee, A. M. and Toennies, J. Peter and Wöll, Ch. Observation of a Soliton Reconstruction of Au(111) by High-Resolution Helium-Atom Diffraction. *Physical Review Letter*, 54:2619–2622, 1985.

[24] S. Buchholz, H. Fuchs, and J. P. Rabe. Surface structure of thin metallic films on mica as seen by scanning tunneling microscopy, scanning electron microscopy, and low-energy electron diffraction. *Journal of Vacuum Science & Technology B: Microelectronics and Nanometer Structures Processing, Measurement, and Phenomena*, 9(2):857–861, 1991.

[25] Yuval Golan, Lev Margulis, and Israel Rubinstein. Vacuum-deposited gold films: Factors affecting the film morphology. *Surface Science*, 264(3):312–326, 1992.

[26] D. Porath, Y. Goldstein, A. Grayevsky, and O. Millo. Scanning tunneling microscopy studies of annealing of gold films. *Surface Science*, 321(1):81–88, 1994.

[27] Mark H. Dishner, Michelle M. Ivey, Sasha Gorer, John C. Hemminger, and Frank J. Feher. Preparation of gold thin films by epitaxial growth on mica and the effect of flame annealing. *Journal of Vacuum Science & Technology A*, 16(6):3295–3300, 1998.

[28] L. J. Kepley, R. M. Crooks, and A. J. Ricco. A selective SAW-based organophosphonate chemical sensor employing a self-assembled, composite monolayer: a new paradigm for sensor design. *Analytical Chemistry*, 64(24):3191–3193, 1992.

[29] A. C. Mirkin, R. L. Letsinger, R. C. Mucic, and J. J. Storhoff. A DNA-based method for rationally assembling nanoparticles into macroscopic materials. *Nature*, 382:607–9, 09 1996.

[30] J. Huang, D. A. Dahlgren, and J. C. Hemminger. Photopatterning of Self-Assembled Alkanethiolate Monolayers on Gold: A Simple Monolayer Photoresist Utilizing Aqueous Chemistry. *Langmuir*, 10(3):626–628, 1994.

[31] J. Vancea, G. Reiss, F. Schneider, K. Bauer, and H. Hoffmann. Substrate effects on the surface topography of evaporated gold films: a scanning tunnelling microscopy investigation. *Surface science*, 218(1):108–126, 1989.

[32] Guo, L.- H. and Facci, J. S. and McLendon, G. and Mosher, R. Effect of Gold Topography and Surface Pretreatment on the Self-Assembly of Alkanethiol Monolayers. *Langmuir*, 10(12):4588–4593, 1994.

[33] M. Ohring. *The materials science of thin films*. Boston: Academic Press, 1992.

[34] Li Nan, D. Allan, and Liu Gang-yu. In situ STM study of thermal annealing of Au thin films: An investigation on decay of nanometer Au clusters and 2D islands. *Acta Physica Sinica (Overseas Edition)*, 6(7):531, 1997.

[35] R.J. Colton. *Procedures in Scanning Probe Microscopies*. Wiley, 1998.

[36] I. Oštádal and P. Sobotík. STM study of Au(111) growth on mica. *Czechoslovak Journal of Physics*, 47(4):445–449, 1997.

[37] H. Klein, W. Blanc, R. Pierrisnard, C. Fauquet, and P. Dumas. Self-assembled monolayers of decanethiol on Au(111)/mica. *The European Physical Journal B - Condensed Matter and Complex Systems*, 14(2):371–376, 2000.

[38] W. Umrath. *Fundamentals of Vacuum Technology*. Oerlikon Leybold Vacuum, 2007.

[39] Kenjiro Oura, V.G. Lifshits, Alexander Saranin, A.V. Zotov, and M. Katayama. *Surface science: an introduction*. Springer Science & Business Media, 2013.

[40] *Instruction Manual of Granville-Phillips Series 350 Ultra High Vacuum Gauge Controllers*, 2008.

[41] P.A. Redhead. Thermal desorption of gases. *Vacuum*, 12(4):203–211, 1962.

[42] Ming Pan, Adrian J. Brush, Zachary D. Pozun, Hyung Chul Ham, Wen-Yueh Yu, Graeme Henkelman, Gyeong S. Hwang, and C. Buddie Mullins. Model studies of heterogeneous catalytic hydrogenation reactions with gold. *Chem. Soc. Rev.*, 42:5002–5013, 2013.

[43] *H-flux Atomic Hydrogen Source Operating Manual*, 2010.

[44] Giuseppe Grosso and Giuseppe Pastori Parravicini. X-Scattering of particles by crystals. In *Solid State Physics*, pages 349–388. Academic Press, London, 2000.

[45] Karlsruhe Institute of Technology. Research methods: LEED - Low Energy Electron Diffraction. https://www.ips.kit.edu/5881.php. 2017.

[46] Nobelprize.org. Press Release: The 1986 Nobel Prize in Physics. http://www.nobelprize.org/nobel_prizes/physics/laureates/1986/press.html. 2014.

[47] C. Julian Chen. *Introduction to Scanning Tunneling Microscopy*. Oxford University Press, 1993.

[48] J. Hudson. *Surface Science: An introduction*. Elsevier Science, 2013.

[49] D. Bonnell. *Scanning Probe Microscopy and Spectroscopy: Theory, Techniques, and Applications*. Wiley, 2000.

[50] B. Voigtländer. *Scanning Probe Microscopy: Atomic Force Microscopy and Scanning Tunneling Microscopy*. NanoScience and Technology. Springer Berlin Heidelberg, 2015.

[51] William E. Martinez, Giuliano Gregori, and Thomas Mates. Titanium diffusion in gold thin films. *Thin Solid Films*, 518(10):2585–2591, 2010.

[52] F. Pesty and P. Garoche. Low-energy electron beam on an insulator surface: Impact of the charging process on the diffraction by mica muscovite. *Surface Science*, 580(1):153–162, 2005.

[53] Walter M. Kane, James P. Spratt, and Lincoln W. Hershinger. Effects of Annealing on Thin Gold Films. *Journal of Applied Physics*, 37(5):2085–2089, 1966.

[54] Jhen-Jia Hu, Xudong Xiao, D Ogletree, and Miquel Salmeron. Imaging the Condensation and Evaporation of Molecularly Thin Films of Water with Nanometer Resolution. *Science*, 268:267–9, 05 1995.

[55] Miquel Salmeron, Lei Xu, Jun Hu, and Qing Dai. High-Resolution Imaging of Liquid Structures: Wetting and Capillary Phenomena at the Nanometer Scale. *MRS Bulletin*, 22(8):36–41, 1997.

[56] Ke Xu, Peigen Cao, and James R. Heath. Graphene Visualizes the First Water Adlayers on Mica at Ambient Conditions. *Science (New York, N.Y.)*, 329:1188–91, 09 2010.

[57] L. E. McNeil and M. Grimsditch. Elastic moduli of muscovite mica. *Journal of Physics: Condensed Matter*, 5(11):1681, 1993.

[58] A. I. Oliva, J. M. Lugo, R. A. Gurubel-Gonzalez, R. J. Centeno, J. E. Corona, and F. Avilés. Temperature coefficient of resistance and thermal expansion coefficient of 10-nm thick gold films. *Thin Solid Films*, 623:84–89, 2017.

[59] Shobhana Narasimhan and David Vanderbilt. Elastic stress domains and the herringbone reconstruction on Au(111). *Phys. Rev. Lett.*, 69:1564–1567, 1992.

[60] Oliver Schaff, Andreas K. Schmid, Norm C. Bartelt, Juan de la Figuera, and Robert Q. Hwang. In-situ STM studies of strain-stabilized thin-film dislocation networks under applied stress. *Materials Science and Engineering: A*, 319-321:914 – 918, 2001.

[61] L. Stobiński and R. Duś. Atomic hydrogen adsorption on thin gold films. *Surface Science*, 269-270:383–388, 1992.

[62] L. Stobiński and R. Duś. Model of atomic hydrogen adsorption on thin gold film surface. *Vacuum*, 45(2):299–301, 1994.

[63] Ming Pan, D. W. Flaherty, and C. B. Mullins. Low-Temperature Hydrogenation of Acetaldehyde to Ethanol on H-Precovered Au(111). *The Journal of Physical Chemistry Letters*, 2(12):1363–1367, 2011.

[64] David R. Lide. *CRC Handbook of Chemistry and Physics (84th Edition)*. CRC Press, 2007.

[65] Hairong Wu, Kai Sotthewes, Peter M. Schon, G. Julius Vancso, and Harold J. W. Zandvliet. Ordering and dynamics of oligo(phenylene ethynylene) self-assembled monolayers on Au(111). *RSC Adv.*, 5:42069–42074, 2015.

[66] G. A. Somorjai and M. A. Van Hove. Adsorbate-induced restructuring of surfaces. *Progress in Surface Science*, 30(3):201–231, 1989.

[67] Peder J. Estrup. Chemisorption and phase changes on W(100) and Mo(100). *Journal of Vacuum Science and Technology*, 16(2):635–641, 1979.

[68] Fred Lacy. Developing a theoretical relationship between electrical resistivity, temperature, and film thickness for conductors. *Nanoscale Research Letters*, 6(1):636, 2011.

[69] M. J. Madou. *Fundamentals of Microfabrication: The Science of Miniaturization*. CRC Press, 2002.

[70] Jun Hu, Xu-Dong Xiao, and Miquel Salmeron. Scanning polarization force microscopy: A technique for imaging liquids and weakly adsorbed layers. *Applied Physics Letters*, 67(4):476–478, 1995.

[71] Sergio Santos, Albert Verdaguer, Tewfic Souier, Neil H. Thomson, and Matteo Chiesa. Measuring the true height of water films on surfaces. *Nanotechnology*, 22(46):465705, 2011.

[72] E. Schmidt and W. Boas. *Plasticity of Crystals*. Chapman and Hall: London, 1968.

[73] G. M. Sacha, M. Cardellach, J. J. Segura, J. Moser, A. Bachtold, J. Fraxedas, and A. Verdaguer. Influence of the macroscopic shape of the tip on the contrast in scanning polarization force microscopy images. *Nanotechnology*, 20(28):285704, 2009.

[74] M. Luna, J. Colchero, A. Gil, J. Gómez-Herrero, and A. M. Baró. Application of non-contact scanning force microscopy to the study of water adsorption on graphite, gold and mica. *Applied Surface Science*, 157(4):393–397, 2000.

[75] Sergio Santos, Albert Verdaguer, and Matteo Chiesa. The effects of adsorbed water layers on the apparent height of nanostructures in ambient amplitude modulation atomic force microscopy. *The Journal of Chemical Physics*, 137(4):044201, 2012.

[76] A. Verdaguer, S. Santos, G. Sauthier, J. J. Segura, M. Chiesa, and J. Fraxedas. Water-mediated height artifacts in dynamic atomic force microscopy. *Phys. Chem. Chem. Phys.*, 14:16080–16087, 2012.

[77] Greg A. Kimmel, Jesper Matthiesen, Marcel Baer, Christopher J. Mundy, Nikolay G. Petrik, R. Scott Smith, Zdenek Dohnálek, and Bruce D. Kay. No Confinement Needed: Observation of a Metastable Hydrophobic Wetting Two-Layer Ice on Graphene. *Journal of the American Chemical Society*, 131(35):12838–12844, 2009.

[78] P. B. Miranda, Lei Xu, Y. R. Shen, and Miquel Salmeron. Icelike Water Monolayer Adsorbed on Mica at Room Temperature. *Phys. Rev. Lett.*, 81:5876–5879, 1998.

[79] Richard M. Pashley and Jacob N. Israelachvili. Molecular layering of water in thin films between mica surfaces and its relation to hydration forces. *Journal of Colloid and Interface Science*, 101(2):511–523, 1984.

[80] M. Antognozzi, A. D. L. Humphris, and M. J. Miles. Observation of molecular layering in a confined water film and study of the layers viscoelastic properties. *Applied Physics Letters*, 78(3):300–302, 2001.

Ringraziamenti

Vi invito a mettervi comodi, perché non saranno ringraziamenti concisi e generici, bensì mi lascerò travolgere da una vena di romanticismo che raramente mi contraddistingue (chi mi conosce bene sa che si tratta di un evento più unico che raro).

Innanzitutto vorrei ringraziare il fantastico gruppo che mi ha accolto per più di un anno presso il laboratorio Nest, integrandomi non solo in un progetto di ricerca ma soprattutto in una grande famiglia multiculturale, con cui ho condiviso tante ore di lavoro, ma anche discorsi filosofici e ricette di cucina. Un grazie particolare va al Prof. Veronesi, una delle persone più buone e pazienti che abbia mai incontrato: grazie per l'infinita disponibilità, per le piacevoli chiacchierate e per gli innumerevoli doni mangerecci.

Quindi non posso esimermi dal ringraziare i tanti amici che mi hanno accompagnato in questo lungo percorso: a partire dalla succursale pisana della bella Trinacria, il grande gruppo *Bella Pe' Tutti*, che ha iniettato qualche goccia di "siculinità" in questo povero sangue peninsulare, e più recentemente, il gruppo *GenTe Diciamo Proprio*, con cui ho condiviso tanti momenti felici, spesso orbitanti intorno all'amore per il buon cibo ("di giù").

Ora tocca alle mie donne, a partire dal *Circolo del Bridge*, con cui ho condiviso ansie e gioie: grazie a Silvia F., per le sue perle di stile e per l'infinita dolcezza, e

grazie a Kathrin, la donna cazzuta che mi ha fatto sentire meno sola (e stronza) in questo mondo.
Grazie a Silvia D., che mi ha iniziato al magico mondo dell'ecobio e che mi è stata vicina nei momenti forse più difficili degli ultimi anni, offrendomi ospitalità nelle ore più disparate e non lasciandomi mai sola.
Grazie a Suada, con cui condivido le mie grandi passioni, fitness e buon cibo (della serie "penso sempre a magnà..."), con la speranza di condividere presto anche un bel viaggio.
Grazie a Carmela, la mia Foggianazza preferita, per i pranzi a mensa centrale, i caffè con la panna e gli spetteguless.
Grazie a Erica, Bea e Irene per avermi aiutato a costruire un nucleo familiare qui a Pisa: ricordo con nostalgico affetto il nostro primo anno in casa Galante, e la gioia provata nel pulire quelle stanze luride che ci avrebbero regalato la libertà.
Grazie a Eri, per i bagordi, per le lunghe chiacchierate dopo cena, ma anche per le discussioni, che mi hanno insegnato che l'amicizia è una pietanza composta da tanti ingredienti, l'importante è saperli dosare, e penso che ce la siamo cavata bene.
Grazie alla mia pupetta Bea, che "quanto ce piace chiacchierà" a noi... Grazie perché, anche se siamo lontane da tanti anni, è come se non te ne fossi mai andata... e anche se parliamo tanto, servono poche parole per capirci. Sappi che prima o poi Oviedo ci tocca, quindi vedi di convincere Javier a venire con noi!
Grazie a Ire, per la bontà, la disponibilità e soprattutto per la straordinaria pazienza dell'ultimo periodo: non avrei potuto desiderare una coinquilina migliore.

Dulcis in fundo, un doveroso grazie va agli uomini della mia vita. Grazie a Nicola, per le lunghe chiacchierate in macchina, i confronti/scontri e le infinite domande sul senso della vita. Grazie a Domenico e Matteo, che mi hanno obbligato a tenermi informata sul calcio, in modo da non sentirmi esclusa durante le loro profonde conversazioni, e hanno ampliato gli orizzonti dei miei gusti musicali:*Le Focaccine Dell'Esselunga* sarà il tormentone della mia estate 2018.

Direi che è giunta l'ora di ringraziare i miei *Belli Snelli Fotomodelli*, ovvero la mia pazzamente fantastica famiglia, a cui devo tutto, ma tutto tutto.
Grazie a Papi, il mio Principe Azzurro. Grazie per avermi sempre incoraggiata e

supportata in ogni scelta, grazie per aver sdrammatizzato i momenti di difficoltà e per avermi fatto ridere quando più ne avevo bisogno. E grazie per aver rinunciato (spero), all'idea di Suor Thea da Mortellito, anche se a malincuore.
Grazie a Mami, per aver gioito e sofferto con me e per avermi assecondato nei momenti in cui avevo solo bisogno di lamentarmi. Grazie per avermi insegnato a pensare con la mia testa, anche se questo voleva dire percorrere un sentiero diverso da quello già battuto. Grazie per non avermi mai considerato "solo" una figlia... Lorelai e Rory ci fanno un baffo!
Grazie all'amore mio, Elves. Grazie per essermi sempre stata vicina, scatenando la grinta degna di una leonessa quando si è trattato di proteggere la sorella maggiore. Grazie per le infinite risate e per i litigi estenuanti, perché solo con te, che sei la mia migliore amica, posso essere veramente me stessa. Non so dove andremo ma ovunque saremo continueremo a condividere tutto, nel bene e nel male, te lo prometto!

Bene... penso di non aver dimenticato nessuno! Anche se... ci sarebbe un certo siciliano di mia conoscenza...
Giu, amore mio (papà non leggere che poi ti ingelosisci), grazie per aver portato egregiamente "la tua Croce" in questi 6 lunghi anni, che poi così lunghi non sembrano. Grazie per avermi sempre spinta a dare il meglio e a cercare il meglio da/per me stessa, insegnandomi che non c'è nulla che io non possa fare. Grazie per avermi consolato nei momenti di crisi e per avermi fatto ridere come solo tu sai fare. Grazie per avermi insegnato che non ho sempre ragione e che mettersi in discussione è fondamentale per vivere in armonia con gli altri. Grazie perché riesci sempre a stupirmi, come col cane di Paolo Limiti sfilato dalla tasca della giacca come in un film di James Bond, o il falso magro romanticamente servito sulla scrivania di Praticelli la sera di San Valentino. Grazie per le lettere, i "contratti" e i bigliettini... Grazie per essere un uomo che non si vergogna di dire cosa prova. Senza di te sarebbe stato tutto diverso... Spero con tutto il mio cuore che continuerai a "dare luce al salotto della mia vita" per ancora molto molto tempo... (non ti spaventare!)

Dopo ben 32 grazie potete ritenervi soddisfatti per un bel po'!